

# Current trends in strategies to improve photocatalytic performance of perovskites materials for solar to hydrogen production

Sehar Tasleem, Muhammad Tahir\*

*Chemical Reaction Engineering Group (GREG), School of Chemical and Energy Engineering, Universiti Teknologi Malaysia (UTM), 81310, Johor Bahru, Johor, Malaysia*



## ARTICLE INFO

**Keywords:**  
 Photo-catalysis  
 Hydrogen production  
 Perovskites  
 Doping  
 Band engineering  
 Z-Scheme  
 Heterojunction  
 Thermodynamics analysis

## ABSTRACT

Photocatalytic hydrogen production via water splitting is one of the favorable technologies for the solar energy conversion to renewable and sustainable energy; however, semiconductor materials under consideration have lower efficiency, selectivity and stability. Recently, perovskites are most demanding semiconductor photocatalysts belonging to very important family of materials and exhibit exceptional visible light response towards photocatalytic application. This review highlights recent developments in perovskite materials and their modification approaches for improved photocatalytic H<sub>2</sub> production. Primarily, the classification of perovskites based on structural developments; in particular, thermodynamics engineering to minimize energy barriers are discussed. Different approaches for fabrication of perovskite materials by metal and non-metal doping, while focusing on mechanism of Schottky barrier and Surface Plasmon phenomenon to improve photocatalytic efficiency are explored. This review also presents band engineering approaches in perovskites such as site substitution, solid-solution formation and nitrification of perovskites to maximize H<sub>2</sub> evolution. Elaboration of layered perovskite and improvement in their efficiency by various fabrication techniques including Z-scheme formation and composite of perovskite with TiO<sub>2</sub> and carbon-based composites including g-C<sub>3</sub>N<sub>4</sub> and rGO in terms of multi-component heterojunction based on transfer of electron-hole pairs are critically deliberated. Finally, future perspectives of perovskite materials and their efficiency enhancement approaches for sustainable solar to hydrogen production has been suggested.

## 1. Introduction

Since last few decades the aggravation of environmental and energy crisis has been rising due to the usage of fossil fuels for energy and other daily human activities [1,2]. At present, approximately, 85% of global energy consumptions are fulfilled from non-renewable resources including fossil fuels [3]. Reduction in reserves of fossil fuels and related environmental concerns has provoked substantial research efforts towards hydrogen (H<sub>2</sub>) fuel as a renewable, alternative and environmentally friendly energy carrier for the post fossil fuel regime [4–6]. For the future high energy capacity, hydrogen is recognized as the best energy carrier [7] releasing zero greenhouse gas emission, thus is considered as an alternative energy source to mitigate global warming effects [8,9]. Since 1972, the photoelectrochemical water splitting by Fujishima and Honda [10] has led to deep interest in photocatalytic hydrogen production from water and sunlight [11], as solar energy is considered Earth's most abundant source having minimal contribution towards environmental contamination [12]. Moreover, global solar energy

possess technical potential that is a number of times more than the current total energy demand [13]. Hydrogen production is the best known strategy to overcome the forthcoming consequences of environmental pollution with zero global warming [14,15]. Moreover, H<sub>2</sub> energy is considered as a sustainable, long lasting, clean, renewable source of energy [16], which can be easily stored [17,18].

A large range of semiconductor materials for photocatalytic hydrogen production have been recognized including graphene, graphitic carbon nitride (g-C<sub>3</sub>N<sub>4</sub>), conjugated polymers, metal/non-metals and carbon based photocatalysts [15,19,20]. However, most of them activate only under UV irradiation due to wide band gap [21], lack cost effectiveness and efficiency [22]. Thus, visible light photocatalysts are highly demanding as wide range of solar spectrum lies in visible light range [23,24]. Solar spectrum contains only less than 10% UV light, while more than 90% light energy lies in visible spectrum range [25]. During the past years, a number of semiconductor materials as photocatalyst with high quantum efficiencies have been reported for water splitting [26]. However, currently suitable photocatalytic materials

\* Corresponding author.

E-mail address: [m.tahir@utm.my](mailto:m.tahir@utm.my) (M. Tahir).

having suitable band gap and good stability are lacking for water splitting [27]. Moreover, in the recent years, titanium oxide ( $\text{TiO}_2$ ) [28, 29], cadmium sulfide ( $\text{CdS}$ ) [30,31] and graphitic-carbon nitride [32, 33] are mostly studied materials for water splitting, but show less efficiency towards photocatalytic process.  $\text{CdS}$  is recognized as a semiconductor with suitable band gap [34] but shows high charge recombination rate and instability for practical application [35]. Similarly,  $\text{TiO}_2$  is known as an excellent photocatalyst due to its advantages such as non-toxicity, easy availability, low cost and photostability [36, 37]. However, it shows less efficiency for photon to hydrogen conversion because of faster charge recombination in addition to its wide band gap (3.2 eV) leading to UV-light activity [37,38].

Recently, perovskite based materials are under considerations as they are multifunctional and have wide range of properties such as ferromagnetic, ferroelectric, dielectric, piezoelectric, superconducting and semiconducting [39]. Perovskites are known to be originated from calcium titanate perovskite oxide ( $\text{CaTiO}_3$ ) family with general formula  $\text{ABO}_3$  and contains several types such as titanates, tantalates, ferrites, niobates and vanadate perovskites, which are recently reported for photocatalytic applications [40]. These materials show photocatalytic activity and stability under visible light irradiation and this can be accredited due to their distinctive electronic and structural properties. Alteration in crystal structure, band gap tuning and band edge modification can be employed to enhance absorption of visible light for the photocatalytic process. Moreover, the recombination of charge carrier in perovskites can be reduced by distortion in the lattice structure and by creating oxygen vacancies [41]. Furthermore, the photocatalytic activity of perovskite materials can be further enhanced by doping with foreign elements such as metals or non-metals. Generally, the vacancy of anion and cation is indirectly influenced by doping with metals and non-metals [42]. For instance, doping of metals like Ag and Cr into titanate  $\text{SrTiO}_3$  can make it visible light active. The high visible light absorption of halide perovskites allow them to generate more  $\text{H}_2$ , however, they have lower stability in slurry systems [43]. Similarly, structure of layered perovskite allows the diffusion of dopants easily, resulting in enhanced  $\text{H}_2$  generation under solar energy.

The aim of this review is to highlight recent developments in perovskite materials, thermodynamics analysis for selective  $\text{H}_2$  evolution, band engineering evaluation and modification approaches to enhance photocatalytic activity of perovskites for sustainable and renewable energy production. Firstly, the fundamentals including mechanism for hydrogen production by perovskites and thermodynamics are briefly discussed. Secondly, an overview of perovskites with their modification approaches for enhanced photocatalytic hydrogen production by dopants is systematically discussed. The developments in perovskite composites in view of direct and indirect Z-scheme heterojunction for improved electron-hole pair's separation are discussed in detail. Finally, this review highlights recent challenges and future perspectives of perovskite material for hydrogen production.

## 2. Fundamentals of perovskite and thermodynamics analysis

### 2.1. Mechanism of photocatalysis for $\text{H}_2$ evolution

Photocatalytic water splitting for hydrogen generation can be accomplished by utilizing principles of photocatalysis from wastewater or pure water in the presence of light irradiations e.g., sunlight [44]. Light energy from the sunlight is converted into chemical energy in the presence of a suitable photocatalyst during the process of photocatalysis for  $\text{H}_2$  production [45]. Photocatalytic water splitting and photocatalytic reforming of organic substances [46] are two widely employed methods for hydrogen evolution. In the process of water splitting, electrons and holes are produced by redox reaction, while in photocatalytic organic material reforming electrons are generated by organic material and proton ions are generated after oxidation [47]. Lastly, the electrons are involved in converting protons ( $\text{H}^+$ ) into  $\text{H}_2$  over the

surface of photocatalyst [46]. In general, for the evolution of hydrogen, photocatalytic system requires reactants, photocatalyst, photo-reactor and light source. Pure water or water mixed with sacrificial reagent can be employed as a reactant and light source can either be UV light or visible light, however, visible light photocatalysts are highly demanding as they can capture substantial part of sunlight [48]. Moreover, for effective photocatalysis process for hydrogen production, an active interaction between all the components including light, catalyst and reactants is necessary [49].

Fig. 1 illustrates steps involved in perovskite photocatalysis including light harvesting (stage 1), charge excitation (stage 2), charges separation and transfer (stage 3), and surface catalytic reactions or redox reaction (stage 4). Firstly, photocatalysis starts when light energy with wavelength greater than or equal to the band gap of the photocatalyst strikes over the perovskite surface. The semiconductor perovskite consists of valence band (VB) and conduction band (CB), which are separated from each other by band gap energy ( $E_{\text{bg}}$ ). Secondly, when light strikes over the perovskite, electronic transitions are initiated, resulting in generation of electron/hole ( $e^-/\text{h}^+$ ) pairs (Eq. (1)). Thirdly, electrons and holes are separated due to the excitation of electrons from the VB to CB, leaving holes in the VB. Lastly, redox reaction takes place in which electrons are involved in the reduction of protons, while, holes are involved in the oxidation of water. During the oxidation reaction, holes decompose water into  $\text{H}^+$  as shown in (Eq. (2)), while (Eq. 3) shows formation of  $\text{H}_2$  after protons ( $\text{H}^+$ ) gain electrons. More importantly, redox reaction occurs on the surface of perovskite photocatalyst when the reduction potential of perovskite is above the CB and oxidation potential is below the VB of the photocatalyst [50]. Photoexcited holes have great oxidizing properties which are capable of oxidizing organic compounds like alcohols as illustrated in Eq. (4).



Photocatalytic water splitting is a challenging task because the entire process starting from charge carrier generation to surface catalytic reactions for producing  $\text{H}_2$  requires appropriate wavelength, intensity and energy. However, most challenging task is the fast recombination of photogenerated charge carriers due to short life time. Electrons generated in the CB can recombine with the holes inside the volume of photocatalyst or at the surface known as volume and surface recombination, respectively, to generate unproductive energy as a heat [51]. Commonly, three types of recombination are possible: First, band-band recombination is a radiative transition occurring mostly in the direct band gap semiconductors in which electrons in conductive band move to the valence band having holes; second, trap-assisted recombination in which an electron falls into an energy level within the band gap known as trap formed due to structural defect. Once trap gets filled with electrons they cannot accept more electrons. Finally, the electrons in the trap move into valence band resulting in their recombination. In auger recombination, electrons and holes have possibility to recombine in a band-to-band transition. However, in this case, the resulting energy is given off to another electron or hole. Therefore, for successful water splitting, the redox reaction and charge separation in the photocatalyst must proceed within the lifetimes of the photo-excited charge carriers [52]. For this purpose, highly efficient and selective semiconductor materials functional under solar energy are high in demand for hydrogen production application.

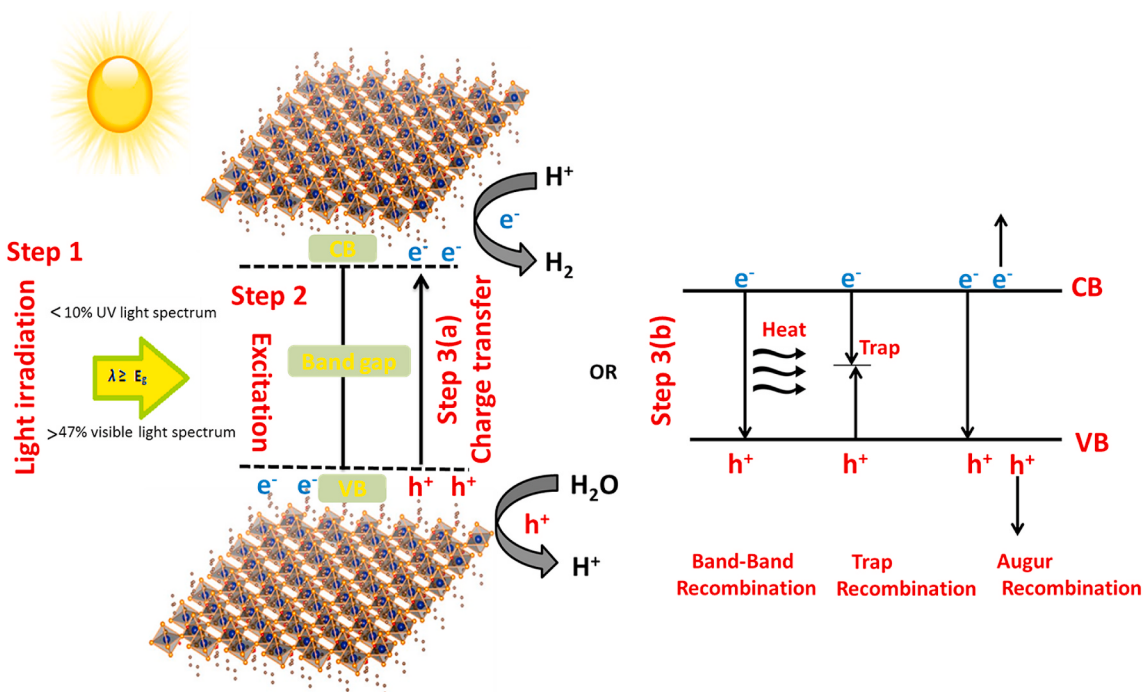


Fig. 1. Steps involved in process of photocatalysis in perovskite ranging from light harvesting to redox reaction and types of electron-hole pairs recombination.

## 2.2. Thermodynamics analysis

In photocatalytic water splitting, a photocatalyst should have band gap larger than the standard Gibbs free energy change (1.23 eV) and a smaller band gap than incident light energy for the photo-excitation to take place. Moreover, the conduction band potential should be more negative than the water reduction potential and potential of valence band should be more positive than the water oxidation potential. Secondly, it should be in a good capacity to separate and transfer photogenerated charge carriers, thus restraining their recombination. Thirdly, for accelerating redox reaction and for suppressing backward reaction, sufficient active sites should be available on the photocatalyst surface. Photocatalyst should be able to generate, excite and transfer photogenerated charge carriers and should be able to carry out redox reaction [53]. Therefore, for enhanced photocatalytic H<sub>2</sub> production process, in addition to semiconductor material absorbing solar energy, the material should have appropriate band structure to carry oxidation and reduction reactions. Moreover, understanding about this process can be obtained through the thermodynamics evaluation of the perovskite materials.

Thermodynamics in perovskite as a semiconductor photocatalyst can be discussed in terms of type and intensity of light, width of band gap, CB and VB of perovskite semiconductor. Usually, perovskite consists of a totally filled VB and partially filled or empty CB. Between VB and CB there exists a forbidden energy level having varying population of electrons and holes, termed as band gap energy ( $E_g$ ). When light energy higher than band gap energy falls on the perovskite, the population of electrons in VB and holes in CB is disturbed. Due to shorter relaxation time within the conduction band as compared to the band gap, the probability of electrons to achieve equilibrium within energy level is more than across the band gap [54]. Electrons with internal equilibrium are called quasi equilibrium and potential of electrons and holes in quasi-fermi levels is given by Eqs. (5) and (6). The maximum thermodynamic driving force for electrons and holes for inducing photocatalytic reaction can be explained by Eq. (7) [55].

$$F_n = E_c + k_B T \ln \frac{n}{N_c} \quad (5)$$

$$F_p = E_v + k_B T \ln \frac{P}{N_v} \quad (6)$$

$$\Delta G = -|Fn - Fp| = -E_g - k_B T \ln \frac{np}{N_v N_c} \quad (7)$$

where,  $E_c$  and  $E_v$  are CB minimum and VB maximum energy level positions, respectively,  $\Delta G$  denotes Gibbs free energy provided by light irradiations,  $k_B$  denotes Boltzmann constant,  $N_c$  and  $N_v$  are effective densities of states in CB and VB respectively and  $n, p$  denotes carrier concentrations.

For effective water splitting, band gap of perovskite must be 1.23 eV  $< E_g < 3.26$  eV. There are two types of light irradiations; light irradiation with wavelength 200–400 nm is UV, while, irradiation with wavelength between 400 and 800 nm is visible light. UV light can activate perovskite with band gap wider than 3.15 eV, whereas, perovskite with band gap below 3.15 eV can be activated by visible light. Secondly, for hydrogen evolution the reduction and oxidation potential must lie within the band gap of perovskite [56]. The bottom of the CB should be more negative than the redox potential of H<sup>+</sup>/H<sub>2</sub> i.e., −0.41 eV vs NHE whereas, top of the VB should be more positive than the redox potential of O<sub>2</sub>/H<sub>2</sub>O i.e., +0.82 eV vs NHE [57]. Higher number of electron-hole pairs can be generated using lamp with high power as higher light intensity cause generation of more photon flux for excitation of electrons per unit time in the semiconductor. However, poor photocatalytic efficiency even under high power lamps should possibly be due to fast recombination of photogenerated electrons and holes and inappropriate band structure of catalyst for efficient oxidation and reduction process. Photocatalytic reaction is directly proportional to light intensity but absorption of wavelength depends on the band gap and morphology of catalyst and design of photoreactor [58]. For instance, Fig. 2 (a, b) shows perovskites with narrow and wide band gaps, respectively. Narrow band gap perovskite semiconductors show absorption in the wavelength of 400–800 nm and wavelength of 200–400 nm is absorbed by a wide band gap perovskite. Therefore, before selecting type of light source, band gap and other characteristics of catalyst should be identified for getting efficient photoactivity for hydrogen generation.

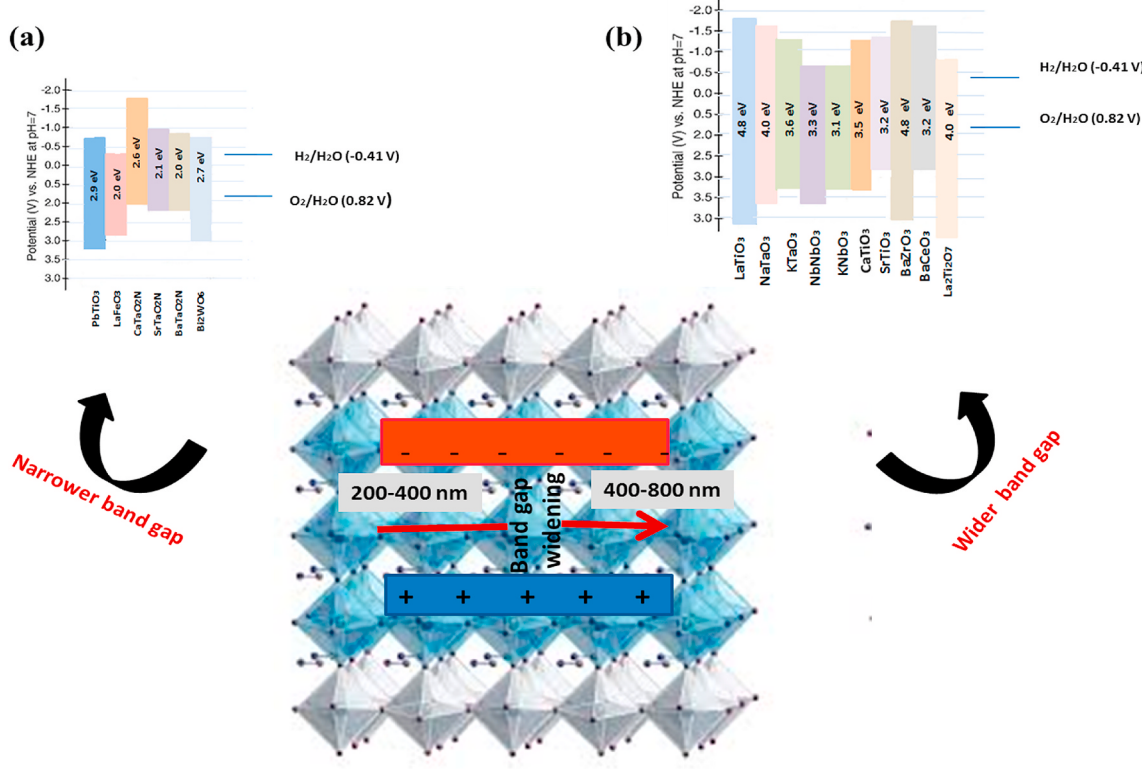


**Fig. 2.** Demonstration of relation of absorption of wavelength of light and band gap; (a) Band gap of narrow band gap perovskites; (b) Band gap of wide band gap perovskites.

### 3. Recent advancements in perovskite materials

#### 3.1. $ABO_3$ perovskite

Currently, the development of novel binary metal oxide considered as third generation photocatalysts is under consideration denoted generally by  $A_xB_yO_z$  formula. It includes perovskites and related materials, iron spinels denoted by  $AB_2O_4$ , tungstate, molybdate and vanadate containing compounds denoted by  $A^{3+}B^{5+}O_4$ . Perovskite has a general formula  $ABO_3$ , where, A denotes rare or alkaline earth metal and B denotes first row transition metals. Large ionic radius cations occupy A sites in the structure, coordinating 12 oxygen atoms, while small ionic radius cations occupy B sites in the perovskite structure, coordinating 6 oxygen atoms [41]. Perovskite constitutes advantages of excellent characterized structure as well as good surface properties with basic and alike structures, variable valences, valence metal ions and abundant O<sub>2</sub> vacancies, which makes them appropriate for photocatalytic H<sub>2</sub> generation [59]. Classification of  $ABO_3$  perovskite can be carried out as  $A^{1+}B^{5+}O_3$ ,  $A^{2+}B^{4+}O_3$  and  $A^{3+}B^{3+}O_3$  perovskites based on the valence and includes different groups of perovskites with varying rate for H<sub>2</sub> production.

Niobates ( $ANbO_3$ , A = Na, K, Ag, Cu) and Tantalates ( $ATaO_3$ , A = Na, K, Ag, Li) are included in  $A^{1+}B^{5+}O_3$  subgroup of  $ABO_3$  perovskite. Moreover, it also includes vanadium-based perovskites. Tantalates constitute an appropriate band gap based on the Ta 5 d orbitals. Also, phenomenon of efficient carrier delocalization occurs by the structure distortion of TaO<sub>6</sub> connections and is attributed to the crystalline structure, leading to enhanced photocatalytic activity [60,61]. For instance, NaTaO<sub>3</sub> and KTaO<sub>3</sub> belonging to tantalate perovskites constitute effective properties such as their availability, less toxicity and constitute CB edge that is more negative than H<sup>+</sup>/H<sub>2</sub> potential [41]. However, NaTaO<sub>3</sub> has been reported to constitute a wide band gap (4.0 eV) as the VB contains O 2p orbitals, making it active only under UV

light irradiations in addition of charge recombination. KTaO<sub>3</sub> having a band gap of (3.6 eV) is also recognized as a photocatalyst under UV irradiations, but less studies are reported for H<sub>2</sub> production. Pristine KTaO<sub>3</sub> was observed to produce 228  $\mu\text{molg}^{-1}\text{h}^{-1}$  of H<sub>2</sub> from water-methanol mixture as sacrificial agent under stimulated sunlight [62]. In another study, Xu et al. [63], reported pristine AgTaO<sub>3</sub> to produce low rate of H<sub>2</sub> i.e., 20  $\mu\text{molg}^{-1}\text{h}^{-1}$  from water-methanol mixture as sacrificial agent under UV irradiations, while, showing complete inertness under visible light. Moreover, niobates including NaNbO<sub>3</sub> (3.08 eV) and KNbO<sub>3</sub> (3.14 eV) have been reported for photocatalytic H<sub>2</sub> production under UV irradiation due to their wide band gap [64], but at the same time NaNbO<sub>3</sub> is considered for photoactivity based on its non-toxicity, stability and crystal structure which is capable of promoting charge transfer due to corner-shared octahedral [NbO<sub>6</sub>] in its structure [65,66]. Liu et al. [67], reported pristine NaNbO<sub>3</sub> nanowires to produce 32  $\mu\text{molg}^{-1}\text{h}^{-1}$  of H<sub>2</sub> under mimetic sunlight. In another study, H<sub>2</sub> rate of 350  $\mu\text{molg}^{-1}\text{h}^{-1}$  was observed for pristine NaNbO<sub>3</sub> from formic acid as sacrificial agent under UV-Visible irradiation [68]. Vanadium (B-site) based perovskites includes AgVO<sub>3</sub> which exist as crystal structure of  $\alpha$ -AgVO<sub>3</sub> with band gap of 2.5 eV and  $\beta$ -AgVO<sub>3</sub> with 2.3 eV band gap. However, AgVO<sub>3</sub> constitute a CB which is inappropriate for photocatalytic H<sub>2</sub> production and is best for O<sub>2</sub> evolution reaction and water treatment [69].

$ABO_3$  perovskite has another  $A^{2+}B^{4+}O_3$  subgroup containing titanates (ATiO<sub>3</sub> where, A = Ca, Sr, Ba, Mg, Fe etc.) as the predominant perovskites as well as B site occupied zirconium (Zn) and tin (Sn) containing perovskites. Titanates show unique electronic properties, optical properties and good stability, but wider band gap makes them active only under UV irradiations [70]. SrTiO<sub>3</sub> is the most primitive and widely studied titanate perovskite based on its suitable band levels and flat band potential, which makes it appropriate for water splitting, ability of electron transforming among Ti<sup>3+</sup> and Ti<sup>4+</sup>, availability of surface defects and high stability. However, wide band gap of 3.2 eV hinders its

visible light activity. In a study by Ikeue et al. [71], pristine photocatalytic activity of  $\text{SrTiO}_3$  revealed to be  $30 \mu\text{molg}^{-1}\text{h}^{-1}$  from 50% methanol-water mixture under UV-irradiation, while, in another study,  $8 \mu\text{molg}^{-1}\text{h}^{-1}$  rate of  $\text{H}_2$  production from 15% of methanol as sacrificial agent under UV light has been reported [72]. Furthermore, as compared to other titanates perovskites, titanates consisting of transition metals oxides having d 0 and d 10 orbitals such as  $\text{Co}^{2+}$ ,  $\text{Fe}^{2+}$ ,  $\text{Ni}^{2+}$  offers narrow band gap, leading to visible light activity. However, they have an unsuitable CB for carrying out water reduction and their photoactivity is only limited for photooxidation and water treatment reactions. Yet,  $\text{ZnTiO}_3$ ,  $\text{CdTiO}_3$  and  $\text{PbTiO}_3$  with band gap 3.68 eV, 4.0 eV and 2.72 eV, respectively are rarely studied for photocatalytic  $\text{H}_2$  production. Carrasco et al. [73], reported  $28 \mu\text{molg}^{-1}\text{h}^{-1}$ ,  $41 \mu\text{molg}^{-1}\text{h}^{-1}$  and  $46 \mu\text{molg}^{-1}\text{h}^{-1}$  of photocatalytic  $\text{H}_2$  production from pure water under UV irradiations from  $\text{ZnTiO}_3$ ,  $\text{CdTiO}_3$  and  $\text{PbTiO}_3$ , respectively [73].  $\text{CaTiO}_3$  is considered as another prominent perovskite having wide band gap (3.5eV) [74] constituting remarkable photoelectric, dielectric and catalytic photoelectric properties [75]. Moreover, studies report  $\text{CaTiO}_3$  to exhibit photocatalytic  $\text{H}_2$  production from pure water under UV irradiation. Also,  $\text{CaTiO}_3$  has an appropriate band alignment i.e., a VB lower than the water oxidation potential and a CB higher than hydrogen reduction potential. Moreover, it has a band structure comparable to  $\text{TiO}_2$  making it able to display photocatalytic activity [76]. Pristine  $\text{CaTiO}_3$  has been reported to produce insignificant  $\text{H}_2$  under visible light irradiations and  $325 \mu\text{molg}^{-1}\text{h}^{-1}$  of  $\text{H}_2$  from methanol as sacrificial agent under UV irradiation [74]. Another study reports  $\text{H}_2$  generation of  $60 \mu\text{molg}^{-1}\text{h}^{-1}$  and  $30 \mu\text{molg}^{-1}\text{h}^{-1}$  under UV irradiation and visible irradiations from 0.05 M sodium sulfite aqueous solution [77]. Other than this,  $\text{Fe}_2\text{TiO}_5$  is recognized as a pseudobrookite n-type titanate semiconductor with a narrow band gap of 2.1 eV. Based on its availability, stability, non-toxicity and charge transfer property, it has been used in dielectric anode and sensor material as well as material for electrode in photo-electrochemical process [78]. Also,  $\text{Fe}_2\text{TiO}_5$  constitute an electronic and atomic structure close to that of  $\text{TiO}_2$  [79].  $\text{Fe}_2\text{TiO}_5$  has been employed as co-catalyst in photo-electrochemical process, but, limited studies are available on its photocatalytic activity.  $157 \mu\text{molg}^{-1}\text{h}^{-1}$  of  $\text{H}_2$  from triethanolamine as the sacrificial agent under simulated sunlight was reported for pristine  $\text{Fe}_2\text{TiO}_5$  [80].  $\text{MgTiO}_3$  having a band gap of 3.5 eV is also recognized as a principle titanate photocatalyst for water splitting, but is not much explored for photocatalytic  $\text{H}_2$  production. It owns an appropriate electronic structures for water splitting with CB at  $-1.13 \text{ eV}$  and VB at  $2.37 \text{ eV}$  potential for carrying out redox reaction of water splitting into  $\text{H}_2$  and  $\text{O}_2$  [81]. Besides, bottom of CB for  $\text{MgTiO}_3$  consist of a transition-metal d orbitals ( $\text{Ti}^{4+}$ ), which is empty and is positioned at more negative potential than 0 eV. Also, a noble flat band of  $\text{MgTiO}_3$  makes it more desirable towards photoactivity [82]. Zhang et al. [83], reported  $100 \mu\text{molg}^{-1}\text{h}^{-1}$  of  $\text{H}_2$  production by using  $\text{MgTiO}_3$  as photocatalyst with methanol-water mixture under UV irradiation. Zirconium containing perovskites are not much explored for instance;  $\text{SrZrO}_3$  is considered as a photocatalyst, but lacks studies focusing on water splitting due to its wide gap of 5.6 eV. It is a potential photocatalyst as it offers an appropriate band alignment with VB and CB lower than the oxidation potential of water and higher than hydrogen reduction potential, respectively [84]. Moreover, it also shows outstanding stability and excessive active sites for photocatalytic activity [85]. Guo et al. [84], studied pristine  $\text{SrZrO}_3$  for  $\text{H}_2$  production and observed  $29 \mu\text{molg}^{-1}\text{h}^{-1}$  production of  $\text{H}_2$  from pure water under UV irradiation. Tin based perovskite such as  $\text{CaSnO}_3$ ,  $\text{BaSnO}_3$  and  $\text{SrSnO}_3$  constitute a wide band  $>4.0 \text{ eV}$ , thus their photocatalytic activity is rarely found in literature. Among Tin based perovskites,  $\text{SrSnO}_3$  is capable of showing better hydrogen production rates under UV irradiation [47,86–89].

$\text{ABO}_3$  also contains subgroup  $\text{A}^{+3}\text{B}^{+3}\text{O}_3$  constituting of ferrite perovskites having narrow band gaps with visible light photoactivity. Normally, iron oxides and hematite compounds have a low CB with other limitations including less electron conductivity and short diffusion

of exciton. Ferrite perovskites have been reported to overcome the limitations of other iron oxides by showing good photocatalytic activity [90]. For instance,  $\text{LaFeO}_3$  is known as a principle photocatalyst with a narrow band gap of 2.07 eV, making it active under visible irradiation. It offers advantages of optoelectronic properties as well as it is nontoxic and highly stable [91].  $\text{LaFeO}_3$  has been reported to depict visible light activity towards photocatalytic  $\text{H}_2$  production, but literature still lacks studies of photophysical properties of  $\text{LaFeO}_3$ .  $\text{BiFeO}_3$  with a band gap of 2.2 eV has been studied to show visible light activity towards water splitting. Moreover, it depicts multiferric properties and magneto-electric properties, which can be employed for the enhanced photoactivity by improved charge carrier separation. Though, the reduction potential of  $\text{BiFeO}_3$  is 0.3 V which is more positive as compared to the water reduction potential, but still it has issues of chemical stability in photocatalytic water splitting [92]. Iervolino et al., [93], and yang et al. [94], reported the utilization of  $\text{LaFeO}_3$  and  $\text{BiFeO}_3$  respectively, towards photocatalytic  $\text{H}_2$  production.  $\text{PrFeO}_3$  is recognized as a praseodymium ferrite and was reported for  $\text{H}_2$  production with cocatalyst from ethanol-water mixture because of its good ferromagnetic and ferroelectric properties [95]. Moreover,  $\text{GaFeO}_3$  has been observed as a ferrite perovskite for visible light water splitting activity with a yield of around  $2 \mu\text{molg}^{-1}\text{h}^{-1}$  due to its deactivation with passage of time.  $\text{YFeO}_3$  (2.43 eV) and  $\text{AlFeO}_3$  are also considered as ferrite perovskite, but are only reported for photocatalytic decomposition of organic pollutants [96].

$\text{SrTiO}_3$  is been considered as an attractive UV active photocatalyst in comparison to other titanates based on its transformation flexibility between  $\text{Ti}^{3+}$  and  $\text{Ti}^{4+}$  and surface defects. However, pristine  $\text{CaTiO}_3$  has been investigated for highest photocatalytic  $\text{H}_2$  production titanate under UV irradiation. Furthermore, it has also been identified for photoactivity from pure water under UV irradiations. Niobates including  $\text{NaNbO}_3$  is been observed for more improved  $\text{H}_2$  production rate based on its efficient charge separation ability as compared to tantalates. Ferrite perovskite including  $\text{LaFeO}_3$ ,  $\text{BiFeO}_3$  and  $\text{GaFeO}_3$  are not considered as ideal photocatalyst for photocatalytic  $\text{H}_2$  production as compared to titanates and tantalates however, the photoactivity of  $\text{LaFeO}_3$  is studied to be a good photocatalyst in ferrite perovskites.

### 3.2. Modification approaches for $\text{ABO}_3$ perovskite

Structure of perovskite is a cubic crystal lattice comprising of  $\text{ABO}_3$  stoichiometry which is capable of accommodating most of the metallic ions in the periodic table together with a significant number of other anions. This is due to various degree of lattice distortion in the real perovskite structure [97]. The distortion in the crystal lattice of the perovskite affects the whole photocatalytic activity as it changes the electronic band structure and dipole of perovskite. These changes in electronic band structure influence the excitation, transfer, and redox reactions of photogenerated charges [98]. Furthermore, the choice of the perovskites for photocatalytic  $\text{H}_2$  production is linked to their semi-conductivity and chemical photostability [99]. However, photo-activity of perovskite is lower due to wide band gap and fast charge recombination. Several modification approaches have been investigated to enhance photoactivity of perovskite for enhanced hydrogen production. Incorporation of constituent elements essentially to retain the basic structure of perovskites are widely investigated to improve photoactivity and selectivity for  $\text{H}_2$  evolution. In addition, more than 90% of metals can effectively be doped into the perovskite lattice without changing the structure and morphology [100]. Similarly, other approaches for modification of perovskites include doping with non-metals, substituting A or B site of  $\text{ABO}_3$  perovskite, formation of solid solution, incorporation of nitrogen into the perovskite lattice and formation of composites.

#### 3.2.1. Metal and non-metal loading to $\text{ABO}_3$ perovskite

Modification of perovskite semiconductors with metals is attributed

to the work function value of metals ( $\phi$ ) and energy of fermi level, which should be lower than the CB of semiconductor for efficient electrons migration to metals [101,102]. The higher work function of metals can be significant for efficient separation of electron-hole pairs and improvement of metals ability to accept electrons [103]. Moreover, higher difference of metal's work function with semiconductor, leads to higher Schottky barrier, resulting in faster charge separation for increased hydrogen production.

In recent years, metals including Pd, Au, Ag, Al Cu, Fe, La, Zr, and Cr are reported to enhance efficiency of perovskites. Metal doping to perovskite is a surface modification approach to suppress electron-hole pairs recombination by acting as an electron trap. Metals have the tendency to act as a cocatalyst by providing increased active sites for H<sub>2</sub> production reactions [104]. Furthermore, metal nanoparticles loading to perovskite forms Schottky barrier as the Fermi level of metals is lower than the conduction band of perovskites. Similarly, during band alignment of semiconductor and metal, there develops an electronic potential barrier at the semiconductor-metal heterojunction (Schottky barrier), which increases the transfer of electrons to the metal and acts as an electron trap [102]. In heterojunction of semiconductor-metal, the photogenerated electrons are transferred to metal from the CB of perovskite via Schottky barrier until their Fermi levels becomes equal, while, restraining the holes in the VB of perovskite [103]. For instance, Husin et al. [105], reported reduction in charge recombination of NaTiO<sub>3</sub> by doping with La<sup>3+</sup> which acted as a donor dopant and provided extra electrons. Similarly, Yu et al. [106], studied narrowing band gap of SrTiO<sub>3</sub> with Cr<sup>3+</sup> doping which was further reduced by incorporation of N as shown in Fig. 3(a). It was observed that the amount of H<sub>2</sub> production was significantly enhanced with higher recycled stability over Cr/N co-doped SrTiO<sub>3</sub> as illustrated in Fig. 3 (b). Similarly, enhanced photocatalytic H<sub>2</sub> evolution over Cu-doped SrZrO<sub>3</sub> was obtained as illustrated in Fig. 3 (c). Improved separation of electron hole

pairs was observed at the interface of n-type SrZrO<sub>3</sub> and p-type CuO semiconductor, resulting in significantly improved H<sub>2</sub> evolution [107]. In another work, Meng et al. [108], investigated that wide band gap of BaZrO<sub>3</sub> ( $E_g = 4.96$  eV) was reduced to 2.84 eV by Fe<sup>3+</sup> doping, which increased hydrogen production under visible light as shown in Fig. 3 (d) [108].

Moreover, incorporation of noble metals induces Surface Plasmon Resonance effect (SPR) under visible light for enhanced photocatalytic activity [109]. In the case of semiconductor-metal heterojunction under visible light, the metal contains photogenerated electrons in the Localized Surface Plasmon Resonance (LSPR), which are directly transferred to the CB of perovskite and reduction reaction takes place at the surface of perovskite [48].

Several plasmonic metals such as Pt, Au and Ag can enhance photocatalytic hydrogen production through formation of Schottky junction and strong SPR effect under visible light [110,111]. For instance, Fig. 4 (a) illustrates the significance of perovskite-metal interface for photocatalytic chemical reactions including: (1) fast flowing and energetic charge carriers, (2) formation of Schottky barrier, (3) excess charge carriers or oxygen vacancies on perovskite, and (4) generation of hot electrons for efficient light trapping [112]. For example, Xu et al. [113], investigated the use of Ag nanoparticles as a dopant for enhanced hydrogen production, enabling higher light harvesting and faster charge separation through Localized Surface Plasmon effect. Fig. 4(b) shows that the contact between AgTaO<sub>3</sub> and Ag metal facilitates direct injection of electrons to CB of AgTiO<sub>3</sub>, which are further consumed for H<sub>2</sub> evolution through reduction process. Likewise, Fig. 4 (c) shows SPR effect of Au to facilitate transfer of electrons from the Au metal to CB of BaTiO<sub>3</sub>. The back flow of electrons to Au was prevented by Schottky barrier [114]. Recently, bimetallic nanoparticles containing two different metals have been found more efficient to maximize photocatalytic activity compared to monometallic particles. This is obviously

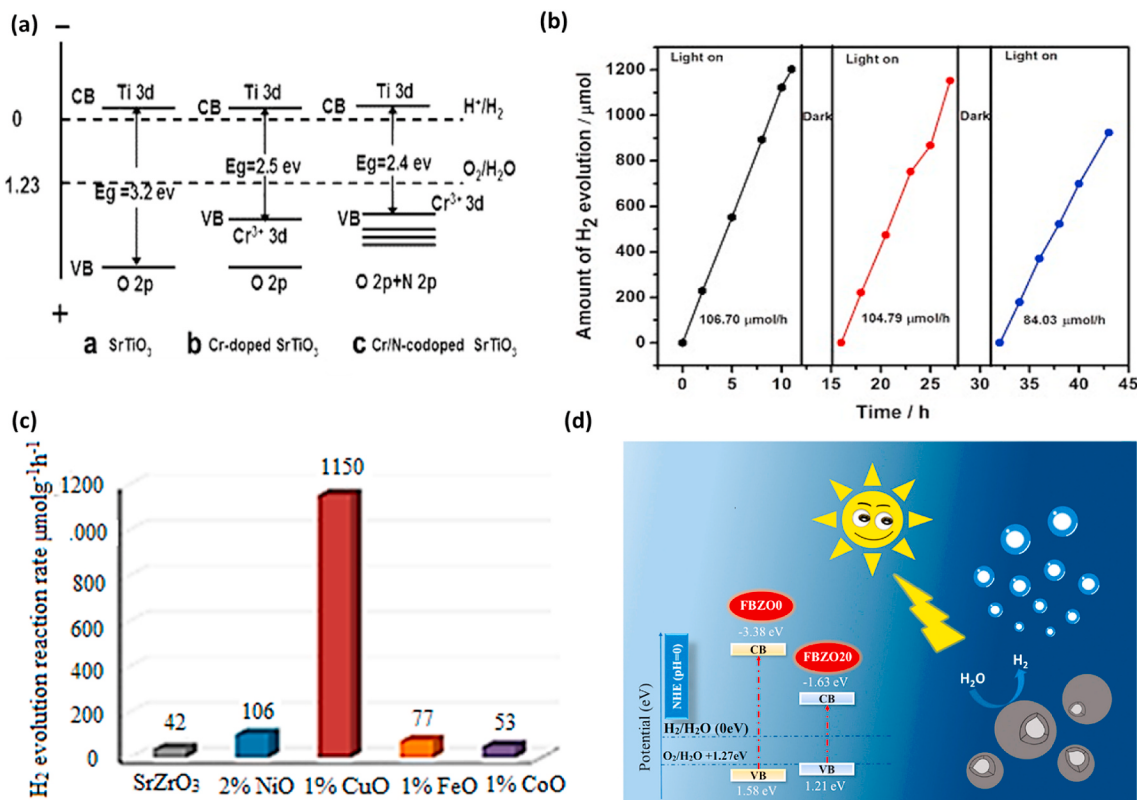


**Fig. 3.** (a) The electronic band structures for SrTiO<sub>3</sub>, Cr-doped SrTiO<sub>3</sub> and Cr/N-co-doped SrTiO<sub>3</sub> [106]; (b) Recycle course of photocatalytic H<sub>2</sub> evolution over Cr/N-co-doped SrTiO<sub>3</sub> [107]; (c) Summary of the best activities in the hydrogen evolution reaction [107]; (d) Schematic diagram for photocatalysis by Fe doped BaZrO<sub>3</sub> under visible light [108].

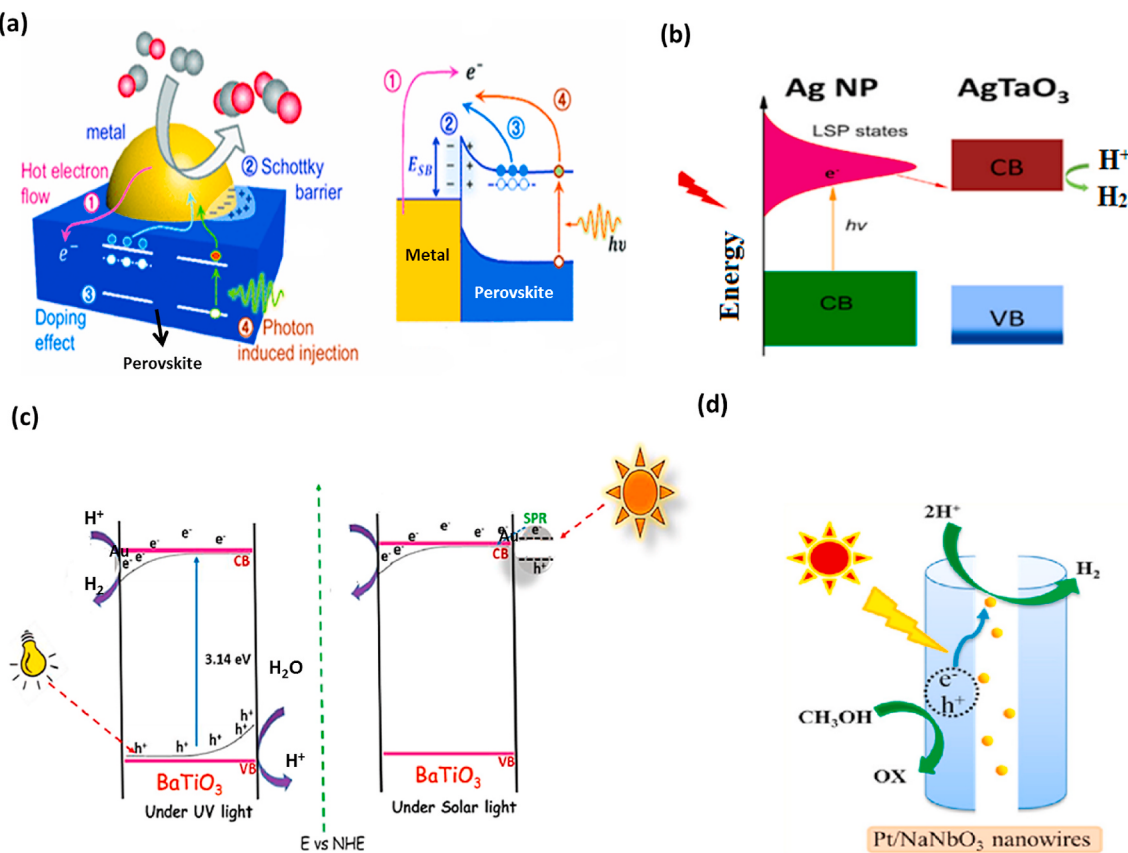


**Fig. 4.** (a) Illustration of electronic configuration and energy band diagram for perovskite-metal photocatalysts under chemical reactions [112]; (b) Representation of direct injection of excited free electrons from silver into conduction band of AgTaO<sub>3</sub> [113]; (c) Overall charge transfer mechanism by SPR effect and Schottky barrier occurring in Au doped BaTiO<sub>3</sub> [118]; (d) Schematic illustration of charge separation and transformation in the Pt/NaNbO<sub>3</sub> nanowire during photocatalytic H<sub>2</sub> production under sunlight irradiation [67].

due to their characteristics such as extraordinary optical, electronic, catalytic properties and expected synergic effect [115,116]. In this view point, Rodríguez et al. [117], reported enhanced hydrogen evolution using multilayer system of ITO/NaTaO<sub>3</sub>/Au-Pd. Addition of Au-Pd bimetallic particles increased hydrogen evolution by increasing active sites and improving absorbance of visible light. The formation of suitable Schottky barrier at the semiconductor and metal interface also contributed to increased H<sub>2</sub> production [67]. Loading Pt nanoparticles (NPs) accomplished the successful transfer process of electrons, while reducing the recombination of photogenerated electron hole pairs in NaNbO<sub>3</sub> nanowires. Fig. 4 (d) depicts the photocatalytic mechanism indicating charge separation at the surface of NaNbO<sub>3</sub> nanowire and subsequently transferring electrons to Pt nanoparticles for reduction of protons to H<sub>2</sub>. The further charge carrier recombination was prevented by reaction of holes with methanol, thus, maximizing H<sub>2</sub> evolution during photocatalytic process of water splitting and organic reforming process.

Doping of perovskite semiconductor with non-metals is relatively a new technique for improving photocatalytic hydrogen production. A variety of non-metals including C, N, and S etc. are studied to boost the photocatalytic activity. When the semiconductor perovskite is doped with non-metal, the band gap becomes narrow and causes the hybrid 2p band to be formed between CB and VB of perovskite. Under visible light irradiation, the electrons are transferred to the intermediate 2p band from VB of semiconductor and then are excited to the CB from the intermediate band to produce H<sub>2</sub>. This electron excitation process requires lower energy and also hinders charges recombination [119]. For example, Chen et al. [62], boosted photocatalytic hydrogen activity of C doped KTaO<sub>3</sub> up to 2.6 times as illustrated in Fig. 5 (a) by extending

visible light absorption and by reducing recombination of charge carriers. More importantly, this photocatalytic system maintained photoactivity even after eight cycles.

Similarly, introducing carbon can also promote more electrons to migrate at the catalyst surface, resulting in superior reduction process for hydrogen production. In another work, Wang et al. [120], investigated incorporation of N for narrowed band gap, shifted optical absorption to the visible light region and enhanced photocatalytic hydrogen production. The proposed mechanism of N incorporation into KTaO<sub>3</sub> as reported by Rao et al. [121], for hydrogen production has been presented in Fig. 5 (b). With nitrogen doping to KTaO<sub>3</sub>, the valence band formed hybrid N 2p and band gap was reduced to 2.54 eV as presented in Fig. 5 (c). Thus, band gap of KTaO<sub>3</sub> was reduced from 3.53 to 2.54 with N doping, which enabled higher visible light absorption for maximizing H<sub>2</sub> production. Likewise, Fig. 5 (d) depicts the mechanism of charge separation and transfer within N doped SrSnO<sub>3</sub>. Firstly, after excitation under UV light irradiation, charges were generated and electrons were transferred to the CB, leaving the holes behind. Subsequently, the holes were transferred to the energy level of doped N and electrons were left behind, promoting efficient charge separation.

Table 1 summarizes the literature of ABO<sub>3</sub> perovskites doped with metals and non-metals, showing H<sub>2</sub> generation activity under various reaction conditions. It can be observed that metal loading to perovskite is an effective approach to promote activity of ABO<sub>3</sub> perovskite. Appropriate Schottky barrier at metal and perovskite interface can improve charge transfer process. Furthermore, the work function of metals play significant role in reducing electron hole pairs recombination over the semiconductor surface [103]. SPR effect under visible light is the major cause for considerable attention of researchers towards

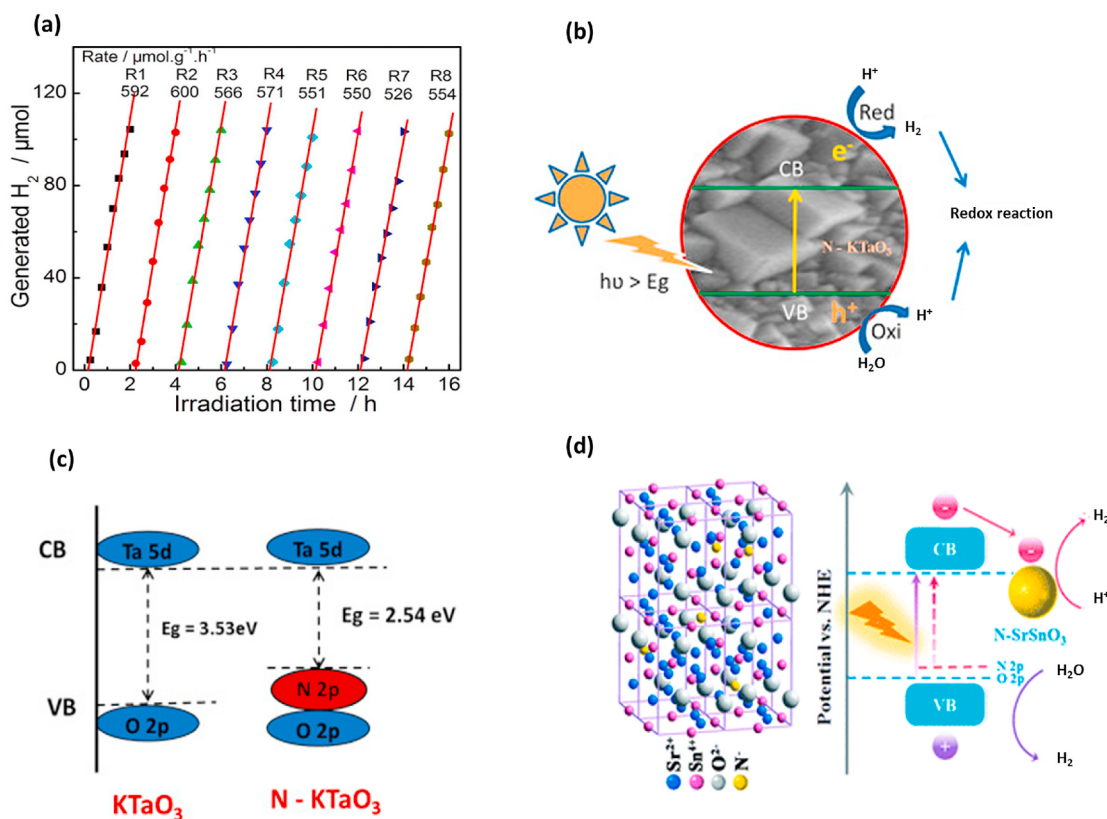


**Fig. 5.** (a) Photocatalytic H<sub>2</sub> generation of carbon-doped KTaO<sub>3</sub> under simulated sunlight and its photocatalytic stability [62]; (b) Proposed photocatalytic hydrogen evolution mechanism of N doped KTaO<sub>3</sub>; (c) Schematic representation of band gap reduction of KTaO<sub>3</sub> nanoparticles upon doping with N [121]; (d) Schematic representation of N doped SrSnO<sub>3</sub> [122].

noble metals like Ag, Au and Pt. Doping of perovskite with non-metals is considered more appropriate approach as it narrows the band gap of perovskite semiconductor and reduces centers for charge recombination, which otherwise exist in most of metal ion doping.

### 3.2.2. A site and B site substitution in ABO<sub>3</sub> perovskite

The chemical and physical properties of perovskites can be altered for enhanced photocatalytic activity by A site doping, B site doping and anion doping as depicted by Fig. 6 (a and b), illustrating the concept of A site substituted Bi<sub>0.5</sub>Na<sub>0.5</sub>TiO<sub>3</sub> and B site substituted BaFe<sub>0.95</sub>Ca<sub>0.05</sub>O<sub>3</sub> perovskite crystal structure. Variation in anionic sub lattice is linked to formation of randomly dispersed oxygen vacancies and well-ordered new structures. O<sub>2</sub> vacancies are linked to reduced surface charge recombination and enhanced charge transfer. Anionic changes are not much explored yet; they induce changes in metal-ion bond in terms of iconicity, leading to different changes in properties of perovskites [152]. However, electron-hole system is recognized to be advantageous to photocatalysis, which is entirely influenced by cation doping. Moreover, cation ion doping technique is more convenient and economical as well as advantageous for tailoring electron structure and enhancing visible light activity [53].

Generally, the size and radius of doped cations are important parameters influencing the properties of perovskite. Substitution of A ion in ABO<sub>3</sub> by different valence state A' ion also modifies the valence state of B metal ion. Moreover, this substitution induces defects and oxygen vacancies into the structure, which influence the optical and photocatalytic activity. Thus, by taking charge balance under consideration, the combination of dual metal ions rationally is an effective approach to design new photocatalyst perovskites. For interpretation, it was observed that BaTiO<sub>3</sub> has a more positive conduction band than the reduction potential of H<sup>+</sup>/H<sub>2</sub> which makes it unable to generate H<sub>2</sub>, but partially substituted Ba(II) ions by Zn(II) ions forming Ba<sub>5/6</sub>Zn<sub>1/6</sub>TiO<sub>3</sub>

constituted favorable property to be an active photocatalyst due to better charge mobility and narrowed band gap [153]. Similarly, Wang et al., [154] studied A site substituted Bi<sub>0.5</sub>Na<sub>0.5</sub>TiO<sub>3</sub> after partial substitution of Na at A site in BaTiO<sub>3</sub> forming sodium bismuth titanate. Fig. 6 (c) depicts that amount of H<sub>2</sub> produced can be controlled by adjusting alkalinity and highest H<sub>2</sub> at 9 M of NaOH was due to high conduction band edge, increased active sites and suppressed electron hole recombination. Similarly, Hu et al. [155], reported K-doped monoclinic NaTaO<sub>3</sub> showing absorption of wavelength region longer than the absorption edge. A B–O–B bond angle of 180° has been investigated for efficient electron hole pairs separation. Fig. 6 (d) indicates that pristine NaTaO<sub>3</sub> constitutes a bond angle of less than 180° as A site is occupied by smaller sized Na which hinders charge separation. Whereas, Fig. 6 (e) indicates that in K doped NaTaO<sub>3</sub>, Ta–O–Ta bond angle of 180° facilitated efficient band gap reduction and charge separation.

An overview of recent development on A site substituted perovskite photocatalysts along with their band gaps, structure, photocatalytic reaction parameters and hydrogen generation has been summarized in Table 2. Overall, La doped at A site and Pt supported La<sub>0.02</sub>Na<sub>0.98</sub>TaO<sub>3</sub> depicted highest photocatalytic H<sub>2</sub> production from glycerol-water mixture. Moreover, the structural and chemical properties of NaTaO<sub>3</sub> make it an ideal photocatalyst which was further investigated for photoactivity improvement by A site doping of La. This was mainly due to the inhibition of charge carrier recombination due to formation of ohmic junction between Pt and La<sub>0.02</sub>Na<sub>0.98</sub>TaO<sub>3</sub> as well as also due to the electron donating property of glycerol.

Other than A-site substitution, another possibility for alteration of physicochemical and photocatalytic properties of perovskites is substituting different cations at B site. Band gap of photocatalyst can be altered by combining and varying ratio of two or three metal cations rationally at B site. Usually, B site cations in ABO<sub>3</sub> perovskite control the

**Table 1**Hydrogen production and photocatalytic reaction conditions for by  $\text{ABO}_3$  perovskite.

Year	Catalyst/-structure	Band gap	Light intensity	Co-catalyst, loading of catalyst, Reactor	Reagent	$\text{H}_2$ production	Comments	Ref.
2019	$\text{ZnTiO}_3$	4.0eV	pen-ray lamp UV light 4400 $\mu\text{W}/\text{cm}^2$ (254 nm)	0.2 g, 300 mL batch reactor	200 mL of deionized water	156.6 $\mu\text{molg}^{-1}\text{h}^{-1}$	$\text{ZnTiO}_3$ synthesized by the solvo-combustion method showed the highest photocatalytic activity	[73]
2019	$\text{BaZrO}_3$	1.75eV	300 W Xe lamp ( $\lambda = 200\text{--}400$ nm)	0.1 g, airtight container connected with cooling water, vacuum system, and gas analysis device	100 mL of deionized water	67.98 $\mu\text{molg}^{-1}\text{h}^{-1}$	$\text{O}_2$ vacancies were formed in hollow $\text{BaZrO}_3$ which gave more $\text{H}_2$ than commercial catalyst	[123]
2018	Hollow - $\text{BaZrO}_3/\text{Fe}$	4.96 eV	300 W Xe lamp ( $\lambda > 420$ nm)	0.1 g, Closed circulation system	60 mL of deionized water along with 20 mL of methanol	9.45 $\mu\text{molg}^{-1}\text{h}^{-1}$	$\text{H}_2$ was Highest for 20% Fe	[108]
2018	$\text{CaTiO}_3/\text{AgCl/Ag}$	–	300 W Xe arc lamp (100 $\text{mW}/\text{cm}^{-2}$ )	0.05 wt % internal radiation reactor	90 mL water and 10 mL methanol	226.53 $\mu\text{molg}^{-1}\text{h}^{-1}$	Z-scheme heterojunction and 2D lamellar structure of the $\text{CaTiO}_3$ contributed to the activity	[124]
2018	$\text{KNbO}_3$	–	300 W Xe lamp $\lambda = 420$ nm	0.05 g, 500 mL Pyrex reactor.	crystal violet dye aqueous solution (50 mL)	245 $\mu\text{molg}^{-1}\text{h}^{-1}$	CQDs as co-catalyst formed more active sites for trapping electrons and promoted separation	[125]
2018	$\text{KNbO}_3/\text{C}$	–	300 W xenon lamp ( $\lambda = 420$ nm)	Pt 0.37 wt%, 0.1 g, Close gas circulation system	20 mL $\text{CH}_3\text{OH} + 80$ mL water	211 $\mu\text{molg}^{-1}\text{h}^{-1}$	Activity was due to enhanced separation efficiency of charge carriers due to the presence of carbon dopant in the lattice of $\text{KNbO}_3$	[126]
2018	$\text{BiFeO}_3/\text{Gd}^{3+}$	2.28eV	300 W Xe arc lamp-UV	0.1 g, batch reactor	100 mL of solution with aq. sol $\text{CH}_3\text{OH}$ volume ratio of 9:1.	67.6 $\mu\text{molg}^{-2}\text{h}^{-1}$	Magnetic properties of $\text{Gd}^{3+}$ helped its separation from solution	[94]
2018	$\text{SrTiO}_3/\text{Er}^{+3}$	3.22eV	UV-visible ( $\lambda = 405$ nm)	0.1 g, Online photo catalyst hydrogen production system	20 mL methanol + 80 mL water	333 $\mu\text{molg}^{-1}\text{h}^{-1}$	5 mol% of $\text{Er}^{+3}$ was used	[127]
2018	nanocomposite $\text{CaTiO}_3/\text{CdSe}$	3.27 eV	300 W Xe lamp ( $\lambda = 420$ )	Pt 0.6 wt%, 0.025 g, Closed quartz reactor flask.	100 mL of an aq. solution containing 0.35 M $\text{Na}_2\text{S}$ and 0.25 M $\text{Na}_2\text{SO}_3$	727.7 $\mu\text{molg}^{-1}\text{h}^{-1}$	In the composite, CdSe QDs with concentration of Cd (0.1 M) gave highest $\text{H}_2$	[128]
2018	$\text{AgTaO}_3$	–	UV pen-ray lamp of 254 nm	5 wt% $\text{CdS}$ , 0.2 g, batch-type reactor	200 mL vol of 0.5 M $\text{Na}_2\text{SO}_3$ sol.	1548 $\mu\text{mol g}^{-1}\text{h}^{-1}$	$\text{CdS}$ gave more production than NiO catalyst	[129]
2018	$\text{KNbO}_3$	–	300 W Xe-lamp- simulated sunlight	Pt 0.37 wt%, 0.1 g, closed gas circulation system	100 mL methanol aq. sol (20% $\text{CH}_3\text{OH}$ )	1300 $\mu\text{molg}^{-1}\text{h}^{-1}$	$\text{HNO}_3$ (1 M) and $\text{NH}_3$ (7 M) solution were used to adjust the pH value of the reaction solution	[130]
2018	$\text{KNbO}_3/\text{CQDs}$	–	300 W Xe lamp ( $\lambda = 420$ nm)	0.05 g, 500 mL Pyrex reactor.	crystal violet dye aqueous solution (50 mL)	468.72 $\mu\text{molg}^{-1}\text{h}^{-1}$	Mass proportion of CQDs and $\text{KNbO}_3$ was 1.5:0.5	[125]
2017	$\text{Pt/NaNbO}_3$	–	300 W Xe arc lamp- mimic sunlight irradiation.	0.1 g, top irradiation vessel	100 mL aqueous solution containing 20% $\text{CH}_3\text{OH}$	266 $\mu\text{molg}^{-1}\text{h}^{-1}$	$\text{NaNbO}_3$ gave more $\text{H}_2$ as the Pt was uniformly dispersed on $\text{NaNbO}_3$ nanowire	[67]
2017	Cubic- $\text{SrTiO}_3$	3.1eV	pen-ray lamp (254 nm)-UV	0.005 g, 250 mL Pyrex reactor	200 mL deionized water	494 $\mu\text{molg}^{-1}\text{h}^{-1}$	cubic $\text{SrTiO}_3$ exhibited the highest activity due to cauliflower-like morphology, which offered more surface area	[131]
2017	orthorhombic $\text{NaTaO}_3$	4.01eV	pen-ray lamp (UVP, 254 nm and 4400 IW/ $\text{cm}^{-2}$ )	0.005 g, 250 mL Pyrex reactor	200 mL deionized water	5672 $\mu\text{molg}^{-1}\text{h}^{-1}$	laser assisted chemical vapor deposition was used to get roof like morphology of orthorhombic $\text{NaTaO}_3$ , good for charge separation than powders	[131]
2017	Cryatalline- $\text{LaCoO}_3$	–	125 W xenon lamp UV light (cutoff filter $< 400$ nm)	0.2 g, quartz inner reaction vessel	aqueous formaldehyde solution (1.5 M) for a total solution volume of 160 mL	106 $\mu\text{molg}^{-1}\text{h}^{-1}$	Form sugarcane bagasse 1.0 g of SB gave highest results.	[132]
2016	$\text{SrZrO}_3/\text{Cu}$	4.1eV	pen-ray lamp of power UVP, and 4400 IW/ $\text{cm}^{-2}$ $\lambda = 254$ nm	0.2 g, Pyrex reactor	200 mL distilled water	1165 $\mu\text{molg}^{-1}\text{h}^{-1}$	Highest $\text{H}_2$ was for 1% Cu	[107]
2015	$\text{KNbO}_3$	–	300 W xenon lamp ( $420 < \lambda < 800$ nm)	Pt 0.5 wt%, 0.3 g, 500 mL Pyrex reactor	10% methanol as sacrificial agent	106 $\mu\text{molg}^{-1}\text{h}^{-1}$	Highest $\text{H}_2$ was at heat-treatment of 500°C for 120 min and for ratio 0.5:1.0	[133]
2014		4.07eV				26 $\mu\text{molg}^{-1}\text{h}^{-1}$		[134]

(continued on next page)

**Table 1 (continued)**

Year	Catalyst/-structure	Band gap	Light intensity	Co-catalyst, loading of catalyst, Reactor	Reagent	H <sub>2</sub> production	Comments	Ref.
	Microsphere-NaTaO <sub>3</sub>		8 W bactericidal lamp-UV(254 nm)	NiO 0.3 wt%, 0.05 g, closed gas-circulating system with a top quartz window	80 mL of deionized H <sub>2</sub> O		4 times efficiency was increased by molten salt in combination with hydrothermal processing than SSR due to rough surfaces for charge separation	
2014	SrTiO <sub>3</sub>	–	300 W Xe lamp-UV	Pt 1.0 wt%, 0.05 g	120 mL aq. sol with 25% aqueous methanol solution	2240 $\mu\text{mol g}^{-1}\text{h}^{-1}$	STO at 325°C reaction temperature for 60 min gave highest H <sub>2</sub>	[135]
2013	NaTaO <sub>3</sub>	4.14eV	500 W mercury lamp	0.10 g, closed photocatalytic system	100 mL of distilled water	3106 $\mu\text{mol g}^{-1}\text{h}^{-1}$	H <sub>2</sub> production depended on particle size. ca 70 NaTaO <sub>3</sub> nanocrystals gave more H <sub>2</sub> than ca.15	[136]
2013	KNbO <sub>3</sub> /N	3.13eV	200 W xenon arc lamp ( $\lambda > 390$ nm).	RuO <sub>2</sub> , 0.05 g, quartz tube reactor	20 vol% of methanol in 10 mL aqueous solution	6.7 $\mu\text{mol g}^{-1}\text{h}^{-1}$	N doping increased the surface area	[120]
2013	KNbO <sub>3</sub>	3.24eV	250 W xenon arc lamp ( $\lambda > 300$ nm)	Pt, 0.05 g, 100 mL Pyrex round-button flask	20 mL methanol +60 mL distilled water	1242 $\mu\text{mol g}^{-1}\text{h}^{-1}$	H <sub>2</sub> production from cubic structure was more than rods	[137]
2013	KNbO <sub>3</sub>	3.24eV	300 W Xe-lamp ( $\lambda = 250$ –380 nm).	1.5 wt % Pt, 0.1 g, 300 mL pyrex reactor	20 mL methanol +60 mL distilled water	1242 $\mu\text{mol g}^{-1}\text{h}^{-1}$	Cubic KNbO <sub>3</sub> gave more H <sub>2</sub> than orthorhombic and tetragonal	[138]
2012	Bulk SrNbO <sub>3</sub>	1.9ev	250 W iron-doped metal halide ultraviolet-visible lamp >420 nm	0.1 g, Borosilicate Coated Glass	200 mL oxalic acid aqueous solution	44.8 $\mu\text{mol g}^{-1}\text{h}^{-1}$	milling treatments of these phases without cocatalyst addition increased performance by a factor of 3, indicating improved surface	[139]
2012	Nanoparticle-GaFeO <sub>3</sub> /S	2.7eV	300 W Xenon arc lamp ( $\lambda > 395$ nm)	0.05 g, quartz photo reactor of V = 70 mL	15 mL pure water	10.8 $\mu\text{mol g}^{-1}\text{h}^{-1}$	Samples calcined at 700°C and presence of S at anionic position increased specific surface area and reduced particle size.	[140]
2012	Nanocrystalline-NaTaO <sub>3</sub>	–	450 W high-pressure mercury lamp-UV	NiO 0.4 wt%, 0.3 g, Quartz irradiation cell	500 mL water	1100 $\mu\text{mol g}^{-1}\text{h}^{-1}$	microwave-assisted hydrothermal method gave 2 times better H <sub>2</sub> than conventional hydrothermal process due to short time to produce pyrochlore Na <sub>2</sub> Ta <sub>2</sub> O <sub>6</sub> intermediate phase	[141]
2012	Bulk-BaZrO <sub>3</sub> /Ta	–	300 W Xenon arc lamp-UV	0.2 g, 100 mL double walled quartz round-bottom flask	50 mL water	900 $\mu\text{mol g}^{-1}\text{h}^{-1}$	High hydrogen production rate was attributed to reduced band gap and increased surface area.	[142]
2011	NaNbO <sub>3</sub> /Ag	–	mercury lamp of 150 W ( $\lambda = 366$ nm)	0.2 g, inner-irradiation-type reactor	0.1 mol/dm <sup>3</sup> concentration HCOOH	450 $\mu\text{mol g}^{-1}\text{h}^{-1}$	Ag species on NaNbO <sub>3</sub> works as the active site for proton reduction	[68]
2010	Bulk-AgNbO <sub>3</sub>	2.8ev	400 W Xe arc-lamp ( $\lambda > 420$ nm)	Pt 1%, 0.25 g, outer-irradiation type fused-silica volume of 90 mL	20% methanol	5.9 $\mu\text{mol g}^{-1}\text{h}^{-1}$	The higher rates were correlated with the formation of ~20–50 nm terraced surface features on the flux-synthesized particles	[143]
2010	Nanoparticle-NaTaO <sub>3</sub> /La	4.0ev	Hg lamp 400 W, ( $\lambda = 200$ –800 nm)	RuO <sub>2</sub> 1.0 wt%, 1 g, batch-type reactor	300 mL of distilled water	4108 $\mu\text{mol g}^{-1}\text{h}^{-1}$	Presence of RuO <sub>2</sub> cocatalyst gave 25 times more than La/NaTaO <sub>3</sub> without co-catalyst by acting as electron trap	[144]
2010	Nano pariculate-NaTaO <sub>3</sub> /La	4.0ev	400 W high-pressure Hg lamp ( $\lambda \geq 250$ nm)	0.5 g, inner irradiation cell	1500 mL of water with 10% methanol	2860 $\mu\text{mol g}^{-1}\text{h}^{-1}$	This H <sub>2</sub> O <sub>2</sub> -assisted sol-gel route was demonstrated to control the formation of nanosized La-doped NaTaO <sub>3</sub> as well as improved its crystallinity	[145]
2010	Bulk-NaTaO <sub>3</sub> /La	4.1eV	125 W high-pressure Hg lamp-UV	NiO 0.2 wt%, 0.05 g, inner irradiation type quartz reaction cell	170 mL glucose aqueous solution with 0.1 g glucose	14,200 $\mu\text{mol g}^{-1}\text{h}^{-1}$	NaTaO <sub>3</sub> with NiO gave more hydrogen than LiTaO <sub>3</sub> with Pt. by SSM	[146]
2010	Nanoparticles-LaNiO <sub>3</sub>	2.42eV	125 W xenon lamp ( $\lambda > 420$ nm)	0.1 g, quartz inner irradiation type	175 mL water with 25 mL HCHO	35 $\mu\text{mol g}^{-1}\text{h}^{-1}$	At 773 K mixture of LaNiO <sub>3</sub> , metallic nickel Ni formed on acted as co-catalyst	[147]
2010	LaFeO <sub>3</sub>	–	125 W medium pressure Hg visible lamp ( $\lambda > 420$ nm)	0.05 g, batch reactor	20 mL of an aq. sol with 10 vol% of CH <sub>3</sub> OH	8600 $\mu\text{mol g}^{-1}\text{h}^{-1}$	At activation temperature of 500°C, particles size was small with more surface area	[148]
2008	Cubic-KNbO <sub>3</sub>	cubic	400 W high-pressure mercury lamp UV	0.5 wt% Pt, 0.2 g, inner irradiation quartz cell	370 mL distilled water, 50 mL methanol	5500 $\mu\text{mol g}^{-1}\text{h}^{-1}$	Nanowires gave highest H <sub>2</sub> than cubes and powder	[149]

(continued on next page)

**Table 1 (continued)**

Year	Catalyst/-structure	Band gap	Light intensity	Co-catalyst, loading of catalyst, Reactor	Reagent	H <sub>2</sub> production	Comments	Ref.
2008	BaZrO <sub>3</sub>	–	400 W high-pressure Hg-lamp -UV	0.2 g, inner irradiation cell	420 mL distilled water	500 $\mu\text{mol}\text{g}^{-1}\text{h}^{-1}$	180° of Zr–O–Zr bond angle, and highly negative flat-band potential were responsible for the high photocatalytic activity	[150]
2007	Bulk-NaNbO <sub>3</sub> ,	–	350 W high-pressure mercury lamp.	0.1 g, gas-closed circulation system	aqueous methanol solution (volume ratio 1/20) (420 mL)	36.75 $\mu\text{mol}\text{g}^{-1}\text{h}^{-1}$	Max activity was on with 14 mol/L NaOH used in preparation of perovskite	[151]
2007	Nanorods-SrSnO <sub>3</sub>	4.1eV	400 W high-pressure Hg lamp-UV	Pt 0.5 wt%, 0.2 g	50 mL of CH <sub>3</sub> OH in 320 mL of H <sub>2</sub> O	8200 $\mu\text{mol}\text{g}^{-1}\text{h}^{-1}$	shape-controlled synthesis of material offered favorable photocatalytic property	[86]
2007	Bulk-CaSnO <sub>3</sub>	–	400 W high-pressure Hg lamp- UV	RuO <sub>2</sub> , 0.5 g, Inner irradiation quartz reaction cell.	50 mL CH <sub>3</sub> OH in 320 mL H <sub>2</sub> O	1630 $\mu\text{mol}\text{g}^{-1}\text{h}^{-1}$	Activity decreased for RuO <sub>2</sub> above 1.25 wt%	[89]
2006	SrSnO <sub>3</sub>	–	400 W high-pressure Hg lamp-UV	RuO <sub>2</sub> 1.25 wt %, 0.5 g, inner-irradiation type quartz reaction cell	370 mL distilled water	666.6 $\mu\text{mol}\text{g}^{-1}\text{h}^{-1}$	Activity was due to distorted SnO <sub>6</sub> octahedral connection and strong interaction in electron lattice	[88]

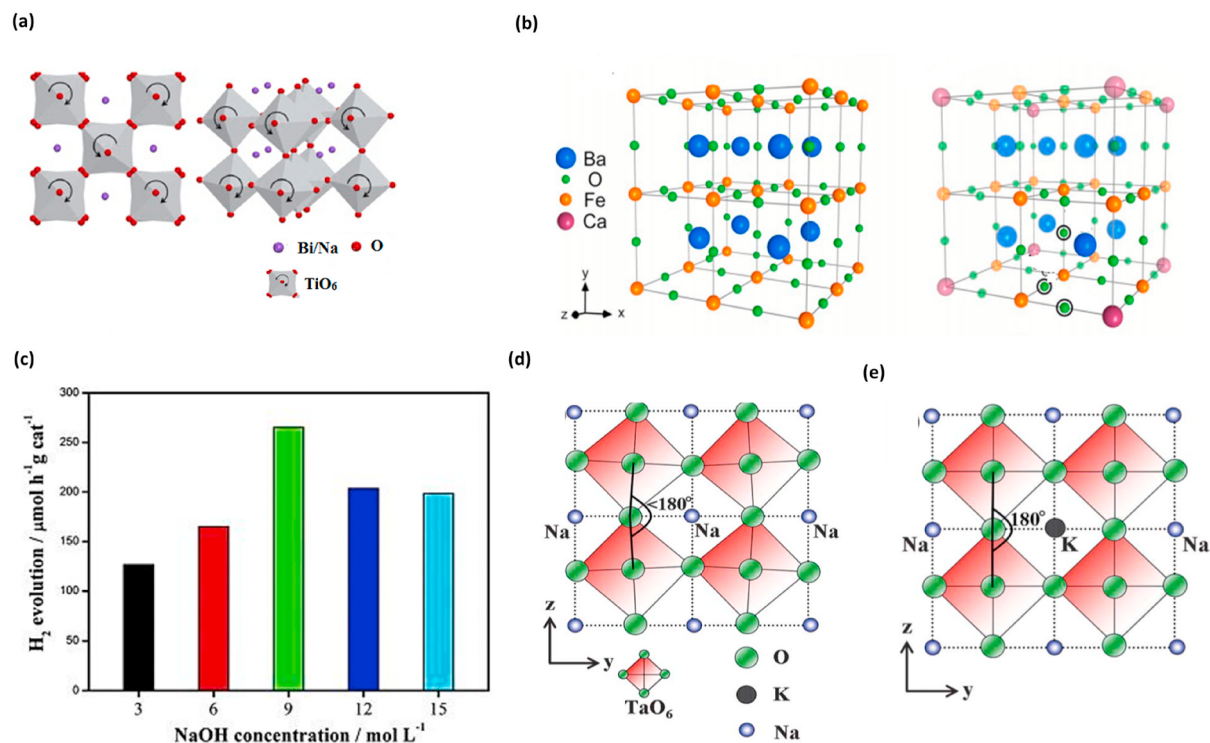


**Fig. 6.** Structural model of (a) A site substituted Bi<sub>0.5</sub>Na<sub>0.5</sub>TiO<sub>3</sub> [156]; (b) B site substituted BaFe<sub>0.95</sub>Ca<sub>0.05</sub>O<sub>3</sub> [157]; (c) Comparison of H<sub>2</sub> evolution from different NaOH concentrations [154]; (d) monoclinic NaTaO<sub>3</sub> structure with less than 180° Ta–O–Ta bond angle; (f) structure of K-doped monoclinic NaTaO<sub>3</sub> with 180° Ta–O–Ta bond angle [155].

level of conduction band. Moreover, they are involved in forming framework of perovskite structure with oxygen atoms. For example, Xu et al. [161], reported that when NaTaO<sub>3</sub> was partially substituted at B site with Cu, it temporarily trapped electrons and prolonged their lifetime, thus, limiting charge recombination and improved photocatalytic activity. In another work, Mondal et al. [162], studied doping of Zr<sup>4+</sup> into KNbO<sub>3</sub>, which was 13 times more efficient for increasing H<sub>2</sub> production and hydrogen evolution reaction (HER) activity (Fig. 7 (a)) as compared to pristine KNbO<sub>3</sub>. Fig. 7 (b, c) indicates that doping Zr (IV) led to formation of acceptor states near the valence band, which reduced the band gap from 3.29 eV in the pure system to 3.15 eV for the doped system. Wang et al. [163], reported 2333.3  $\mu\text{mol}\text{g}^{-1}\text{h}^{-1}$  H<sub>2</sub> production

by substituting Ta<sup>5+</sup> with Nb<sup>5+</sup> in NaTaO<sub>3</sub>, when some energy levels were formed under the CB which narrowed band gap of NaNb<sub>0.5</sub>Ta<sub>0.5</sub>O<sub>3</sub>. Fig. 7(d–e) shows that NaNb<sub>0.5</sub>Ta<sub>0.5</sub>O<sub>3</sub> constituted layered structure, leading to the increased reaction sites, hence, absorbing more solar energy.

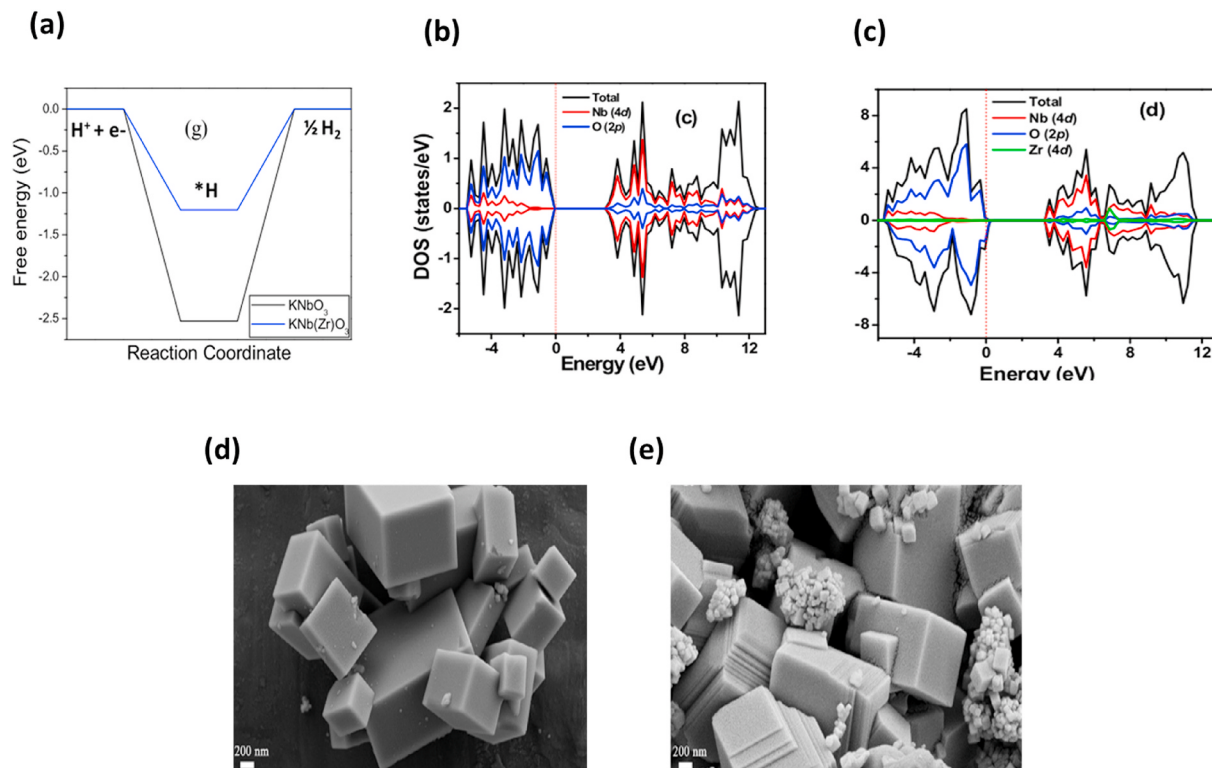
An overview of recent development on A and B site substituted perovskite photocatalysts with their band gaps, structure, photocatalytic reaction parameters and hydrogen generation has been summarized in Table 3. B site perovskite is involved in the framework of perovskite oxide structure concluding that B site substituted perovskite structure is more flexible as compared to A site substituted perovskite.

Forming solid solution is another approach to modify the band gap of

**Table 2**

Hydrogen production and photocatalytic reaction conditions for A cation substituted perovskite.

Year	Catalyst/composite	Band gap	Co-catalyst	Loading of catalyst	Light intensity	Co-catalyst, loading of catalyst, Reactor	Reagent	H <sub>2</sub> Production	Comments	Ref.
2017	La <sub>0.02</sub> Na <sub>0.98</sub> TaO <sub>3</sub>	–	Pt 0.3 wt%	0.3 g	400 W high pressure Hg lamp ( $\lambda \geq 250$ nm)	Pt 0.3 wt %, 03 g, Pyrex glass reactor	300 mL of water containing 5.0%–35% v/v of glycerol	300,000 $\mu\text{molg}^{-1}\text{h}^{-1}$	30% glycerol gave highest H <sub>2</sub>	[158]
2012	Microsphere-Bi <sub>0.5</sub> Na <sub>0.5</sub> TiO <sub>3</sub>	2.9eV	3 wt% Pt	0.15 g	500 W xenon lamp-UV	3 wt% Pt, 0.15 g, pyrex cell with a top window	200 mL aqueous solution with 40 mL methanol	325.4 $\mu\text{molg}^{-1}\text{h}^{-1}$	9 M of NaOH during preparation of catalyst gave highest H <sub>2</sub>	[154]
2012	Crystalline bulk-Sr <sub>2/3</sub> Zn <sub>1/3</sub> TiO <sub>3</sub> Crystalline sphere-Ba <sub>5/6</sub> Zn <sub>1/6</sub> TiO <sub>3</sub>	–	–	0.1 g	400 W high-pressure mercury and xenon lamp-UV	0.1 g, Pyrex reactor with a capacity of 500 mL, attached to an inner radiation type	5 mL CH <sub>3</sub> CH <sub>2</sub> OH in 155 mL H <sub>2</sub> O	73.2 $\mu\text{molg}^{-1}\text{h}^{-1}$	H <sub>2</sub> was highest from methanol without co-catalyst as compared to with pure water and without catalyst	[153]
2011	Na <sub>0.95</sub> K <sub>0.05</sub> TaO <sub>3</sub>	3.75eV	–	0.1 g	400 W high-pressure mercury lamp-UV	0.1 g, gas-closed inner irradiation system	1100 mL of pure water	11,000 $\mu\text{molg}^{-1}\text{h}^{-1}$	5% replacement of Na with K at A site gave well-dispersed K in the perovskite.	[98]
2011	(Na <sub>0.5</sub> La <sub>0.5</sub> TiO <sub>3</sub> ) <sub>1.00</sub> (LaCrO <sub>3</sub> ) <sub>0.08</sub>	2.25eV	Pt 1.0 wt %	0.30 g	300 W Xe arc lamp ( $\lambda \geq 420$ nm)	Pt 1.0 wt%, 0.30 g, Pyrex glass cell (V = 453 mL)	270 mL aq. sol with 18.5 vol %, of CH <sub>3</sub> OH	8.2 $\mu\text{mol g}^{-1}\text{h}^{-1}$	0.08 Cr was considered from LaCrO <sub>3</sub>	[159]
2009	La <sub>0.02</sub> Na <sub>0.98</sub> TaO <sub>3</sub>	4.01eV	NiO	1 g	400 W high pressure mercury lamp	NiO, 1 g, inner irradiation cell made of quartz	390 mL of reactant solution	3570 $\mu\text{molg}^{-1}\text{h}^{-1}$	Fast heating in microwave method was best as compared to furnace heating to get good crystallinity and surface area	[160]

**Fig. 7.** (a): Free energy profile of the hydrogen evolution reaction; (b) Total and Projected density states of pristine KNbO<sub>3</sub> and; (c) Zr-doped KNbO<sub>3</sub> [162]; (d) SEM images of NaNbO<sub>3</sub> and; (e) NaNb<sub>0.5</sub>Ta<sub>0.5</sub>O<sub>3</sub>.

perovskite for enhanced photocatalytic activity and hydrogen production. Solid solution formation is encouraged due to the favorable capacity of ABO<sub>3</sub> perovskite to accommodate variety of valences and cations at A site and B site having formula (ABO<sub>3</sub>)<sub>x</sub> (A'B'O<sub>3</sub>)<sub>1-x</sub>. Solid

solutions consist of lowered CB and increased VB edge as the band gap of solid solution is between the band gaps of two materials. In solid solution perovskite, both A and B sites can be occupied with variety of cations. The inappropriate band gap makes some of the perovskites

**Table 3**

Hydrogen production and photocatalytic reaction conditions for B site substituted perovskite.

Year	Catalyst/composite	Band gap	Light intensity	Co-catalyst, Loading of catalyst, Reactor	Reagent	$H_2$ production	Comments	Ref.
2018	Bulk-KTa <sub>0.75</sub> Nb <sub>0.25</sub> O <sub>3</sub> /C	3.30eV	300 W Xe-lamp-simulated sunlight	Pt 0.37 wt% 0.1 g, top-irradiation reactor	100 mL aqueous solution with 20 vol% methanol	1776 $\mu\text{molg}^{-1}\text{h}^{-1}$	2.5% C/KTN gave highest $H_2$ by acting as carbon reservoir but after this it started to decrease as excess C hindered the incident light utilization.	[164]
2017	KNb(Zr)O <sub>3</sub>	3.08eV	Newport xenon lamp 450 W	Pt 1 wt %, 0.04 g, 100 mL Pyrex glass reactor	20 mL of aq sol and 10 v/v% MeOH	886.87 $\mu\text{molg}^{-1}\text{h}^{-1}$	Highest $H_2$ was for 20 mol% of Zr as it tuned the specific surface area, crystallinity, crystal defects	[162]
2016	Monoclinic-NaNb <sub>0.5</sub> Ta <sub>0.5</sub> O <sub>3</sub>	3.53eV	150 W medium pressure Hg lamp-UV	Pt 0.125 wt%, 0.2 g, Pyrex glass reactor	1000 mL of methanol aq. sol with 10 vol % methanol	1000 $\mu\text{mol g}^{-1}\text{h}^{-1}$	Improved activity was shown by 1:1 combination of Ta and Nb. High % of Pt also showed high $H_2$ production due to well dispersion and more active sites	[165]
2012	Bulk-K <sub>0.95</sub> Ta <sub>0.92</sub> Zr <sub>0.08</sub> O <sub>3</sub>	3.5eV	500-W Xenon lamp-UV	0.2 wt% PtO <sub>x</sub> , 0.1 g, quartz reaction cell (V = 500 mL)	Distilled water (30 mL)	1912 $\mu\text{mol g}^{-1}\text{h}^{-1}$	KOH was used to adjust the pH to 11	[166]
2012	SrFe <sub>1/2</sub> Nb <sub>1/2</sub> O <sub>3</sub>	2.06eV	Hg arc lamp 500 W ( $\lambda \geq 420$ nm)	Pt 0.2 wt%, upper-irradiation type Pyrex reaction vessel	80 mL distilled water with 20 mL CH <sub>3</sub> OH	45 $\mu\text{molg}^{-1}\text{h}^{-1}$	existence of the Fe d- orbital gave high coefficient of absorption and made SFNO visible light active	[167]
2010	Nanoparticulate-LaNi <sub>0.7</sub> Cu <sub>0.3</sub> O <sub>3</sub>	2.8eV	125 W xenon lamp with UV cut-off $\lambda \leq 400$ nm)	0.1 g, quartz inner irradiation	H <sub>2</sub> O 175 mL with 25 mL HCHO	582 $\mu\text{molg}^{-1}\text{h}^{-1}$	Catalyst reduced at 250°C had a balance between Cu <sup>2+</sup> /Cu <sup>1+</sup> = 1 and oxygen vacancies = 0.25, responsible for high $H_2$	[168]
2010	Crystalline nanoparticles-LaNi <sub>0.5</sub> Cu <sub>0.5</sub> O <sub>3</sub>	2.5–2.8eV	12 W xenon lamp with UV-light cut-off filter $\lambda \leq 400$ nm	0.1 g, quartz inner irradiation	H <sub>2</sub> O 175 mL with 25 mL HCHO	575 $\mu\text{molg}^{-1}\text{h}^{-1}$	Catalyst reduced at 250 °C gave highest $H_2$	[169]
2010	BaZr <sub>0.7</sub> Sn <sub>0.3</sub> O <sub>3</sub>	–	300 W Xe lamp ( $\lambda \geq 415$ nm).	0.2 wt% NiO, 0.1 g, Pyrex closed gas circulation reactor	Aqueous methanol solution (20 vol %)	1355 $\mu\text{molg}^{-1}\text{h}^{-1}$	Sn incorporation resulted in the Sn 5s orbitals in bottom of conduction band of BaZrO <sub>3</sub> and also caused indirect to direct band gap transition	[170]
2006	SrTi <sub>0.9</sub> Cr <sub>0.1</sub> O <sub>3</sub>	–	350 W high-pressure Hg lamp-UV	0.1 g, Inner irradiation quartz reaction cell. V = 420 mL	aqueous methanol solution (volume ratio 1/20)	38.24 $\mu\text{mol g}^{-1}\text{h}^{-1}$	Surface area of SrTiO <sub>3</sub> and SrTi <sub>0.9</sub> Cr <sub>0.1</sub> O <sub>3</sub> was same, so high $H_2$ was due to Cr doping by solvothermal method at 100°C temperature causing band transition from the Cr 3d to the Cr 3d + Ti 3d hybrid orbital.	[171]
2006	CaTi <sub>0.99</sub> Rh <sub>0.01</sub> O <sub>3</sub>	–	300-W Xe lamp ( $\lambda \geq 420$ nm)	Pt 0.1 wt%, 0.3 g, Pyrex-glass cell	150 mL aq. sol with 10% methanol	16.6 $\mu\text{molh}^{-1}\text{g}^{-1}$	Doping of more than 1.0 mol % Rh favored charge recombination	[172]
2004	Bulk-BaZn <sub>1/3</sub> Nb <sub>2/3</sub> O <sub>3</sub>	3.90eV	400 W high-pressure Hg lamp-UV	NiO and RuO <sub>2</sub> , 0.5 g, inner-irradiation type quartz cell	50 mL CH <sub>3</sub> OH in 320 mL H <sub>2</sub> O	2685.7 $\mu\text{molg}^{-1}\text{h}^{-1}$	Conduction band Zn <sup>2+</sup> 4s and the valence band O 2p played important roles in the photocatalytic activity.	[173]
2003	Bulk-BaCo <sub>1/3</sub> Nb <sub>2/3</sub> O <sub>3</sub>	2.46eV	Xe arc lamp 300 W ( $\lambda \geq 420$ nm)	NiO 1.0 wt %, 0.5 g, Quartz cell reactor	270 mL distilled water	2.4 $\mu\text{molg}^{-1}\text{h}^{-1}$	Bad gap was based on the ionic radii of Ba <sup>2+</sup>	[174]
2003	Cubic-CaIn <sub>0.5</sub> Nb <sub>0.5</sub> O <sub>3</sub>	4.17eV	400 W high-pressure Hg lamp- UV	Pt 0.2 wt%, 0.5 g, inner irradiation type quartz cell	50 mL of CH <sub>3</sub> OH in 220 mL of H <sub>2</sub> O	304 $\mu\text{molg}^{-1}\text{h}^{-1}$	With decreasing ionic radius in the A site, photocatalyst showed different activities for evolving $H_2$	[175]

incapable for visible light activity towards  $H_2$  production. However, formation of solid solution perovskites is expected to improve photocatalysis under visible irradiation due to tuning of band gap positions with material having single phase [176]. Lv et al. [177], reported that Bi doping into SrTiO<sub>3</sub> introduced additional band energy in band gap of SrTiO<sub>3</sub> which increased light absorption and acted as an effective donor. Fig. 8 (a, b) shows amount of  $H_2$  production by solid state and hydrothermal methods for Bi doped SrTiO<sub>3</sub>, respectively. Lu et al. [178], indicated that solid solution Sr<sub>0.6</sub>Bi<sub>0.4</sub>Ti<sub>0.6</sub>Fe<sub>0.4</sub>O<sub>3</sub> showed high apparent quantum efficiency for hydrogen production under UV and visible irradiation. The amount of  $H_2$  evolution was two times and five times higher than pristine SrTiO<sub>3</sub> and BiFeO<sub>3</sub>, respectively. Moreover, Fe in solid solution of Sr<sub>0.6</sub>Bi<sub>0.4</sub>Ti<sub>0.6</sub>Fe<sub>0.4</sub>O<sub>3</sub> also played an important role in

band gap reduction by forming spin polarized band in intrinsic band gap, resulting in enhanced visible light activity. Pan et al. [179], investigated TiOXH/SiOXH-deposited oxynitride LaTaON<sub>2</sub> and complex oxide LaMg<sub>2/3</sub>Ta<sub>1/3</sub>O<sub>3</sub> solid solution with comparable lattice as shown in Fig. 8(c) and indicated its performance for overall water splitting up to 600 nm wavelength. Fig. 8 (d) indicates that water splitting reaction proceeding between amorphous oxyhydroxide and oxynitride or on amorphous oxyhydroxide, preventing N<sub>2</sub> evolution.

Table 4 summarizes the possible solid solution perovskites as photocatalyst for hydrogen production, taking under consideration the band gaps, structure and reaction parameters. Overall, the change of valence band and conduction band can modify the band structure which is accomplished by formation of solid solution.

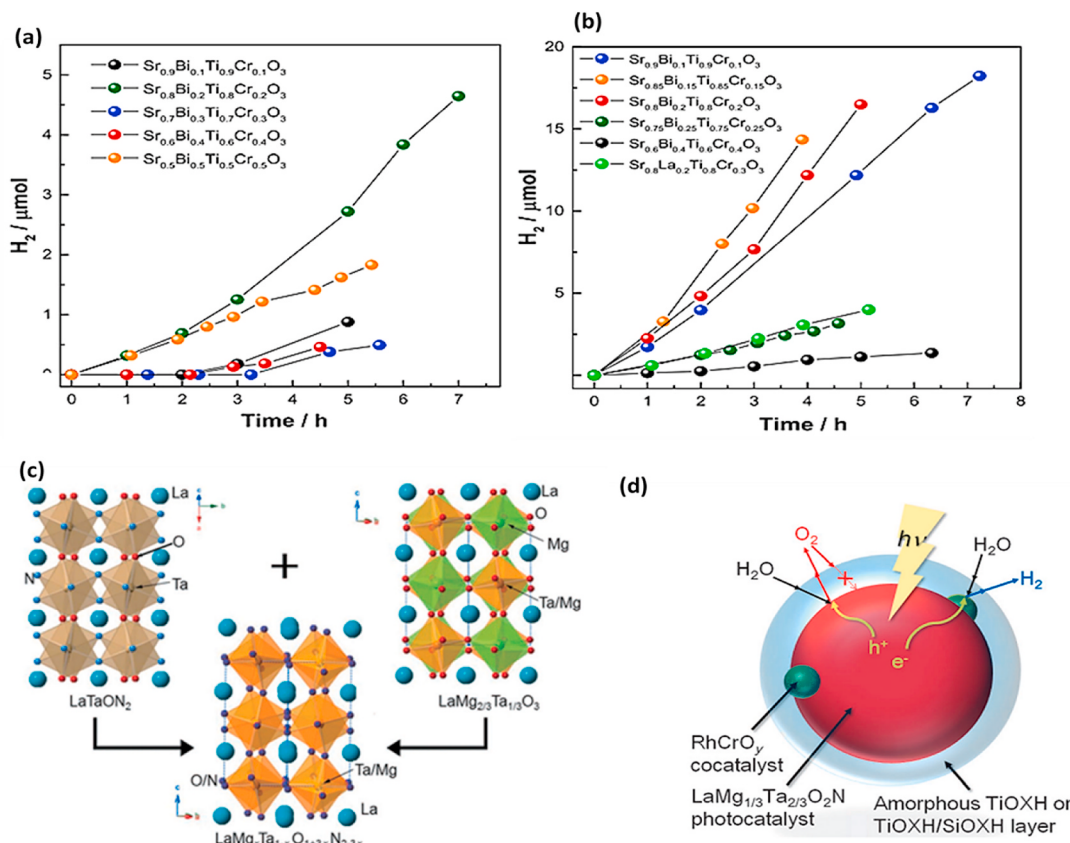


**Fig. 8.** (a) Hydrogen production of samples in prepared by SSR; (b) By HT method under visible irradiation ( $\lambda \geq 420 \text{ nm}$ ) [177]; (c)  $\text{LaMg}_x \text{Ta}_{1-x}\text{O}_{1+3x}\text{N}_{2-3x}$  ( $x = 0-2/3$ ); (d) Reaction mechanism for water splitting on a surface-coated photocatalyst [179].

### 3.2.3. Nitridation of perovskite oxide

Nitridation of perovskite oxides to form oxynitride  $\text{ABO}_{2-x}\text{N}_{1+x}$  [152] is another approach to decrease band gap of  $\text{ABO}_3$  perovskite, showing proficient photocatalytic activity under visible light. Anionic substitutions i.e., the partial replacement of oxygen ions by other anions in sub-lattice mostly refer to vacancies, which play an important role in improving photocatalytic activity [184]. Only few elements including fluorine ( $r_F = 1.3 \text{ \AA}$ ) and nitrogen ( $r_N^{3-} = 1.5 \text{ \AA}$ ) are utilized for partial substitution of oxygen due to geometrical limitations [82]. Tantalum oxynitride perovskites  $\text{ATaO}_2\text{N}$  ( $\text{A} = \text{Ca, Sr, and Ba}$ ) are capable of visible light activity. Transition metal oxynitrides having d 0 and d10 orbitals including  $\text{LaTiO}_2\text{N}$ ,  $\text{LaNbON}_2$ ,  $\text{ANbO}_2\text{N}$  ( $\text{A} = \text{Ba, Sr, Ca}$ ),  $\text{ATaO}_2\text{N}$  ( $\text{A} = \text{Ba, Sr, Ca}$ ),  $(\text{Ga}_{1-x}\text{Zn}_x)(\text{N}_{1-x}\text{O}_x)$  and  $(\text{Zn}_{1+x}\text{Ge})(\text{N}_2\text{O}_x)$  have been studied for visible light photoactivity [184]. Partially nitrated compounds offers new structural, chemical and physical properties, which induce more reactivity in oxynitrides as compared to stoichiometric compounds [185]. They have narrow band gap as compared to  $\text{TiO}_2$  and can be used under visible light, however their band alignment of CB and VB is not much appropriate to carry out redox reaction and also depict faster charge recombination, thus leading to poor efficiency [186]. Generally, oxynitrides are known to be evolved from A site transition metals including W, V, Nb, Mo, Ti, Zr, Ta and B site occupied by rare earth and alkaline earth metals [152]. Mostly, the light absorption of oxynitrides lies within 600–650 nm of visible light range which promote visible light photocatalysis. The visible light absorption of oxynitrides is due to the new energy intermittent level formed due to N 2p orbitals above the valence band edge by O 2p orbitals.

Oxynitrides possess a number of potential applications as they are thermally and chemically stable and their application in photocatalysis lies in the fact that appropriate substitutions can easily tune their band gap, thus increasing applications of perovskite-based oxynitrides [185].

The tuning of Ta–O–N system can be carried out by controlling amount of nitrogen to be doped, thus can alter their electrical properties [187]. As compared to pure oxides, the promising ordering of nitrogen and oxygen in oxynitrides offer more structural freedom [188]. For instance, Qi et al. [189], reported that loading  $\text{BaTaO}_2\text{N}$  on the surface of  $\text{Ta}_3\text{N}_5$  developed  $\text{Ta}_3\text{N}_5/\text{BaTaO}_2\text{N}$  heterostructure, which encouraged efficient charges separation to get higher efficiency for  $\text{H}_2$  evolution. Fig. 9 (a) presents the relative band positions of  $\text{BaTaO}_2\text{N}/\text{Ta}_3\text{N}_5$  and Fig. 9 (b) shows that  $\text{BaTaO}_2\text{N}/\text{Ta}_3\text{N}_5$  remains photochemically stable in cyclic runs over longer period of time. Similarly,  $\text{CaNbO}_2\text{N}$  showed increased absorbance of visible light and reduced charge recombination, thus increasing  $\text{H}_2$  evolution [190]. Oxynitride perovskite photocatalyst  $\text{LaTiO}_2\text{N}$  showed enhanced photocatalytic  $\text{H}_2$  generation under 600 nm of visible light irradiation and was reported as the first oxynitride for photocatalysis [191].

The photocatalytic hydrogen production and photocatalytic parameters of oxynitrides are elaborated in Table 5. Oxynitride perovskite photocatalysts have been developed and gained attention due to their increased quantum efficiency as the anionic substitution of N controls VB, leading to the advantage of easy tuning of band gap potentials and band gap energy. Although, oxynitrides are under consideration, more research in terms of different properties including defects, doping, and morphology related properties should be focused. Moreover, formation of composite and loading of cocatalyst should also be considered for oxynitrides.

### 3.3. Layered perovskites

Although,  $\text{ABO}_3$  perovskites constitute excellent photocatalytic properties, but layered perovskites are reported to be more novel because of flexible structure in comparison to bulk materials. Layered

**Table 4**

Hydrogen production and photocatalytic conditions for perovskite solid solutions.

Year	Catalyst/composite	Band gap	Light intensity	Co-catalyst, loading of catalyst, Reactor	Reagent	H <sub>2</sub> production	Comments	Ref.
2018	Ca <sub>0.80</sub> La <sub>0.20</sub> Ti <sub>0.8</sub> 0Cr <sub>0.20</sub> O <sub>3</sub>	3.15eV	500 W high pressure mercury lamp (cut-off filter $\lambda \geq 400$ nm and $\lambda \geq 250$ nm)	Pt 1 wt%, 0.1 g, top-irradiation-type reactor	100 mL aq. sol with Na <sub>2</sub> SO <sub>3</sub> (0.05 M)	164 $\mu\text{molg}^{-1}\text{h}^{-1}$	Hollow CaTiO <sub>3</sub> owns higher light absorption in comparison to solid one due to enhanced photon-matter interaction and further activity was improved by 5% La/Cr	[77]
2017	Cubic-Sr <sub>0.6</sub> Bi <sub>0.4</sub> Ti <sub>0.6</sub> Fe <sub>0.4</sub> O <sub>3</sub>	-	500 W high-pressure mercury lamp-UV cutoff filter ( $\lambda \geq 250$ nm)	Pt 1 wt%, 0.1 g, Top irradiation type reactor	100 mL aqueous solution sodium of sulfite (0.05 M)	500 $\mu\text{molg}^{-1}\text{h}^{-1}$	50% Bi/Fe incorporation by hydrothermal method gave high surface area, high crystallinity and Bi (V) species free solid solution.	[178]
2017	Sr <sub>0.9</sub> La <sub>0.1</sub> Ti <sub>0.9</sub> Cr <sub>0.1</sub> O <sub>3</sub>	2.31eV	300 W Xenon lamp ( $400 \leq \lambda \leq 700$ nm)	0.1 g, Gas closed circulation system	10 mL methanol + 4 g NaOH in 90 mL water	62.8 $\mu\text{molg}^{-1}\text{h}^{-1}$	Cr was responsible for photocatalytic activity. Sr based sample had shortest Ti-O bond length and proper Ti-O-Ti bond angle responsible for a wide band dispersion and a high charge mobility. Maximum H <sub>2</sub> was obtained at x = 0.003 by spray pyrolysis from polymeric precursor solutions and the induction period was also reduced to 33%	[180]
2013	Bulk-Na <sub>1-x</sub> La <sub>x</sub> Ta <sub>1-x</sub> Cr <sub>x</sub> O <sub>3</sub>	2.88eV	300 W Xe lamp ( $\lambda > 415$ nm)	Pt 0.5 wt%, 0.1 g, Pyrex closed gas circulation reactor	20% methanol	1467 $\mu\text{molg}^{-1}\text{h}^{-1}$	With 3 mol% the specific surface area and activity increased but above this it decreased due to recombination, limited solubility of doped ions in the CaTiO <sub>3</sub> is limited and more doped ions on surface of catalyst.	[181]
2012	Ca <sub>0.94</sub> Ag <sub>0.03</sub> La <sub>0.03</sub> TiO <sub>3</sub>	-	350 W high pressure Hg lamp-UV	0.1 g	5% methanol in 420 mL aqueous solution	1064 $\mu\text{molg}^{-1}\text{h}^{-1}$	Whereas, when x = 0.70, there was no suppression of Cr 3 d or reduction of band gap	[182]
2009	Bulk-Na <sub>1-x</sub> La <sub>x</sub> Ta <sub>1-x</sub> Cr <sub>x</sub> O <sub>3</sub>	-	300 W Xe lamp ( $\lambda > 420$ nm)	Pt 0.2 wt%, 0.5 g	50 mL CH <sub>3</sub> OH+220 mL H <sub>2</sub> O	9.0 $\mu\text{molg}^{-1}\text{h}^{-1}$	Specific composition-controlled activity. It was highest for x = 0.4, when, x = 0.60. The original O 2p orbitals of NaTaO <sub>3</sub> narrowed band gap with the increase in Cr content but the transition of photoelectrons within Cr 3d local levels was suppressed.	[183]

perovskites exhibit interesting optoelectronic and electronic properties as well as efficient charge transport [195]. Layered perovskite is classified into Aurivillius (AL) phase, Ruddlesden–Popper (RP) phase and Dion–Jacobsen (DJ) phase based on structure as discussed in the following section.

### 3.3.1. Dion–Jacobson (DJ) phase

Dion–Jacobsen (DJ) phase has formula A (Ln<sub>n-1</sub>Ta<sub>n</sub>O<sub>3n+1</sub>), where, A = K, Rb, Cs, Ag, and Ln = La, Pr, Nd, Sm and n = 2 and 3. Dion–Jacobsen (DJ) phase layered perovskites show extraordinary easy ion exchange, electron conductivity, dielectric properties and photoluminescence [196], however, these layered materials constitute wider band gaps ranging from 3.8 to 4.3 eV, making them active only UV irradiation [197]. Also, these layered structures show improved photocatalytic activity, however, due to limitations of narrow band gap [198], recombination of charge carriers [199] and low visible light harvesting [200], these structures should be improved. These materials can be easily modified as their layered structure allows better distribution of dopant [201]. The efficiency of layered structure can be improved by forming Z-scheme with other materials. The issues in classic photocatalytic systems can be controlled by Z-scheme as it promotes charge separation and redox reactions. Z-scheme mechanism is identical to the natural photocatalysis, where, series linkage of two semiconductors (PS I and PS II) helps retaining of electrons at higher reduction potential and holes at higher oxidation potential involving active sites. All the three types of Z-scheme including direct Z-scheme, Z-scheme with shuttle redox mediator and with solid state electron mediator promote efficient electron transfer. Direct Z-scheme promotes transfer of electrons by direct

solid to solid contact. The major difference between Z-scheme with shuttle redox mediator and with solid state electron mediator is the presence of redox couple ions acting as electron transporter and presence of solid electron linker transporting electrons by ohmic contact, respectively [202]. Yet, not many studies are focused on effective charge transfer for photocatalytic H<sub>2</sub> production in perovskite through Z-scheme with shuttle redox mediator, solid state electron mediator and direct Z-scheme.

Direct Z-scheme system without redox mediators consist of two photocatalysts (SPP I and SPP II). SPP I constitute a higher VB than VB of SPP II, while, SPP II has a CB lower than CB of SPP I for formation of heterojunction. Upon irradiations from light source, recombination of photogenerated electrons from SPP II with holes from SPP I takes place at interface of heterojunction as shown in Fig. 10 (a). The trapping of electrons for reduction and holes for oxidation leads to effective photoactivity. Moreover, it also assists towards hindering of backward reaction as well as minimizes shielding effect. Improved water splitting was studied for SrTiO<sub>3</sub>:La/Rh in combination with Ir/CoO<sub>x</sub>/Ta<sub>2</sub>N<sub>5</sub> with 5 times more activity than SrTiO<sub>3</sub>:Rh [203].

In Z-scheme with redox mediator, two semiconductor perovskite photocatalysts (SPP I and SPP II) are linked together by an acceptor (A) and donor (D) pair rather than physical interaction as shown in Fig. 10 (b). Redox mediators comprise of IO<sub>3</sub>/ $\text{I}$ , Co<sup>3+</sup>/Co<sup>2+</sup>, Fe<sup>3+</sup>/Fe<sup>2+</sup> and NO<sub>3</sub>/NO<sub>2</sub>. Light irradiations initiate forward reaction of H<sub>2</sub> and O<sub>2</sub> generation in particular photosystem. Redox mediator supports the migration of photogenerated electrons from perovskite photocatalyst responsible for O<sub>2</sub> production to H<sub>2</sub> producing perovskite photocatalyst. Usually, backward reaction takes place in concurrent production of O<sub>2</sub> and H<sub>2</sub> as

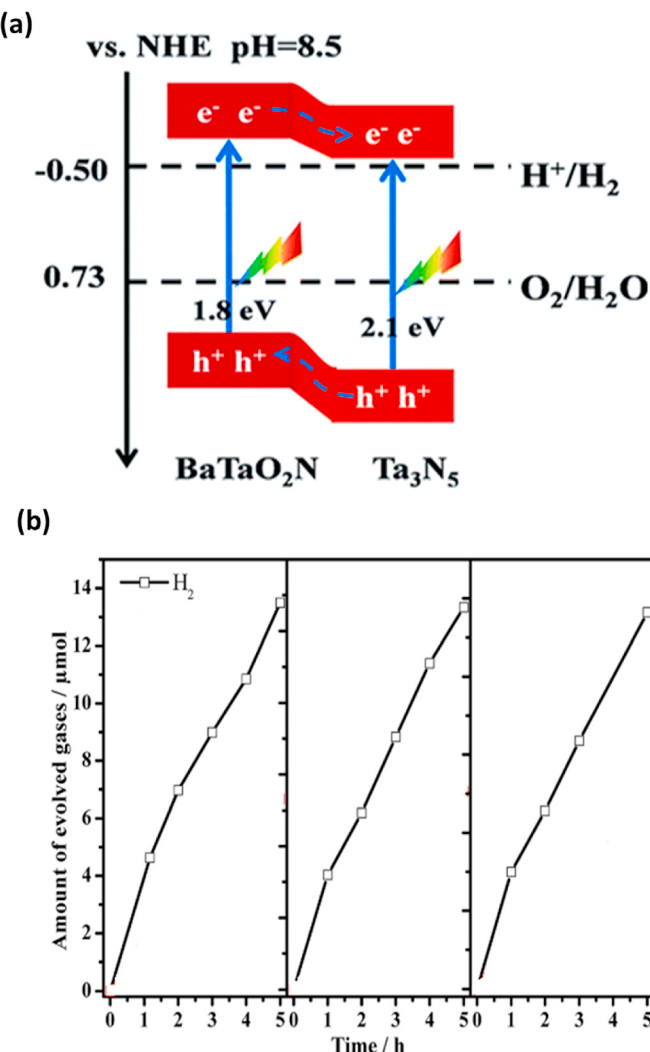


Fig. 9. (a) Band structure characterization of the Ta<sub>3</sub>N<sub>5</sub> and BaTaO<sub>2</sub>N sample; (b) Multiple cycles of H<sub>2</sub> production with 0.5 wt% Pt/Ba (0.3)-Ta<sub>3</sub>N<sub>5</sub> [189].

the electrons react with the acceptor and donor pair leading to reduce quantity of excited electrons and holes [204]. In a study, water splitting under visible light was achieved by H<sub>2</sub> evolving Pt/BaTiO<sub>3</sub>:Rh and O<sub>2</sub> photocatalyst PtO<sub>x</sub>-loaded WO<sub>3</sub> in presence of IO<sup>3-</sup>/I<sup>-</sup> shuttle redox mediator [205]. In another study, photocatalytic water splitting was carried out by H<sub>2</sub> evolving BaZrO<sub>3</sub>-BaTaO<sub>2</sub>N fabricated by Pt nanoparticles in combination with O<sub>2</sub> evolving TiO<sub>2</sub> or PtO<sub>x</sub>/WO<sub>3</sub> in the presence of IO<sup>3-</sup>/I<sup>-</sup> pair as redox shuttle mediator [206]. In another work, Li et al. [169], investigated LaNi<sub>1-x</sub>Cu<sub>x</sub>O<sub>3</sub> with appropriate amount of Cu<sup>2+</sup>/Cu<sup>1+</sup> redox couples which favored band gap narrowing and also increased the migration time of photo-induced charge carriers from the VB to CB.

Z-scheme photocatalytic system with solid electron mediator consist of two semiconductor perovskite photocatalysts (SPP I and SPP II), where solid electron mediator is present at the interface. Improved H<sub>2</sub> production has been reported based on the efficient charge carrier's transfer and separation by carbon based rGO and noble metals such as Ag and Au. This type of Z-scheme is formed when one semiconductor perovskite constitutes a more negative CB and more positive VB. Moreover, the noble metals acting as solid electron mediator also induce Surface Plasmon Resonance effect (SPR) for more effective photoactivity. Also, the backward reaction is inhibited by Z-scheme involving solid electron mediator [207]. For instance, Z-scheme with solid state electron mediator has been reported where, rGO transferred

photogenerated electrons from BiVO<sub>4</sub> acting as O<sub>2</sub> generating photocatalyst to Ru/SrTiO<sub>3</sub>: Rh acting as H<sub>2</sub> generating perovskite photocatalyst as shown in Fig. 10 (c). This enhanced visible light water splitting was because of the three times increased charge carries consumption [208]. Detailed information on Z-scheme with redox mediator of perovskites has been included in Sub-section 4.2.1 Graphene and Reduced Graphene Composites.

In this perspective, Wei et al. [209], studied the increase in photocatalytic activity of HCa<sub>2</sub>TaNb<sub>3</sub>O<sub>10</sub> under UV light when intercalated with ZnS and PbS. Fig. 10 (d) illustrates the band gap structure according to band energies of HCa<sub>2</sub>TaNb<sub>2</sub>O<sub>10</sub>, ZnS and PbS which were determined from position of conduction and valence band of the respective semiconductors. It also depicts that the photo-generated electrons in CB of ZnS and PbS were transferred to higher potential CB of HCa<sub>2</sub>TaNb<sub>2</sub>O<sub>10</sub>, while, transferring the holes in VB of HCa<sub>2</sub>TaNb<sub>2</sub>O<sub>10</sub> to lower potential VB of ZnS, thus facilitating separation of charge carriers. The rate of hydrogen evolution was increased significantly by intercalation of perovskite's interlayer spaces with ZnS and PbS as shown in Fig. 10 (e). Layered Dion–Jacobson phase Rb<sub>2</sub>La<sub>2</sub>Ti<sub>3</sub>O<sub>10</sub> was prepared by solid-state method. With substitution of silver cations, there was a decreased in optical band gap sizes and potential active sites on the surface were increased [210]. Wang et al. reported band gap reduction of UV active La<sub>2</sub>Ti<sub>2</sub>O<sub>7</sub> having band gap of 3.8 eV due to formation of electron donor levels inside the intrinsic band gap of La<sub>2</sub>Ti<sub>2</sub>O<sub>7</sub> by Rh<sup>3+</sup> ions doping [211].

On the whole, HCa<sub>2</sub>TaNb<sub>3</sub>O<sub>10</sub>/(ZnS, PbS) Z-Scheme was observed to produce highest and enhanced rate of H<sub>2</sub> production under UV irradiation. This was obviously due to the efficient electron hole pairs separation. Also, Dion–Jacobson layered perovskites like Rb<sub>2</sub>La<sub>2</sub>Ti<sub>3</sub>O<sub>10</sub> normally depicts hydration and interlayer space expansion which is responsible for improved H<sub>2</sub> production as it allowed proper movement of methanol-water mixture.

### 3.3.2. Ruddlesden–Popper (RP) phase

Layered perovskite can be classified into (100) layered Ruddlesden–Popper phase (RP) having a general formula of A<sub>n-1</sub>A'<sub>1</sub>B<sub>n</sub>X<sub>3n+1</sub>. Here, (100) layered has the interlayer in parallel with (100) plane of a bulk type perovskite structure. Similarly, (110) layered perovskite has a general formula A<sub>n</sub>B<sub>n</sub>O<sub>3n+2</sub>, where, A = Sr, La and B = Ta, Nb, Ti and n = 4, 5. They consist of perovskite slabs, placed parallel to (110) face. The (110) plane structure can be classified further into (111) plane-type structures due to the plane defect structure of perovskite crystal structure having a general formula A<sub>5</sub>B<sub>4</sub>O<sub>15</sub>, where, A = Ba, Sr and B = Nb, Ta. 100). These layered structures have a wide band gap of 3.9–4.1 eV, however, H<sub>2</sub> production has been reported to enhance by modification of (100) layered Ruddlesden–Popper phase. For instance, Huang et al. [212], studied nitrogen doping and observed decrease in band gap of K<sub>2</sub>La<sub>2</sub>Ti<sub>3</sub>O<sub>10</sub> from 3.69 to 3.44 eV. Composite of Ba<sub>5</sub>Ta<sub>4</sub>O<sub>15</sub>/Ba<sub>3</sub>Ta<sub>5</sub>O<sub>15</sub> showed 160% higher hydrogen evolution as compared to the pure Ba<sub>5</sub>Ta<sub>4</sub>O<sub>15</sub> in the presence of Rh. The Ba<sub>3</sub>Ta<sub>5</sub>O<sub>15</sub> conduction band was located at lower potential than Ba<sub>5</sub>Ta<sub>4</sub>O<sub>15</sub>, thus, photo-excited electrons were effectively transferred from the conduction band of Ba<sub>5</sub>Ta<sub>4</sub>O<sub>15</sub> to Ba<sub>3</sub>Ta<sub>5</sub>O<sub>15</sub>, resulting in hindered recombination rate and improved photo-activity [213]. Likewise, a network of octahedral La<sub>2</sub>Ti<sub>2</sub>O<sub>7</sub> doped with Rh<sup>3+</sup> boosted the mobility of charge carriers which led to higher photocatalytic activity for water splitting and also showed stronger light absorption [214]. In another work, Kim et al. [215], investigated that the doping W<sup>6+</sup> into p-type PbBi<sub>2</sub>Nb<sub>2</sub>O<sub>9</sub> which resulted in increased electron-hole pairs separation and photocatalytic activity due to high electron density.

### 3.3.3. Aurivillius (AL) phase

Aurivillius structures are subgroups of layered perovskite denoted as (Bi<sub>2</sub>O<sub>2</sub>)<sub>2</sub>+(A<sub>m-1</sub>B<sub>m</sub>O<sub>3m+1</sub>)<sup>2-</sup>. The structure of Aurivillius contains 12-fold coordinated one to three valence A ions in crystal lattice. Whereas, B ion located in octahedron consist of transition ion having high valence.

**Table 5**

Hydrogen production and photocatalytic reaction conditions for oxynitrides.

Year	Catalyst/composite	Band gap	Light intensity	Co-catalyst, Loading of catalyst, Reactor	Reagent	H <sub>2</sub> production	Comments	Ref.
2017	Ta <sub>3</sub> N <sub>5</sub> /BaTaO <sub>2</sub> N	-	300 W xenon lamp ( $\lambda > 420$ nm)	Pt 0.5 wt%, 0.15 g, Pyrex top irradiation type reaction	150 mL aq. sol with 20% methanol	21.3 $\mu\text{mol g}^{-1}\text{h}^{-1}$	Z-scheme favored electron separation and highest H <sub>2</sub> was for 0.3 Ba	[189]
2014	LaTiO <sub>2</sub> N	2.1 eV	visible light irradiation with a Xe lamp ( $\lambda \geq 420$ nm)	3 wt% Pt, 0.1 g	20 vol% methanol 100 mL aqueous solution	600 $\mu\text{mol g}^{-1}\text{h}^{-1}$	0.25-min aqua regia treatment of LaTiO <sub>2</sub> N doubled the H <sub>2</sub> . Without it the photo excited electrons did not migrated to the Pt cocatalyst	[191]
2012	CaTaO <sub>2</sub> N	-	300 W Xe lamp ( $\lambda > 420$ nm)	0.3 wt% Pt, 0.1 g, Pyrex top irradiation reaction vessel	100 mL aqueous solution with methanol	83 $\mu\text{mol g}^{-1}\text{h}^{-1}$	CaTaO <sub>2</sub> N prepared by layered Ca-Ta oxide gave aggregated nanoparticles, lower density of anionic defects and better activity	[192]
2011	CaNbO <sub>2</sub> N	2.0 eV	Xe lamp (300 W) fitted with a cutoff filter ( $\lambda > 420$ nm)	Pt 1 wt%, 0.1 g, Pyrex top irradiation reaction vessel	Aqueous solution of 90 mL and 10 mL methanol	10 $\mu\text{mol g}^{-1}\text{h}^{-1}$	1023 K was optimal temperature for nitridation. Above this, niobium species were produced, which act as recombination centers	[190]
2012	CaTaO <sub>2</sub> N	-	300 W Xe lamp ( $\lambda > 420$ nm)	0.3 wt% Pt, 0.1 g, Pyrex top irradiation reaction vessel	100 mL aq. sol with methanol	83 $\mu\text{mol h}^{-1}\text{g}^{-1}$	CaTaO <sub>2</sub> N prepared by layered Ca-Ta oxide gave aggregated nanoparticles, lower density of anionic defects and better activity	[192]
2009	BaTaO <sub>2</sub> N	2.0 eV	300 W xenon lamp ( $\lambda > 420$ nm)	0.3 wt% Pt, 0.1 g, Pyrex reaction vessel	250 mL aq. sol of 50 mL of methanol or iodide (I <sup>-</sup> )	500 $\mu\text{mol g}^{-1}\text{h}^{-1}$	It is an example of overall water splitting system by light of wavelengths longer than 600 nm. H <sub>2</sub> increased when preparation temperature was from 1123 to 1223 K	[193]
2004	Octahedral-CaTaO <sub>2</sub> N	2.5 eV	300 W xenon lamp ( $\lambda > 420$ nm)	0.05 wt% Ru, 0.1 g, Pyrex reaction vessel	250 mL aqueous solution with 50 mL of methanol	200 $\mu\text{mol g}^{-1}\text{h}^{-1}$	Ru was better than Pt as the interface electronic structure between Ru particles and TaON facilitated electron transfer	[194]

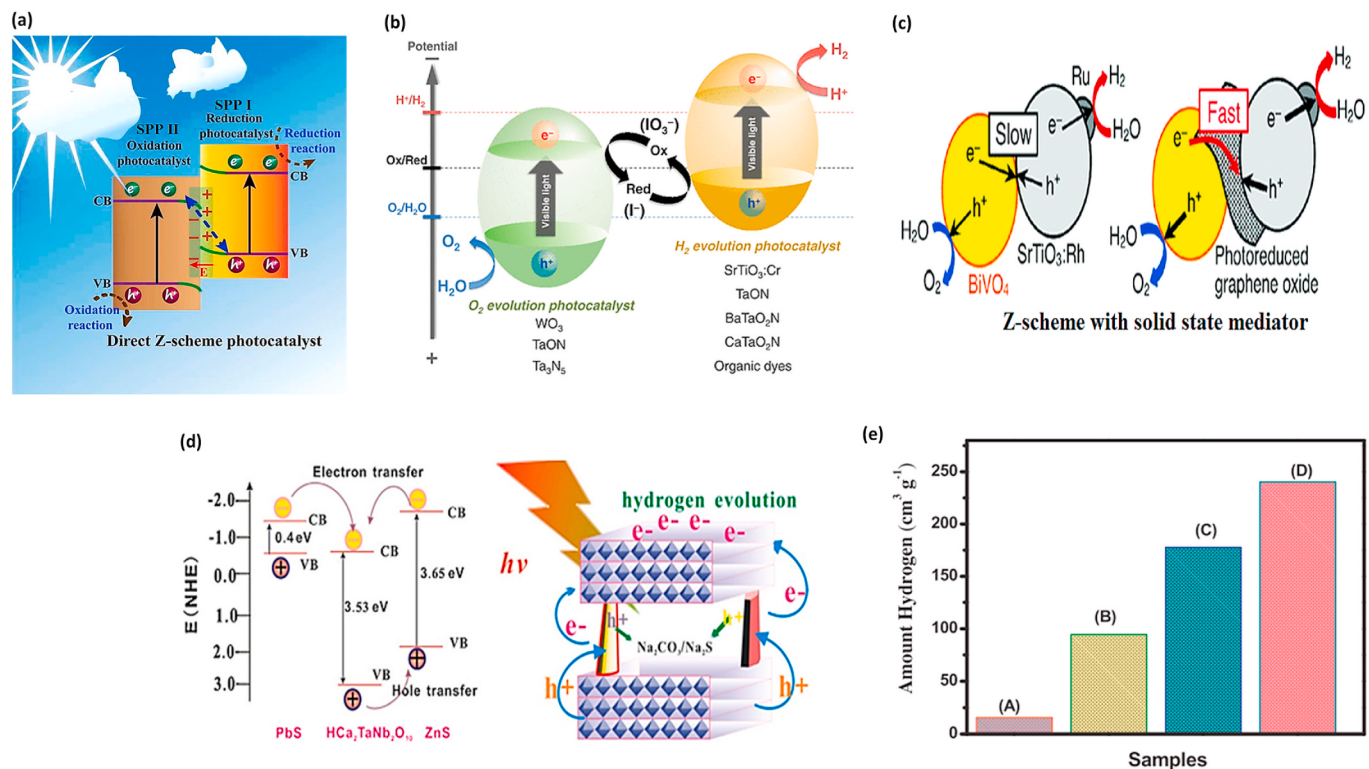


**Fig. 10.** (a) Direct Z-scheme for charge separation in water splitting reaction [216]; (b) Z-Scheme water splitting of H<sub>2</sub> and O<sub>2</sub> with redox mediators for charge separation [217]; (c) Z-scheme with solid state mediator as rGO for BiVO<sub>4</sub> acting as O<sub>2</sub> generating photocatalyst to Ru/SrTiO<sub>3</sub>:Rh [208] (d) Conduction and valence band edges vs. normal hydrogen electrode (NHE, at pH = 0) and Illustration of charge transfer and separation in HCa<sub>2</sub>TaNb<sub>2</sub>O<sub>10</sub>/(ZnS, PbS); (e) Amount of H<sub>2</sub> produced from (A) HCa<sub>2</sub>Nb<sub>3</sub>O<sub>10</sub>, (B) HCa<sub>2</sub>TaNb<sub>2</sub>O<sub>10</sub>, (C) HCa<sub>2</sub>Nb<sub>3</sub>O<sub>10</sub>/(ZnS, PbS) and (D) HCa<sub>2</sub>TaNb<sub>2</sub>O<sub>10</sub>/(ZnS, PbS) [209].

$(\text{Bi}_2\text{O}_2)^{2+}$  layer and number of slabs (denoted by m) determine immense polarization in the structure [218]. Aurivillius structures are observed to show photocatalytic activity, however, wide band gap [219] leading to insignificant visible light photoactivity [220] and electron hole pairs recombination [199] hinders its practical applications.

Heterostructured Z-scheme of 2D  $\text{Bi}_2\text{WO}_6$  nanosheets with CdS nanowires was studied to improve photoactivity. Fig. 11 (a) depicts the transfer of photoexcited electrons in VB of  $\text{Bi}_2\text{WO}_6$  to CB of CdS and further transfer to Pt metal for  $\text{H}_2$  production reaction by reacting with  $\text{H}^+$  ions. Photodecomposition oxidation of  $\text{CH}_3\text{COOH}$  took place on the surface of  $\text{Bi}_2\text{WO}_6$ . High rate of  $1223 \mu\text{mol g}^{-1} \text{h}^{-1}$   $\text{H}_2$  was generated because of sufficient reaction sites and synergistic effect when  $\text{Bi}_2\text{WO}_6/\text{CdS}$  heterostructure was formed as illustrated in Fig. 11 (b) [221]. Similarly, Jiang et al. investigated band gap reduction by co-doping as band gap of pristine  $\text{Bi}_3\text{TiNbO}_9$  (3.1 eV) was reduced by 1 eV upon Cr/Nb co-doping. The persistence of oxidation state ( $\text{Cr}^{3+}$ ) of Cr also helped in maintaining charge balance. Also, electron hole recombination was minimized by  $[\text{BiTiNbO}_7]^{2-}$  slabs in perovskite structure [222]. Similarly, Zhang et al. reported decreased band gap of  $\text{Bi}_4\text{Ti}_3\text{O}_{12}$  from 1.81 eV to 1.3 eV upon Cr doping to form  $\text{Bi}_4\text{Ti}_3-x\text{Cr}_x\text{O}_{12}$ . This was due to the formation of  $\text{Cr} 3d + \text{Bi} 6p + \text{Ti} 3d$  orbital and localized Cr 3d band in CB and middle of band gap of  $\text{Bi}_4\text{Ti}_3\text{O}_{12}$ , respectively [223].

Recent progress in layered perovskite has been summarized in Table 6. (111) layered structure showed improved activity as the spacing between perovskite layers made diffusion of dopant proficiently. On the whole, Ag and N were found to be the best metal and non-metal respectively to enhance photocatalytic activity.

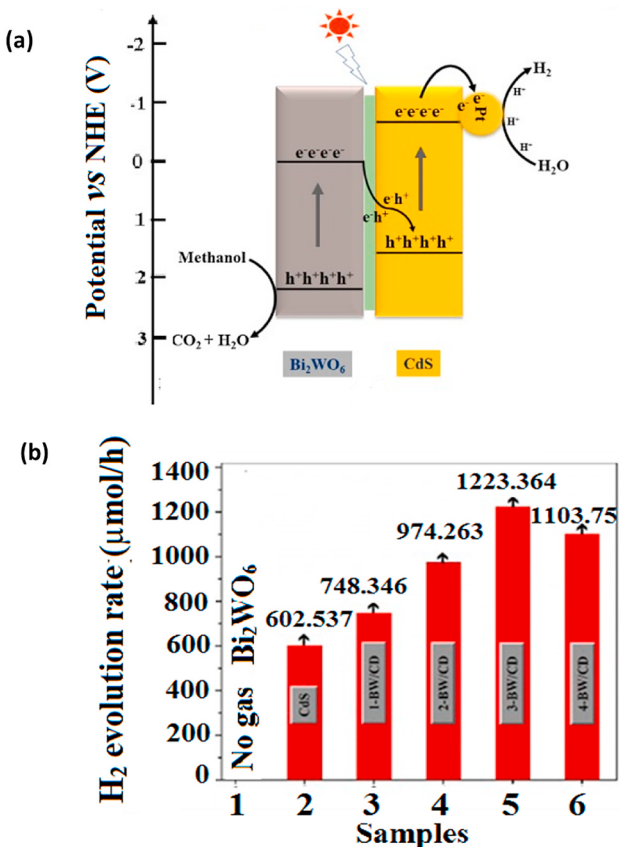


Fig. 11. (a) Schematic photocatalytic  $\text{H}_2$  evolution over  $\text{Bi}_2\text{WO}_6/\text{CdS}$  in Z-scheme photocatalytic system under visible light illumination; (b) Comparison of photocatalytic  $\text{H}_2$  evolution over  $\text{Bi}_2\text{WO}_6$ , pristine CdS nanowires and  $\text{Bi}_2\text{WO}_6/\text{CdS}$  under different mole ratio [221].

### 3.4. Halide perovskites

Typically, 3D halide perovskite materials have a cubic crystal structure similar to  $\text{CaTiO}_3$ , which can be denoted by formula  $\text{ABX}_3$ , where, A and B are cations and X represents an anion. In  $\text{ABX}_3$  structure, the eight corners of cube are occupied by A cation with  $\text{BX}_6$  as corner sharing octahedral complex. Halide perovskites consist of monovalent small cations such as formamidinium (FA), rubidium (Rb), methyl-ammonium (MA) or cesium (Cs) occupying A site in perovskite's structure. B site in structure of perovskite is occupied normally by tin (Sn), germanium (Ge) or lead (Pb), while X site is occupied by halides including Bromine (Br), Chlorine (Cl), Iodine (I) as demonstrated in Fig. 12 (a). The properties of perovskite's crystal structure influencing the electronic and optical properties can be altered notably by varying the constituent elements [234]. A site is normally occupied by MA;  $\text{CH}_3\text{NH}_3^+$  due to increased symmetry based on its larger size. Moreover, it is also responsible for narrowing band gap leading to increased light absorption. Moreover, FA  $\text{HC}(\text{NH}_2)_2^+$  on A site results in more symmetry as compared to MA. In this context,  $\text{FAPbI}_3$  is reported to have 1.4 eV band gap with higher visible light absorption, however, interaction of FA-I ion is reported to be distorted and it also shows poor band alignment [235]. Firstly,  $\text{CsSnI}_3$  perovskite with  $\text{Cs}^+$  at A site was reported to have p type semiconductor performance with holes having high mobility [236]. Moreover, in comparison to MA,  $\text{Cs}^+$  has a smaller size, which causes octahedral tilting leading to less symmetry as well as constitutes a wider band gap. For instance,  $\text{CsPbI}_3$  has a wide band gap of 1.73 eV in comparison to  $\text{MAPbI}_3$  with 1.57 eV band gap [237]. Mixing of A site cation can also be carried out in halide perovskite as for the first time Pellet and co-workers reported A site mixing of MA and FA(x) in different ratios to yield  $(\text{MA})_x(\text{FA})_{1-x}\text{PbI}_3$  for optoelectronic applications. In case of B site cations, the stability decreases in order  $\text{Pb} > \text{Sn} > \text{Ge}$ , but increase in electronegativity and decrease in band gap is observed in order  $\text{Ge} > \text{Sn} > \text{Pb}$ . Thus, mixed B site such as  $\text{MASn}_{1-x}\text{Pb}_x\text{I}_3$  perovskite for solar device applications have been studied with tunable band gap by adjusting ratio of Pb and Sn [238]. X site in perovskite occupied by iodide ( $\text{I}^-$ ) leads to stable structure as  $\text{I}^-$  has similar characteristics as Pb and is the most studied perovskite. Chlorine (Cl) at X site has been reported to improve charge carrier's lifetime and diffusion lengths. Bromide (Br) has been reported for band gap tuning of perovskites, but induce structural distortion causing increase in band gap. Likewise fluoride (F) has been observed to induce lattice strain in structure leading to lower light absorption ability [239].

$\text{CH}_3\text{NH}_3\text{PbI}_3$  is the most commonly studied organic lead perovskite. As shown in Fig. 12 (b), inorganic perovskite originates, when A site in the structure of perovskite is occupied by inorganic species like  $\text{Cs}^+$  and organic perovskites are formed when A site is occupied by organic species like  $\text{CH}_3\text{NH}_3^+$ . Also, A site inorganic species induce spherical symmetry in the structure, while non-spherical symmetry is induced by organic species [240]. Inorganic perovskites comprising of Ti and Ta are effective towards photocatalytic  $\text{H}_2$  production, however, lack of stability leads to insignificant research on inorganic perovskites [241]. Changes in molar ratio of precursor in organic-inorganic perovskites can be adjusted to tune the structural dimensionality for obtaining structures including 0D  $(\text{CH}_3\text{NH}_3)_4\text{PbX}_6\text{H}_2\text{O}$ , 1D  $\text{C}_5\text{H}_{10}\text{NH}_2\text{PbX}_3$ , 2D  $\text{CnH}_{2n+1}\text{NH}_3\text{PbX}_4$  and 3D  $\text{CH}_3\text{NH}_3\text{PbX}_3$  [242]. Halide perovskites have excellent optoelectronic properties that enable the utilization of the full solar spectrum and efficient charge transportation. Halide perovskites show much longer absorption edge ( $\sim 700$  nm for  $\text{MAPbI}_3$ ) than oxide perovskites ( $\sim 200$  nm) or oxynitrides perovskites ( $\sim 650$  nm). This is because of the strong antibonding coupling of s orbitals at B site with p orbital at X site of perovskite's structure [243]. Moreover, halide perovskites are considered for photoactivity based on their high absorption coefficient, long life of charge carriers, short exciton binding energy and stable movement of charge carriers [244–247]. The VB of halide perovskites is dominated by np orbitals of X site, while, the CB is dominated by 6 p orbitals of B site cations. Thus, the VB and CB are not

**Table 6**

Hydrogen production and photocatalytic reaction conditions for layered perovskites.

Year	Catalyst/composite	Band gap	Light intensity	Co-catalyst, loading of catalyst, Reactor	Reagent	H <sub>2</sub> production	Comments	Ref.
2019	Bi <sub>2</sub> WO <sub>6</sub> /CdS	–	300 W Xe arc lamp ( $\lambda \geq 420$ nm)	-Pt 0.6 wt%, 0.02 g	100 mL aqueous solution with 25% methanol	1223 $\mu\text{molg}^{-1}\text{h}^{-1}$	Z-scheme between Bi <sub>2</sub> WO <sub>6</sub> /CdS promoted activity by efficient oxidizing ability and stability.	[221]
2018	Ag/Bi <sub>2</sub> WO <sub>6</sub> -GO	–	300 W high-pressure mercury lamp-UV	0.05 g, quartz cell (100 mL)	100 mL aqueous solution with Sodium sulfide nanohydrate (0.1 M), sodium sulfite (0.04 M), and sodium chloride (3 M)	83.3 $\mu\text{molg}^{-1}\text{h}^{-1}$	1.5 wt% graphene and AgNO <sub>3</sub> precursor 2 mM showed highest H <sub>2</sub> as Ag narrowed band gap and Bi <sub>2</sub> WO <sub>6</sub> and GO controlled charge separation.	[224]
2017	Bi <sub>4</sub> Ti <sub>3</sub> O <sub>12</sub> /I-BiOCl	2.8eV	$\lambda > 420$ nm	0.05 g-	80 mL aqueous solution with 25 vol % methanol	91.7 $\mu\text{molg}^{-1}\text{h}^{-1}$	2D/2D heterojunction interface provided contact surface which increased charge transfer	[225]
2017	Ba <sub>3-x</sub> LaxTa <sub>5</sub> O <sub>14-x</sub> N <sub>1+x</sub>	–	300 W Xe-arc lamp ( $\lambda > 420$ nm)	0.3 wt% Pt 0.1 g, reaction vessel with a top-window	150 mL of reactant solution with 20 vol% methanol	30 $\mu\text{molg}^{-1}\text{h}^{-1}$	Highest H <sub>2</sub> was of samples annealed in 5% NH <sub>3</sub> atmosphere	[226]
2017	r-Sr <sub>4</sub> FeTaO <sub>6</sub>	2.01eV	500 W high-pressure mercury lamp ( $\lambda \geq 400$ nm).	1 wt% Pt, 0.1 g, top-irradiation-type reactor	100 mL aqueous solution with 0.05 M sodium sulfite	1070 $\mu\text{molg}^{-1}\text{h}^{-1}$	structural lamination by reducing inter-layer recombination of charge is character of RP compound	[227]
2017	CsCa <sub>2</sub> Nb <sub>3</sub> O <sub>10</sub>	3.6eV	50 W Hg immersion lamp -UV	0.05 wt% Rh, 0.3 g, double-walled inner irradiation type quartz reactor	600 mL aqueous methanol (10% v/v) solution	5666.6 $\mu\text{molg}^{-1}\text{h}^{-1}$	Activity mainly depended on A cations i.e., conduction band level as well as their structural anisotropy, although, Ca had highest conduction band minimum but showed activity due to largest driving force for proton reduction	[201]
2017	Na <sub>2</sub> ZrTi <sub>5</sub> O <sub>13</sub>	3.62eV	pen-ray lamp (UVP, 254 nm and 4400 $\mu\text{W}/\text{cm}^2$ )	0.1 g, Pyrex reactor of V = 250 mL	200 mL deionized water	1896 $\mu\text{molg}^{-1}\text{h}^{-1}$	Zr <sup>4+</sup> caused efficient charge transport by structural distortion of octahedral sites	[228]
2014	HCa <sub>2</sub> TaNb <sub>2</sub> O <sub>10</sub> /(ZnS, PbS)	3.53eV	300 W Hg lamp-UV	1.0 g, Pyrex reactor of V = 500 cm <sup>3</sup>	200 mL Na <sub>2</sub> S and Na <sub>2</sub> SO <sub>3</sub> aqueous solution	11,200 $\mu\text{molg}^{-1}\text{h}^{-1}$	Activity was due to guest-to-host separation of charges and substitution of Ta for partial Nb which caused higher conduction band	[209]
2013	Plate like-Rh-doped La <sub>2</sub> Ti <sub>2</sub> O <sub>7</sub>	–	300 W Xe lamp fitted with a cutoff filter ( $\lambda > 420$ nm)	Pt 0.3 wt%, 0.3 g, Pyrex top irradiation type vessel	150 mL aqueous solution, with 10 vol% methanol	.8.3 $\mu\text{molg}^{-1}\text{h}^{-1}$	MSS method yielded a higher photocatalytic activity than the SSR and PC	[229]
2013	N doped Sr <sub>5</sub> Ta <sub>4</sub> O <sub>15</sub>	2.2eV	300 W Xenon lamp $\lambda > 420$ nm	Pt 0.3 wt%, 0.15 g, Pyrex top irradiation-type reaction vessel	20% methanol 150 mL aqueous solution.	91.7 $\mu\text{molg}^{-1}\text{h}^{-1}$	H <sub>2</sub> was due to substitution of oxygen by nitrogen for forming Ta-N bonds	[230]
2013	Ba <sub>5</sub> Ta <sub>4</sub> O <sub>15</sub> /Ba <sub>3</sub> Ta <sub>5</sub> O <sub>15</sub>	4.5 eV	700 W Hg mid-pressure immersion lamp-UV	Rh 0.025 wt%, 0.5 g, inner irradiation type quartz reactor	550 mL water and 50 mL methanol.	3770 $\mu\text{molg}^{-1}\text{h}^{-1}$	composite via the sol-gel citrate route showed better activity than Ba <sub>5</sub> Ta <sub>4</sub> O <sub>15</sub> prepared by SSR method	[213]
2013	AgCa <sub>2</sub> Nb <sub>3</sub> O <sub>10</sub>	3eV	1000 W Xe arc lamp visible filter ( $\lambda > 420$ nm)	1 wt% Pt, 0.15 g, Outer irradiation type fused-silica reaction cell with a volume of 70 mL	20% aqueous methanol solution.	13,616 $\mu\text{molg}^{-1}\text{h}^{-1}$	Interlayer spacing substitution of Ruddlesden popper by silver increased valence band maximum and reduced bandgap	[210]
2013	Rh/La <sub>2</sub> Ti <sub>2</sub> O <sub>7</sub>	3.8eV	300 W Xe lamp ( $\lambda > 420$ nm)	Pt 0.5 wt%, 0.3 g, Pyrex top irradiation type vessel	10 vol% methanol in 150 mL aqueous solution	8.33 $\mu\text{mol g}^{-1}\text{h}^{-1}$	In comparison to SSR and PC, MSS method gave better activity as it induced larger surface area and crystallinity, higher phase purity as well as more absorption of light by Rh <sup>3+</sup> ions.	[229]
2011	N-Ba <sub>5</sub> Ta <sub>4</sub> O <sub>15</sub>	1.78eV	simulated sunlight (AM1.5, 1000 $\text{Wm}^{-2}$ )	0.1 wt% Pt, 0.1 g, 25 cm <sup>2</sup> quartz cell	10 mL of 20 vol % methanol	4950 $\mu\text{molg}^{-1}\text{h}^{-1}$	Improved H <sub>2</sub> was due to intergallery spacing between Ba <sub>5</sub> Ta <sub>4</sub> O <sub>15</sub> layers which helped N to diffuse	[231]
2010	N/K <sub>2</sub> La <sub>2</sub> Ti <sub>3</sub> O <sub>10</sub>	3.44eV	100 W mercury lamp ( $\lambda > 290$ nm)	1 g, 500 mL pyrex reactor	5% methanol solution	2.4 $\mu\text{molg}^{-1}\text{h}^{-1}$	It also showed visible light activity but was less but N	[212]

(continued on next page)

**Table 6 (continued)**

Year	Catalyst/composite	Band gap	Light intensity	Co-catalyst, loading of catalyst, Reactor	Reagent	H <sub>2</sub> production	Comments	Ref.
2008	PbBi <sub>2</sub> Nb <sub>2-x</sub> W <sub>x</sub> O <sub>9</sub>	2.74 eV	450 Watt, Xe-Arc lamp ( $\lambda \geq 420$ nm)	0.1 wt % Pt, 0.3 g	10 mL methanol with distilled 170 mL H <sub>2</sub> O	51 $\mu\text{mol g}^{-1}\text{h}^{-1}$	doping helped to narrow band gap	[215]
2006	NiO/Sr <sub>3</sub> Ti <sub>2</sub> O <sub>7</sub>	–	400 W high pressure Hg lamp UV	1 g, inner irradiation-type quartz cell	475 mL distilled water	83 $\mu\text{mol g}^{-1}\text{h}^{-1}$	N type doping with higher electron density ( $\text{W}^{6+}$ at Nb <sup>5+</sup> ) showed efficient charge separation	[232]
2005	Cr/La <sub>2</sub> Ti <sub>2</sub> O <sub>7</sub>	–	450 W high-pressure Hg lamp ( $\lambda > 420$ nm)	1.0 wt Pt, inner irradiation quartz reaction cell	500 mL distilled H <sub>2</sub> O	15 $\mu\text{mol g}^{-1}\text{h}^{-1}$	1 wt% of Ni increased the activity of Sr <sub>3</sub> Ti <sub>2</sub> O <sub>7</sub> prepared by PCM as compared to solid state method due to more surface area and high purity of prepared sample (Cr/La) 0.01 contributed in electronic band structure of La <sub>2</sub> Ti <sub>2</sub> O <sub>7</sub> by forming partially filled 3 d band.	[233]

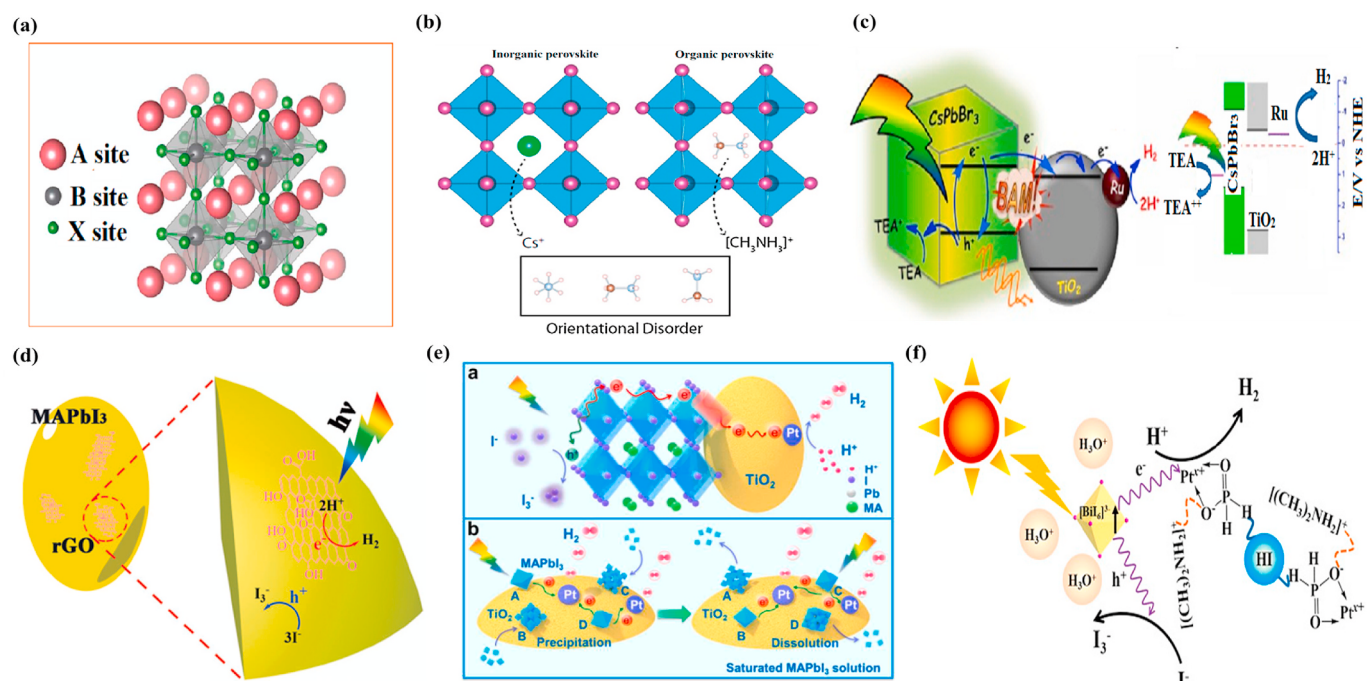


**Fig. 12.** (a) Crystal structure of cubic halide perovskite (ABX<sub>3</sub>) [234]; (b) Crystal structure of organic and inorganic halide perovskite [238]; (c) Schematic representation of the electron transfer processes and band structure energy diagram of the CsPbBr<sub>3</sub> and Ru@TiO<sub>2</sub>, as well as redox potentials of the sacrificial electron donor and proton reduction [249]; (d) Schematic illustration of the H<sub>2</sub> evolution using MAPbI<sub>3</sub>/rGO [253]; (e) Photocatalytic H<sub>2</sub> production along with effective transfer of photogenerated electrons and vigorous contact between MAPbI<sub>3</sub> and TiO<sub>2</sub>/Pt in HI aqueous solution due to dissolution and re-precipitation of MAPbI<sub>3</sub> [256]; (f) Proposed mechanism for photocatalytic hydrogen generation from [(CH<sub>3</sub>)<sub>2</sub>NH<sub>2</sub>]<sub>3</sub>[BiI<sub>6</sub>] with dominant [BiI<sub>6</sub>]<sup>3-</sup> inorganic framework [265].

influenced by the A site cations, making halide perovskites easy to be tuned for efficient photocatalytic activity by varying B site and X site ions. Perovskites have been distinguished on the basis of organic and inorganic lead-based perovskites and lead-free perovskites. Lead-based perovskites (B site) are more stable and are show more improved performance as compared to tin (B site) based perovskites. Germanium based perovskites are insignificantly studied due to highly unstable 2<sup>+</sup> oxidation state [248]. Thus, organic-inorganic lead-based and lead-free perovskites are discussed in the following Sub-sections.

#### 3.4.1. Lead based halide perovskites

Currently, organic-inorganic lead halide perovskites are known to possess extraordinary properties for next-generation hydrogen production applications and are considered as direct band gap perovskite

semiconductors [249]. Organic lead trihalide perovskites such as MAPbX<sub>3</sub> (MA = CH<sub>3</sub>NH<sub>3</sub><sup>+</sup>, X = Br<sup>-</sup> or I<sup>-</sup>) has been recognized for applications in light emitting diodes, solar cells, photodetectors and hydrogen production. Other than their wide applications, they are less costly, constitute optical properties that are tunable and show high light absorption [250]. They have band gap ranging from 1.51 to 1.55 eV and show absorption at 820 nm wavelength [237]. However, these materials have intrinsic environmental instability issues [251] due to their dispersion in slurry systems containing water as well as disadvantage of deactivating speedily in the liquid solution [252]. Furthermore, organic lead halides like CH<sub>3</sub>NH<sub>3</sub>PbI<sub>3</sub> are photocatalysts for water splitting but at the same time has toxicity due to presence of lead. Therefore, resolving stability issues can make halide perovskite an ideal candidate for photo-catalysis. Moreover, resolving toxicity of lead halide

perovskites can be useful for efficient photocatalytic H<sub>2</sub> production. Hybrid organic-inorganic lead halides show problem of rapid deactivation in liquid solutions, however, this limitation can be resolved using halide perovskite as photosensitizer to directly reduce proton in the liquid solution [249]. In the case of inorganic lead halide CsPbBr<sub>3</sub> nanoparticles with Ru@TiO<sub>2</sub>, electrons were transferred unidirectional from conduction band of CsPbBr<sub>3</sub> nanoparticles to conduction band of n-type TiO<sub>2</sub>, leading to charge separation as shown in Fig. 12 (c). Wu et al. [253], reported that organic lead halide MAPbI<sub>3</sub> ie., CH<sub>3</sub>NH<sub>3</sub>PbI<sub>3</sub>/rGo composite has higher visible light H<sub>2</sub> evolution of 960 μmol g<sup>-1</sup> h<sup>-1</sup> as well as it showed good stability in saturated aqueous HI solution by charge transfer process to rGo as illustrated by Fig. 12 (d). Organic lead perovskite MAPbBr<sub>3</sub> was stabilized using HBr aqueous solution for visible light photocatalytic H<sub>2</sub> generation. Moreover, MAPbBr<sub>3</sub> with Pt/Ta<sub>2</sub>O<sub>5</sub> improved the charge carrier migration for enhanced photocatalysis [254]. Likewise, MAPbI<sub>3</sub> offers optoelectronic properties, however, on exposure of MAPbI<sub>3</sub> with water via hydrogen bonding converts it into (CH<sub>3</sub>NH<sub>3</sub>)<sub>4</sub>PbI<sub>6</sub>(2H<sub>2</sub>O) dehydrate or (CH<sub>3</sub>NH<sub>3</sub>)PbI<sub>3</sub>(H<sub>2</sub>O) monohydrate as hydrated products. Also, it has possibility to be decomposed into MA cation, precipitate of PbI<sub>2</sub> and iodide anion. 31 μmol g<sup>-1</sup> h<sup>-1</sup> H<sub>2</sub> by MAPbI<sub>3</sub> from HI aqueous solution as stabilizer was reported with transition in phase to hydrated phases or PbI<sub>2</sub> for effective visible light splitting of HI to I<sup>3-</sup> and H<sub>2</sub> [255]. In another study, MAPbI<sub>3</sub> with TiO<sub>2</sub>/Pt in HI aqueous solution was investigated for photocatalytic H<sub>2</sub> production along with effective transfer of photogenerated electrons. Moreover, vigorous contact was established between MAPbI<sub>3</sub> and TiO<sub>2</sub>/Pt in HI aqueous solution due to dissolution and re-precipitation of MAPbI<sub>3</sub> as shown in Fig. 12 (e). MAPbI<sub>3</sub> and TiO<sub>2</sub>/Pt forms a heterojunction in which TiO<sub>2</sub>/Pt acted as a support for effective photoactivity [256].

#### 3.4.2. Lead-free halide perovskites

Despite of the excellent properties of lead based organic-inorganic perovskites for photocatalytic application, they are known to be detrimental to environment due to the presence of lead. The toxicity and bioavailability of lead also creates major concern in commercial use of lead-based perovskites. Hence, lead-free halide perovskites are under consideration for having outstanding attributes of essential and useful implications. To generate lead-free halide perovskite, homovalent substitution can be carried out by isovalent cations (Sn, Ge), transitions metals (Fe, Mn, Pd, Ni, Cd, Cu), alkaline-earth metals (Mg, Ca, Sr, Ba), and lanthanides (Yb, Tm, Eu). Moreover, for heterovalent substitution involving lanthanides (La, Lu, Dy, Ce, Pr, Tm, Nd, Sm, Er, Eu, Gd), transition metals (Au), main group elements (Tl, Bi, Sb, Te, Bi) and actinides (Bk, Pu, Am) can be utilized. Based on the wide band gap, instability and toxicity, replacement of lead by Sn (II), Sn (IV), In (III), Sb (III), Bi (III), Ag (I) and Cu (II), Ge (II), Mg (II), Ni(II), Co(II), Zn (II) and V (II) has been only been studied as appropriate elements to generate lead-free halide perovskites [257–260]. Lead-free halide perovskites possess remarkable properties including optoelectronic properties and long-life time of charge carriers valuable for photonic application. Moreover, Bi containing halide perovskites are known to show good optoelectronic properties and are stable in ambient air. Also, Sn based halide perovskites show effective charge movement [261]. However, the issue of instability in air of some B site elements (Ge, Sn) in lead-free halide perovskite, which causes oxidation into tetravalent states of elements can be overcome by mixing B site elements such as Bi and Sb [262]. Utilization of lead-free halide perovskites for photocatalytic H<sub>2</sub> production is rapidly emerging and most notable study is based on their utilization in photocatalytic water splitting devices with 12.3% efficiency. Still, there is lack of studies focusing on photocatalytic H<sub>2</sub> production instead, lead-free halide perovskites are studied largely for use in photovoltaic devices [263].

For instance, bismuth is not a toxic heavy metal, so hybrid metal-organic halide perovskites containing bismuth (Bi<sup>3+</sup>) are capable for photocatalytic activities [264]. Zhao et al. [265], reported that lead free

hybrid when decorated with platinum showed improved charge separation and increased hydrogen evolution. Fig. 12 (f) shows enhanced hydrogen production by [(CH<sub>3</sub>)<sub>2</sub>NH<sub>2</sub>]<sub>3</sub>[BiI<sub>6</sub>] which showed strong optical absorption due to dominant [BiI<sub>6</sub>]<sup>3-</sup> inorganic framework. Likewise, pristine (CH<sub>3</sub>NH<sub>3</sub>)<sub>3</sub>Bi<sub>2</sub>I<sub>9</sub> showed visible photocatalytic H<sub>2</sub> production of 12.91 μmol g<sup>-1</sup> h<sup>-1</sup>, while Pt cocatalyst incorporated (CH<sub>3</sub>NH<sub>3</sub>)<sub>3</sub>Bi<sub>2</sub>I<sub>9</sub> showed 14 folds higher H<sub>2</sub> production as compared to pristine (CH<sub>3</sub>NH<sub>3</sub>)<sub>3</sub>Bi<sub>2</sub>I<sub>9</sub> i.e., 169.21 μmol g<sup>-1</sup> h<sup>-1</sup>. It also showed stability up to 70 h from hydriodic acid [266]. MA<sub>2</sub>CuCl<sub>2</sub>Br<sub>2</sub> was studied as an effective lead-free copper-based perovskite for photocatalytic H<sub>2</sub> production. Copper is an earth abundant metal belonging to first-row transition metals. It overcomes the toxicity of lead and is known to be better than Cl<sup>-</sup> in terms of photochemical properties and instability caused by water [241].

Halide perovskite have distinct advantages, such as structural simplicity, flexibility, and excellent absorption due to X sites but could not be utilized for photocatalytic reactions because of their strong reactivity with water and decomposition by protic solvents due to their strong ionic nature. The dynamic family of halide perovskite can deliver efficient photocatalysis by utilizing emerging idea of dynamic equilibrium for stabilizing halide perovskite. Furthermore, the interface loss, carrier diffusion and charge separation can be future improved for photocatalytic applications.

## 4. Perovskite composite

Currently, in photocatalysis for hydrogen production, nanostructured composite with appropriate band structure and visible light activity are highly demanding [267]. Tuning and controlling properties of semiconductor and biomolecular systems as well as introduction of functionalities is possible by manipulating the composite nanostructures precisely [268]. Furthermore, photocatalysis by composites show improved activity due to increase surface area and reactive sites. A number of titanates including SrTiO<sub>3</sub>, BaTiO<sub>3</sub>, FeTiO<sub>3</sub> and NiTiO<sub>3</sub> have great significance and their properties can be tuned by heterojunction composite formation [269–272]. Composites of perovskite with TiO<sub>2</sub>, g-C<sub>3</sub>N<sub>4</sub> and rGO are studied to form heterojunction for boosting efficient electron transfer. Hydrogen production can be improved by forming heterojunction between perovskite and other materials as it improves charge separation and redox reaction. Heterojunction is formed by the combination of a semiconductor photocatalyst at higher conduction band and other semiconductor at lower conduction band. When irradiated with light, the electrons in semiconductor with higher CB are transferred to semiconductor at lower CB, leaving the holes behind, thus facilitating separation of charge carriers [103].

### 4.1. Titanium based composites

Over past 40 years, TiO<sub>2</sub> is the only prominent photocatalyst utilized for photocatalytic applications [273]. In current years, TiO<sub>2</sub> has also been a significant part of reported cocatalyst systems including SiC, WO<sub>3</sub>, CuO<sub>x</sub>, Cu(OH)<sub>2</sub>, NiO, Ni(OH)<sub>2</sub>, CdS, and Si etc [274–282]. Easy fabrication by in-situ reaction, insignificant mismatch of lattice near the interface and increased chemical stability makes TiO<sub>2</sub>/titanate heterojunction more advantageous as compared with other cocatalyst systems [283–285]. Also, TiO<sub>2</sub> is considered largely for commercial scale hydrogen generation. This is because of its unique photochemical properties, chemical stability, high oxidation power to mineralize a lot of organic molecules, its abundance and nontoxicity [286,287]. Moreover, due to the high chemical stability, TiO<sub>2</sub> is known as an effective photocatalyst in splitting of H<sub>2</sub>O for evolution of H<sub>2</sub> and O<sub>2</sub>. However, zero-dimensional nanostructured TiO<sub>2</sub> show low photocatalytic efficiency [288]. This is due to the low ability of TiO<sub>2</sub> to harvest UV-light due to wide band gap (~3.2 eV), easy charge recombination and the deficiency of active sites on surface, which leads to low quantum efficiency [289,290].

Enhanced photocatalytic efficiency of  $\text{TiO}_2$  composites with perovskites have been demonstrated in various reports. The nanocomposites improved the absorption of solar radiation as well as allowed scavenging of charges [291]. For instance, Fig. 13 (a, b) illustrates that  $\text{TiO}_2$  and  $\text{NiTiO}_3$  are n-type semiconductors, with conduction band edges near to water reduction potential. Moreover, charge separation was accomplished during movement of electrons from  $\text{TiO}_2$  to  $\text{NiTiO}_3$  in their n-n interface and by accumulated electrons in space charge region [289].

Srontium titanate ( $\text{SrTiO}_3$ ) is known as active photocatalyst for water splitting and is a multi-metal oxide with cubic perovskite structure having a band gap of 3.2 eV. The conduction band of  $\text{SrTiO}_3$  is more negative than  $\text{TiO}_2$ . Suppressing recombination of electron hole pairs was investigated by coupling  $\text{SrTiO}_3$  with  $\text{TiO}_2$ . Un-doped intrinsic n-type  $\text{TiO}_2$  has a fermi level which lies at the minimum of its CB range. Thus, the negative shift in Fermi level to more negative redox potential compared to  $\text{H}^+/\text{H}_2$  (0 V vs NHE) increased the hydrogen production due to less hydroxide ions produced as compared to pristine  $\text{TiO}_2$  and  $\text{SrTiO}_3$ . Two semiconductors of unequal band gaps, formed an exceptional heterojunction at the p-n junction i.e., interface where the p-type acceptor perovskite compound ( $\text{SrTiO}_3$ ) and n-type  $\text{TiO}_2$  connect electronically, which acted as trap for the photogenerated electrons and facilitated interfacial electron transfer. In the case of heterojunction, the electrons flowed through p-n junction to the conduction band of  $\text{TiO}_2$ . Improved photocatalytic water splitting was due to spatial interparticle charge separation favored by the flow of charges through the p-n junction and the highly stable reduced states of  $\text{TiO}_2/\text{SrTiO}_3$ , which were even stable under oxygen saturated conditions [283].

Moreover, the formation of composite  $\text{SrTiO}_2/\text{TiO}_2$  and its doping with nickel introduced a new acceptor impurity energy level above the valence band. This reduced band gap shifted the light absorption into visible light region. Electron hole recombination was reduced by  $\text{Ni}^{3+}$  doping as it trapped the photogenerated electrons, transferred the excited electrons to the adsorbed water and induced oxygen vacancies. Fig. 13 (c) depicts electron transfer mechanism in heterojunction of  $\text{SrTiO}_2/\text{TiO}_2$  and role of nickel in reducing electron hole recombination [292].

Similarly, it is demonstrated that the heterojunction of  $\text{TiO}_2$ /porous

$\text{BiFeO}_3$  (P-BFO) showed ability for water reduction. Porous  $\text{BiFeO}_3$  showed negligible  $\text{H}_2$  generation from the water methanol mixture even with Pt cocatalyst. However, the activity is obvious after coupling with nanocrystalline  $\text{TiO}_2$ . When T/P-BFO nanocomposite in proper mole ratio i.e., 9%  $\text{TiO}_2$  was irradiated under visible light, the photogenerated high energy electrons transferred thermodynamically to  $\text{TiO}_2$  conduction band. In this way separation of photogenerated charges was improved (Fig. 13 (d)). When heterojunction is formed between  $\text{TiO}_2$  and BFO, their Fermi energy levels descended and electric field was formed at the interface of the nanocomposite heterojunction. Due to interface electric field, a negative charge appeared on junction face of  $\text{BiFeO}_3$ , while positive charge appeared on face junction of  $\text{TiO}_2$  at equilibrium position. Thus, the charge carrier recombination was significantly reduced, leading to the enhanced photocatalytic activity [293].

Table 7 summarizes the detailed photocatalytic reaction parameters and hydrogen evolution rates on recent research of perovskite composites with  $\text{TiO}_2$  as heterojunction for improved photocatalytic activity. On the whole, the formation of heterojunctions between perovskite and  $\text{TiO}_2$  can reduce the problems of wide band gap and charge recombination. Moreover, red shift in light absorption spectrum and alteration of charge transfer can be noticed as the composite of  $\text{TiO}_2$  with perovskite can tune electronic structures.

#### 4.2. Carbon based perovskite composites

Since many decades, 1 D and 2D carbon-based nanomaterials are known as a noteworthy class of materials widely utilized for clean energy production including hydrogen from solar energy. Carbon is abundantly available on earth and since last two eras carbon-based compounds including graphitic carbon nitride ( $\text{g-C}_3\text{N}_4$ ), graphene (GO), reduced graphene (rGO) and carbon nanotubes have been explored for their application as supercapacitors, biosensors, fuel cells and energy storage [24,37]. Furthermore, they have been utilized for catalysis process. Generally, 1D and 2D carbon-based materials offer outstanding optical and electrical properties, are non-toxic, environmental friendly and are abundant [20,297]. Currently, the utilization of

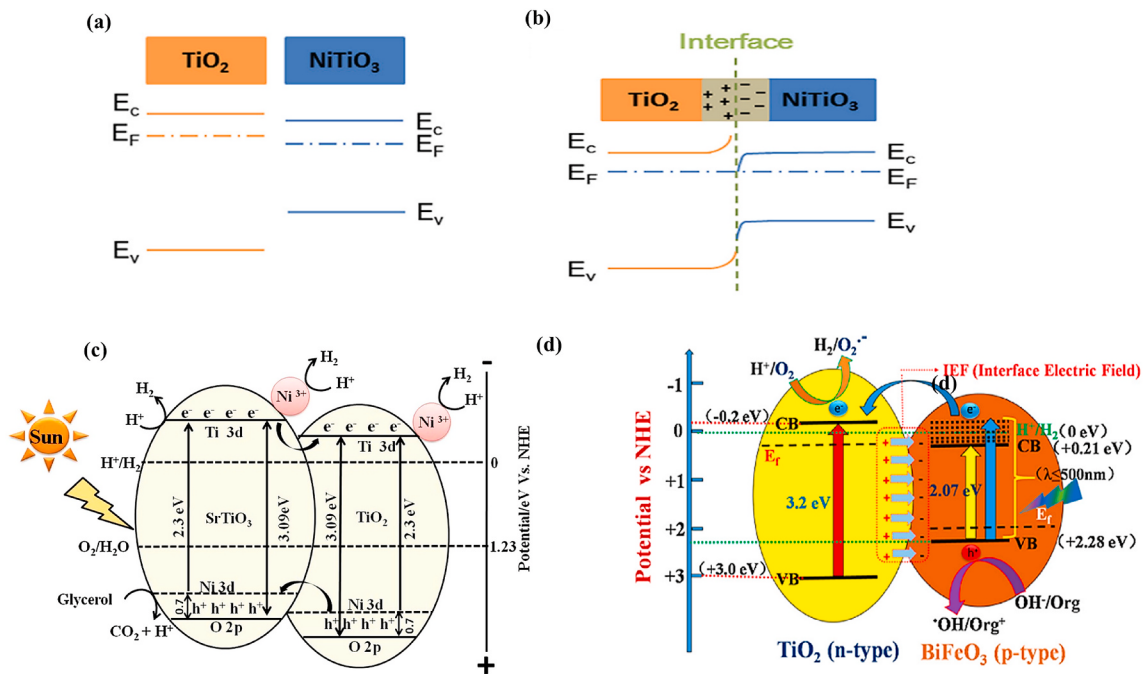


**Fig. 13.** (a, b)  $\text{TiO}_2$ - $\text{NiTiO}_3$  p-n junction [289]; (c) The proposed mechanism for electron transfer and  $\text{H}_2$  evolution on  $\text{TiO}_2/\text{SrTiO}_3$  with Ni as co-catalyst [292]; (d) Schematic diagram showing the energy band gaps of P-BFO and  $\text{TiO}_2$  and the possible transfer mechanism of visible-light excited high energy electrons from BFO to  $\text{TiO}_2$  [293].

**Table 7**Hydrogen production and photocatalytic reaction conditions for TiO<sub>2</sub>/perovskite composites.

Year	Composite	Band gap	Light intensity	Co-catalyst, Loading of catalyst, Reactor	Reagent	H <sub>2</sub> production	Comments	Ref.
2019	LaFeO <sub>3</sub> /TiO <sub>2</sub>	–	300 W Xe lamp (320–780 nm) with power of 195 mW/cm <sup>2</sup>	0.1 g, Quartz reactor cell	80 mL methanol solution (20%)	270 μmolg <sup>-1</sup> h <sup>-1</sup>	Z-scheme promoted efficient charge transfer	[294]
2018	NiTiO <sub>3</sub> /TiO <sub>2</sub>	–	250 W Xenon lamp ( $\lambda = 300\text{--}800\text{ nm}$ )	0.005 g, 135 mL borosilicate reactor	50 mL glycerol-water	87 μmolg <sup>-1</sup> h <sup>-1</sup>	The enhanced photocatalytic activity was due to the formation of a n-n heterojunction between TiO <sub>2</sub> and NiTiO <sub>3</sub> and presence of TiO <sub>2</sub> anatase phase Ni/Ti at 1.77% gave highest H <sub>2</sub>	[295]
2017	Nanotubes-NiTiO <sub>3</sub> /TiO <sub>2</sub>	3.0 eV	Xe lamp (300 W)	0.1 g, Quartz reactor cell (V = 50 mL)	10% methanol in 100 mL distilled water	680 μmolg <sup>-1</sup> h <sup>-1</sup>	Ni/Ti at 1.77% gave highest H <sub>2</sub>	[289]
2017	mesoporous SrTiO <sub>3</sub> /TiO <sub>2</sub>	3.22 eV	Natural solar light ( $\lambda = 200\text{--}800\text{ nm}$ )	Ni 0.5 wt% 0.005 g, Air tight quartz reactor	5% glycerol in water	3750 μmolg <sup>-1</sup> h <sup>-1</sup>	The sample NSTO washed with acid gave more H <sub>2</sub> than without, due to impurities removal	[292]
2016	nanocomposites BiFeO <sub>3</sub> /TiO <sub>2</sub>	2.7 eV	300 W xenon lamp ( $\lambda \leq 420\text{ nm}$ cutoff filter)	Pt 1 wt%, 0.1 g, Pyrex glass cylinder reactor	20 mL methanol + 80 mL water	24 μmol g <sup>-1</sup> h <sup>-1</sup>	The nanocomposites with 9% of TiO <sub>2</sub> gave highest H <sub>2</sub>	[293]
2010	Thin film-Hetro-TiO <sub>2</sub> /SrTiO <sub>3</sub>	3.75 eV	Low pressure UVP Pen ray mercury lamp with power of 5400 μW cm <sup>-2</sup> ( $\lambda = 254\text{ nm}$ )	2-3 films, 45 mL quartz reactor	40 mL water with 5 mL methanol	386.6 μmolg <sup>-1</sup> h <sup>-1</sup>	The SrTiO <sub>3</sub> nanocubes were grown from TiO <sub>2</sub> nanowires by in situ dissolution-precipitation. Hetro, anatase phase were prepared by autoclave Hetro phase gave highest H <sub>2</sub>	[283]
2009	Spherical-N-SrTiO <sub>3</sub> /TiO <sub>2</sub>	3. eV	250 xenon lamp ( $\lambda = 200\text{--}700\text{ nm}$ )	Pt 2 wt%, 0.6 g, Tube shape reactor	600 mL solution of oxalic acid (0.05 mol L <sup>-1</sup> )	5100 μmol g <sup>-1</sup> h <sup>-1</sup>	Highest H <sub>2</sub> was on 400°C calcination temperature	[296]

carbon based compounds in composite with perovskites for photocatalysis is considerably explored as they are capable of enhancing the reaction for H<sub>2</sub> production by increasing active sites for sacrificial agent, by acting as electron acceptor and by acting as a mediator for charge carriers leading to separation of electron hole pairs [29,298]. Moreover, they are known to decrease agglomeration of particles through improving dispersion by acting as host matrix with semiconductor photocatalyst [299]. Heterojunctions of perovskites with carbon based compounds including rGO, GO and g-C<sub>3</sub>N<sub>4</sub> has been widely studied for improvement of photocatalytic H<sub>2</sub> production [300] and has been systematically discussed in next sections.

#### 4.2.1. Graphene and reduced graphene composite

Chemical modification by oxidation and exfoliation of graphene (allotrope of C) accompanied by extensive modification of the basal plane forms GO. GO is a monolayer with high oxygen content, characterized by C/O ratio less than 3:1 and typically closer to 2:1 [301]. Honeycomb structure of graphene induces many extraordinary properties. Graphene has large surface area (2620 m<sup>2</sup>/g), high transparency, excellent charge mobility [302,303], exciting electronic and photonic properties for various applications such as energy storage, photovoltaics, photoelectrochemical and photocatalysis [303,304]. The two-dimension cycle planer structure of graphene enables it to act as an exceptional catalyst carrier [305]. In addition, the transfer of electrons from the conduction band of semiconductor to graphene is also favored by the intimate interfacial contact between photocatalyst and graphene [306]. Currently, graphene is considered and recognized as more portable and flexible for energy applications aimed at future energy needs [307].

The combination of perovskite photocatalysts with graphene has been depicted as an efficient way for suppressing recombination by separating electron hole pairs [308] and enhancing photocatalytic activity [309]. In composites with graphene, an increased number of electrons and holes are involved in the photocatalytic reaction as graphene acts as an electron acceptor and capture electrons readily [310]. Fig. 14 (a) illustrates that the oxidation/exfoliation of graphite gives

bulk solid graphene oxide (GO) and its reduction through various chemical, thermal or electrochemical processes increase the interlayer spaces and functionalize the basal planes, giving reduced graphene (rGO) [311]. It has also been recognized as a solid-state mediator for enhanced charge separation. Moreover, loading rGO on the semiconductors acts as a cocatalyst to catalyze reactions for hydrogen evolution [312].

Reduced graphene oxide (rGO) is a 2D non-metallic carbon material with conductive properties. It is ideal for photocatalysis due to its large surface area, light transmittance, chemical stability and outstanding electron capture and transport [313]. However, the properties relating to conductivity of rGO are not exploited completely. The advantages of doping rGO with semiconductors are: (i) it assists improvement in the separation of the photogenerated charges; (ii) enhances utilization of charges in photocatalytic process; (iii) maintain the structural integrity of composite even after repeated use. Moreover, preparation of composites with rGO is also known to be environmental friendly [314].

In rGO based composites, the semiconductor nanoparticles (NPs) are typically distributed on the surface of rGO sheets [315,316]. Strong interaction between rGO and semiconductor nanoparticles in rGO encapsulated nanostructures makes it a remarkable transporter of charge carriers and induces molecular diffusion property. These properties were implied practically in crumpled graphene nano reactors, in which chemical reaction took place in small nano-spaces for improved stability and catalytic activity [317].

LaFeO<sub>3</sub> (LFO) is an AB<sub>3</sub> type perovskite, exhibiting water splitting properties, but wide band gap and poor lifetime of photogenerated charge carriers limit its use as a photocatalyst. LFO nanospheres were prepared by sol-gel combustion method. Further, LFO spheres were fabricated on 1 wt% rGO surface through ultrasonication. Reduced graphene oxide acted as a cocatalyst under visible light to improve photocatalysis as compared to LFO without rGO. During excitation, the electrons jumped from the valence band of LFO to the conduction band, leaving holes in the valence band. After that, the photogenerated electrons from CB of LFO were transferred to graphene sheets where they participated in H<sub>2</sub> evolution reaction. This was possible because of the

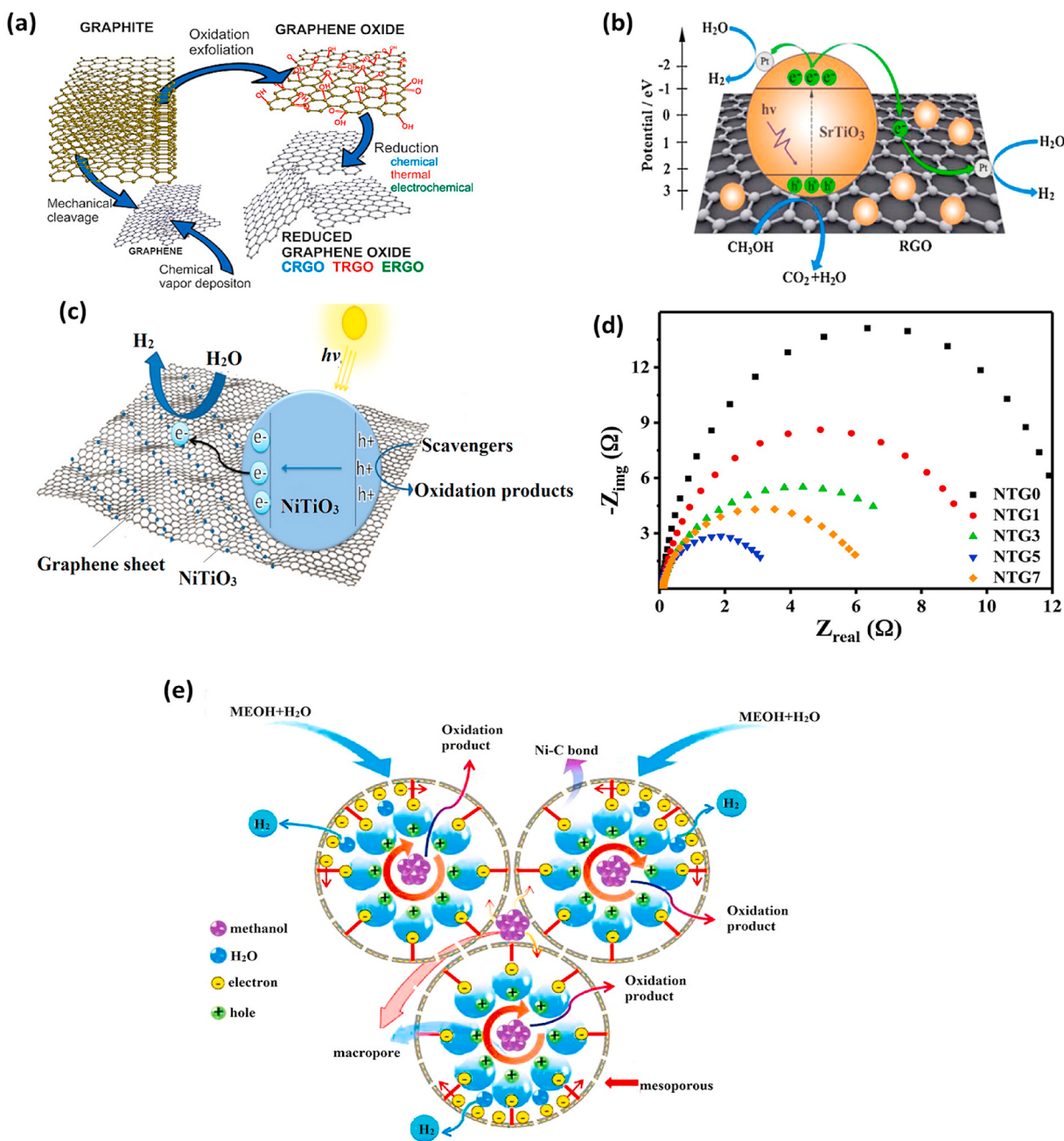


**Fig. 14.** (a) A schematic illustration for preparation of graphene and rGO [311]; (b) Schematic illustration of the photo generated charge transfer and photocatalytic hydrogen production mechanism over  $\text{SrTiO}_3$ -rGO [319]; (c) Schematic illustration for the charge transfer and separation in the  $\text{NiTiO}_3$ /graphene composite under visible light irradiation [320]; (d) Electrochemical impedance spectra of various samples [320]; (e) Photocatalytic hydrogen production mechanism of LNO-rGO nanoreactor [322].

superior interfacial interaction between rGO sheet and LFO nanosphere through the self-assembly tactic and exclusive ability of the rGO [318].

$\text{SrTiO}_3$ -rGO composite exhibited higher photocatalytic activity in methanol solution than pristine  $\text{SrTiO}_3$ . The simple one pot hydrothermal technique was used to synthesize  $\text{SrTiO}_3$ -rGO composite. Composite with uniform morphology was prepared via facile one pot hydrothermal method by 0.8% rGO and showed improved activity. Fig. 14 (b) shows that under UV irradiation, the electrons in VB of  $\text{SrTiO}_3$  were excited to the CB, generating holes in the VB. The rGO sheets and Pt nanoparticles in the  $\text{SrTiO}_3$ -rGO composite acted as electron acceptors. On the other hand, the rGO not only acted as a charge acceptor but also served as a scaffold to improve dispersion of  $\text{SrTiO}_3$  [319].

The  $\text{NiTiO}_3$ /5 wt% Go (NTG) composite has been observed for

improved activity as it showed larger surface area than pristine  $\text{NiTiO}_3$  (NTG). On increasing graphene content, visible light absorbance of composite was enhanced. Increased surface area resulted in improvement towards adsorption-desorption of reactants and products in photocatalytic reaction. Fig. 14 (c) shows that excited electrons migrated from the valence band of  $\text{NiTiO}_3$  (NTG) to the conduction band of  $\text{NiTiO}_3$  and then moved to graphene sheet. This mechanism prevented recombination of electrons and holes and indicated extended lifetime of charge carriers in NTG, which enhanced photocatalytic activity. Fermi level of graphene i.e.,  $-0.08$  V was slightly lower than the conduction band potential of  $\text{NiTiO}_3$  i.e.,  $-0.53$  V, which facilitated the transfer of photoexcited electrons. This shows that graphene acted as an outstanding conductor as well as electron acceptor. Fig. 14 (d) indicates

$\text{NiTiO}_3$  containing different wt. % of graphene and reduced size of semicircles indicates less resistance in charge transfer, allowing rapid separation of photogenerated electrons and holes. Increased charge carrier transfer rate between the photocatalyst and solution depends on the  $\text{sp}^2\pi$ -conjugated domains [320]. Similarly,  $\text{Bi}_2\text{WO}_6$ /graphene composites with doped Ag also showed enhanced photocatalysis due to improved light absorption, decreased band gap of the composite and separation of photogenerated electron hole pairs. The composite of  $\text{KNbO}_3$ /rGO integrated with cocatalyst was an efficient way to improve the charge mobility and separation efficiency of electron and hole pairs [224,321].

Facile self-assembly photocatalytic reduction method was implied to synthesize reduced graphene oxide (rGO) encapsulated  $\text{LaNiO}_3$  (LNO-rGO) composites. Fig. 14 (e) illustrates meso-macroporous framework of the prepared LNO-5% rGO composite. This restricted the electron hole recombination and the electrons rapidly flowed along Ni-C bond to rGO sheets, helping migration of electrons from the surface of LNO to rGO. Moreover, the meso-macroporous framework of crumpled nano-reactor also promoted capturing of photogenerated holes by diffusion and as well as adsorption of molecules of methanol into nano-reactors. Meanwhile,  $\text{H}_2$  was formed by the reaction of electrons adsorbed  $\text{H}_2\text{O}$  molecules and the products spilled over from the nano-reactor through mesoporous structure. More than this, during the whole long recycling process, the nano-reactor showed exceptional stability. This made it possible for rGO and LNO to develop a strong interaction among them

[322].

Layered perovskite,  $\text{Sr}_2\text{Ta}_2\text{O}_7$  has a wide band gap of 3.0–4 eV due to which it is only active under UV irradiation but  $\text{Sr}_2\text{Ta}_2\text{O}_7$  doping with nitrogen minimized the band gap thus, allowing visible light absorption. The composite of  $\text{Sr}_2\text{Ta}_2\text{O}_{7-x}\text{N}_x$  with GO showed charge carrier transportation as the GO acted as “highway” to transport electrons to the cocatalysts i.e., platinum. The electrons in CB of  $\text{Sr}_2\text{Ta}_2\text{O}_{7-x}\text{N}_x$  were injected into GO sheets. Due to high charge carrier mobility of graphene, the electrons were mobilized on the graphene sheet. The Pt nanoclusters decorated on the graphene surface acted as active sites for hydrogen evolution. The presence of graphene suspended in solution reduced the possible recombination. The highest  $\text{H}_2$  production in graphene composites was achieved using 5% GO/ $\text{Sr}_2\text{Ta}_2\text{O}_{7-x}\text{N}_x$ . Quantum efficiency was 6.45, which was 80% more than using pristine  $\text{Sr}_2\text{Ta}_2\text{O}_7$  [323].

Recent advancements in carbon-based perovskite composites with rGO for improved photocatalytic hydrogen production have been listed in Table 8.  $\text{LiFeO}_3$ /rGO showed highest photocatalytic  $\text{H}_2$  production under visible irradiation. 1 wt% rGO in the composite acted as an electron sink, promoted efficient charge separation. Moreover, it narrowed the composite's band gap as well as enhanced adsorption due to large surface area of rGO. Activity was enhanced because  $\text{H}_2$  evolution reaction occurred on both  $\text{LiFeO}_3$  and rGO sheet. The sol gel method for the preparation of LFO nanospheres and ultrasonication process for fabrication of  $\text{LiFeO}_3$  on rGO sheets also contributed to enhanced activity due to better anchoring of  $\text{LiFeO}_3$  nanoparticles.

**Table 8**  
Hydrogen production and photocatalytic reaction conditions for GO and rGO/perovskite composites.

Year	Composite	Band gap	Light intensity	Co-catalyst, Loading of catalyst, Reactor	Reagent	$\text{H}_2$ production	Comments	Ref.
2019	Macroporous- $\text{LaNiO}_3$ -rGO	–	A 175 W high pressure mercury lamp ( $\lambda > 320$ nm)	0.01 g, Pyrex glass reactor	60 mL deionized water and 20 mL methanol	3220 $\mu\text{molg}^{-1}\text{h}^{-1}$	LaNiO <sub>3</sub> -rGO $\text{H}_2$ production was 12 times higher than the LaNiO <sub>3</sub>	[322]
2018	Mesoporous- $\text{NiTiO}_3$ -rGO	–	100 W linear halogen lamp ( $\lambda > 400$ nm)	0.01 g, cylindrical glass vessel	50 mL of pure water and 5 vol % methanol	8383 $\mu\text{molg}^{-1}\text{h}^{-1}$	5% rGO gave highest results	[320]
2018	Nanoparticles-Ag- $\text{Bi}_2\text{WO}_6$ /GO	2.75eV	300 W high-pressure mercury lamp	0.05 g, quartz cell (100 mL)	Sodium sulfide nanohydrate (0.1 M), sodium sulfite (0.04 M), sodium chloride (3 M)	78,000 $\mu\text{molg}^{-1}\text{h}^{-1}$	Highest $\text{H}_2$ was when GO was 1.5 wt % and Ag was 2 Mm	[224]
2017	Nanosphere- $\text{LaFeO}_3$ -rGO	–	125 W medium pressure Hg visible lamp (420 nm)	0.05 g, Batch reactor	50 mL of 10 vol% of $\text{CH}_3\text{OH}$ solution	611,000 $\mu\text{molg}^{-1}\text{h}^{-1}$	Max activity was at 1 wt% rGO	[318]
2015	Ru complex/ $\text{SrTiO}_3$ :Rh and rGO / $\text{BiVO}_4$	–	500 W Xe lamp ( $390 < \lambda \geq 750$ nm)	0.008 g, 8 mL Pyrex test tube	Water (4 mL) with $\text{H}_2\text{SO}_4$ and 10 vol% methanol	21.25 $\mu\text{molg}^{-1}\text{h}^{-1}$	Complex of Ru was [Ru-dpbpy]	[324]
2015	Ru complex / $\text{SrTiO}_3$ :Rh	–	300 W Xe lamp with ( $\lambda > 420$ nm)	0.05 g, Top irradiation cell with a Pyrex glass window.	120 mL with $\text{H}_2\text{SO}_4$ ,	125 $\mu\text{molg}^{-1}\text{h}^{-1}$	Ru-complex electrocatalyst, [Ru (2,2'-bipyridine) (4,4'-diphosphonate-2,2'-bipyridine) ( $\text{CO}_2$ ) <sub>2</sub> ]	[324]
2015	Nanoscrolls- $\text{K}_4\text{Nb}_6\text{O}_{17}$ -rGO	–	300 W Xe lamp filter to remove light with wavelengths above 400 nm	0.1 g, Outer irradiation type quartz cell	100 mL of aqueous solution containing 20 vol% methanol.	106.8 $\mu\text{molg}^{-1}\text{h}^{-1}$	Intercalation of rGO was done in the process of curling of the potassium niobate nanosheets.	[321]
2014	Microsphere- $\text{K}_4\text{Nb}_6\text{O}_{17}$ -rGO	–	300 W Xe lamp filter to remove light with wavelengths above 400 nm	0.1 g, outer-irradiation type quartz cell	100 mL of aqueous solution containing 20 vol% methanol.	1530 $\mu\text{molg}^{-1}\text{h}^{-1}$	Procedure was simple mixing of rGO with $\text{K}_4\text{Nb}_6\text{O}_{17}$	[325]
2014	Nanoparticles-Go/YInO <sub>3</sub>	–	300 W Xe arc lamp ( $\lambda = 420$ nm and 750 nm)	0.5 wt% Pt, 0.01 g, 330 mL top irradiation reactor	100 mL solution containing 0.0025 mol $\text{Na}_2\text{S}$ and 0.0025 mol $\text{Na}_2\text{SO}_3$ .	400.4 $\mu\text{molg}^{-1}\text{h}^{-1}$	separation and lifetime of electron-hole pairs were accomplished by chemical bonding between YInO <sub>3</sub> and graphene	[326]
2011	$\text{Sr}_2\text{Ta}_2\text{O}_7$ /N/GO	4.2eV	AM1.5, 1000 $\text{W/m}^2$ lamp (400–700 nm)	Pt, 0.5 mg/L of $\text{Sr}_2\text{Ta}_2\text{O}_{7-x}\text{N}_x$ and 0.5 mg/L GO air free closed gas circulation system reaction cell made of quartz. (V = 150 mL)	10 mL methanol	586,000 $\mu\text{molg}^{-1}\text{h}^{-1}$	Best $\text{H}_2$ production was when Pt was 2.5 wt% and GO was 5 wt%	[323]

#### 4.3. Graphitic carbon nitride composite

Graphitic carbon nitride ( $\text{g-C}_3\text{N}_4$ ) is a non-metal polymeric carbon-based semiconductor having layered structure. It has band gap 2.7 eV and shows visible light response up to wavelength 460 nm and is a metal free photocatalyst for hydrogen production [327,328]. Moreover, other than its band gap, other properties which makes  $\text{g-C}_3\text{N}_4$  suitable for water splitting [329,330] are its simple preparation, low cost, pollution free feature and high chemical stability [331]. Under visible light irradiation,  $\text{g-C}_3\text{N}_4$  shows outstanding photocatalytic activity owing to its electron richness and basic surface functionalities [33] as well as stability in water splitting for hydrogen evolution [9,332,333]. At the same time, rapid electron-hole pairs recombination and moderately small surface area are some shortcomings of  $\text{g-C}_3\text{N}_4$  [330,334,335].

Nickel titanate ( $\text{NiTiO}_3$ ) with a band gap of 2.18 eV shows good visible light photocatalytic activity, however, the CB level of  $\text{NiTiO}_3$  is not more negative than hydrogen evolution level ( $E=\text{H}_2/\text{H}_2\text{O}$ ) to initiate hydrogen production, thus it shows no photocatalytic performance. The heterojunction between  $\text{g-C}_3\text{N}_4$  and  $\text{NiTiO}_3$  showed photocatalytic activity under visible light irradiation. The electrons transfer from the CB of  $\text{g-C}_3\text{N}_4$  to the CB of  $\text{NiTiO}_3$  did not occur because of the inner electric field, but the transfer of holes from the VB of  $\text{g-C}_3\text{N}_4$  to the VB of  $\text{NiTiO}_3$  was stimulated. This resulted in longer lifetime of the photo-generated electrons and holes, separation of the photo generated electron hole pairs and enhanced photocatalytic activity [336].

Similarly,  $\text{AgNbO}_3$  is also a perovskite active under visible light due to its moderate band gap (2.8 eV). Unfortunately, the photoactivity is limited by fast charges recombination. Separation of charge carrier was successfully obtained by developing composite of  $\text{AgNbO}_3/\text{g-C}_3\text{N}_4$ ,

resulting in enhanced production of hydrogen under visible light. Improved photocatalytic activity was observed using  $\text{AgNbO}_3/\text{g-C}_3\text{N}_4$  prepared via microwave heating method. Using this method,  $\text{g-C}_3\text{N}_4$  was not decomposed and this approach was also useful in improving crystallinity. Improved electron transfer was obtained due to chemical bonds which were formed at the interface and helped to decrease surface energy. On the basis of matched band position of the two semiconductors, heterojunction was constructed between them. Fig. 15 illustrates that the inner electric field in the heterojunction transferred electrons from  $\text{g-C}_3\text{N}_4$  to the CB of  $\text{AgNbO}_3$ . At the same time, the holes in  $\text{AgNbO}_3$  migrated to the VB of  $\text{g-C}_3\text{N}_4$ . Sacrificial agent i.e., methanol consumed the holes in  $\text{g-C}_3\text{N}_4$ , while accumulated electrons in the CB of  $\text{AgNbO}_3$  were transferred to Pt nanoparticles and  $\text{H}^+$  was reduced to  $\text{H}_2$  [337]. Likewise, Fig. 15 (b and c) illustrates charge transfer and photocatalytic mechanism in heterojunction for  $\text{g-C}_3\text{N}_4$  with  $\text{KCa}_2\text{Nb}_3\text{O}_{10}$  nanosheets and  $\text{KCa}_2\text{Ta}_3\text{O}_{10}$  Dion-Jacobson perovskite, respectively.  $\text{KCa}_2\text{Nb}_3\text{O}_{10}$  and  $\text{KCa}_2\text{Ta}_3\text{O}_{10}$  were not active under visible light but, when heterojunction was formed with  $\text{g-C}_3\text{N}_4$ , the electrons were excited from the VB to the CB of  $\text{g-C}_3\text{N}_4$  nanosheets, leaving electropositive holes in the VB of respective perovskite. This transfer of photogenerated electrons from  $\text{g-C}_3\text{N}_4$  nanosheets to  $\text{KCa}_2\text{Nb}_3\text{O}_{10}$  nanosheets was because of more negative CB edge potential of  $\text{g-C}_3\text{N}_4$  (-1.12 eV) than the CB edge potential of  $\text{KCa}_2\text{Nb}_3\text{O}_{10}$  (-0.784 eV) and  $\text{KCa}_2\text{Nb}_3\text{O}_{10}$  [338]. So, due to more positive VB edge of the  $\text{g-C}_3\text{N}_4$  (1.59 eV) the photogenerated holes were left in the VB of  $\text{g-C}_3\text{N}_4$  and were consumed for water oxidation.

Heterojunction composite  $\text{Ca}_2\text{Nb}_2\text{TaO}_{10}/\text{g-C}_3\text{N}_4$  showed good hydrogen production from aqueous methanol solution under visible light. Hybridization of two-dimensional nanostructured materials ( $\text{Ca}_2\text{Nb}_2\text{TaO}_{10}/\text{g-C}_3\text{N}_4$  bulk) constituted a specific surface area of 7.56

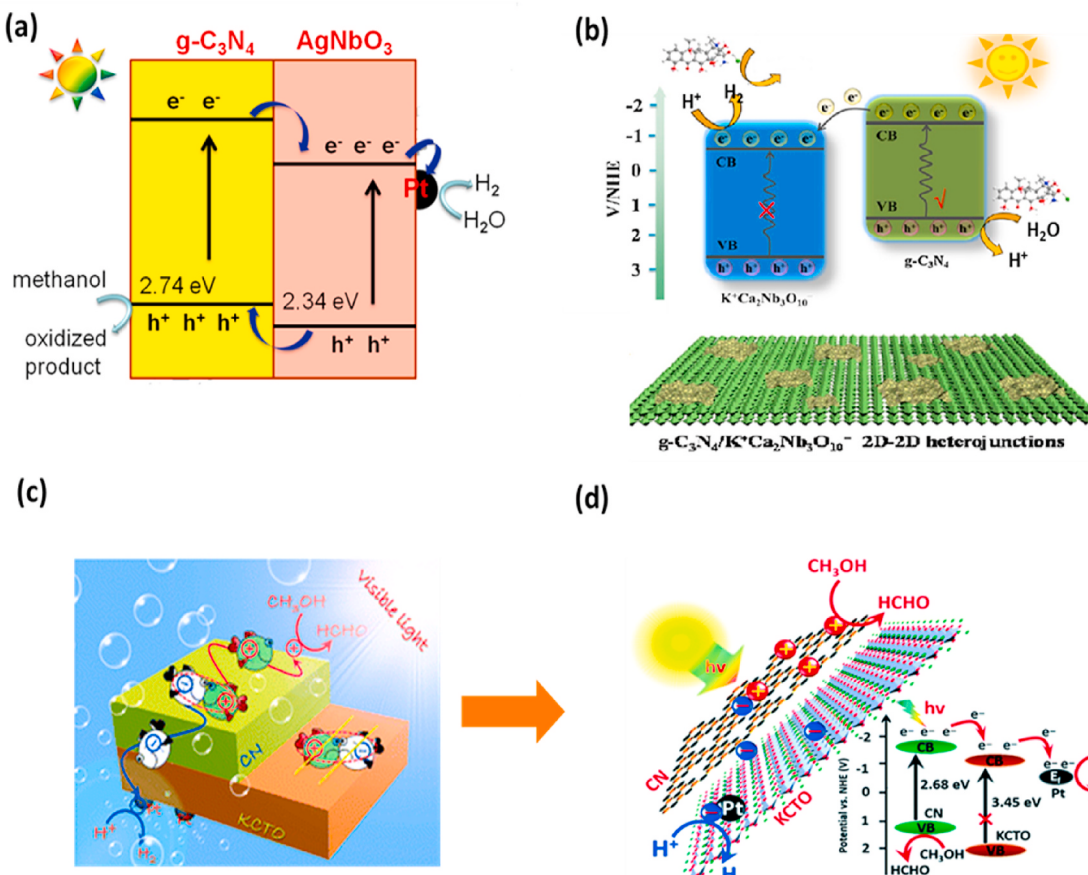


**Fig. 15.** Heterojunction between  $\text{AgNbO}_3$  and  $\text{g-C}_3\text{N}_4$  for efficient electron transfer [337]; Schematic representation of the charge separation and transfer in the  $\text{CN}/\text{K}^+\text{Ca}_2\text{Nb}_3\text{O}_{10}$  nanosheet heterojunction under visible light irradiation [339]; charge transfer and photocatalytic  $\text{H}_2$  production mechanism in  $\text{KCa}_2\text{Ta}_3\text{O}_{10}/\text{g-C}_3\text{N}_4$  [340].

$\text{m}^2/\text{g}$ , while, the  $\text{Ca}_2\text{Nb}_2\text{TaO}_{10}/\text{g-C}_3\text{N}_4$  nanosheets has a specific surface area of  $43.81 \text{ m}^2/\text{g}$ . Transfer of photoinduced charge carriers and suppression of electron hole pairs recombination was accomplished by the heterostructured photocatalyst as depicted in Fig. 16 (a). Fig. 16 (b) indicates UV/Vis diffuse reflection spectra, which indicates that  $\text{g-C}_3\text{N}_4$  is visible light active, but  $\text{Ca}_2\text{Nb}_2\text{TaO}_{10}$  is UV light active photocatalyst. The  $\text{g-C}_3\text{N}_4/\text{Ca}_2\text{Nb}_2\text{TaO}_{10}$  nanosheet composite showed sharper absorption in the visible region. The activity of nanosheets was about 2 times higher than bulk because of the synergic properties of increased surface area and the quantum confinement effect, which increased the ability of redox potential of generated charges on  $\text{g-C}_3\text{N}_4$  based composite [341].

Furthermore, heterojunction of  $\text{g-C}_3\text{N}_4/\text{SrTa}_2\text{O}_6$  showed remarkable activity for hydrogen evolution as shown in Fig. 16 (c). Similarly,  $\text{g-C}_3\text{N}_4/\text{CaTiO}_3$  (Fig. 16 (d)) and  $\text{g-C}_3\text{N}_4/\text{KCa}_2\text{Ta}_3\text{O}_{10}$  heterojunction improved visible light photocatalytic activity because of narrowed band edges and intimate contact between perovskite and  $\text{g-C}_3\text{N}_4$ , which reduced the interface energy and impored electron transfer [342,343].

Pertinent hydrogen evolution by carbon-based perovskite composite with  $\text{g-C}_3\text{N}_4$  through photocatalytic reaction is summarized in Table 9. Dion-Jacobson phase  $\text{Ca}_2\text{Nb}_2\text{TaO}_{10}$  showed highest visible light photocatalytic activity for composite with  $\text{g-C}_3\text{N}_4$  because of the synergistic effect as well as due to intimate interfacial connections between  $\text{g-C}_3\text{N}_4$  nanosheets and  $\text{Ca}_2\text{Nb}_2\text{TaO}_{10}$  nanosheets. The cascading electrons proved to be efficient in suppressing charge recombination and improving photocatalytic  $\text{H}_2$  evolution performance.

#### 4.4. Other perovskite composites

Heterojunction formation of perovskites with noble metal free narrow band gap (2.4 eV)  $\text{CdS}$  is rarely studied, but is known to improve photocatalytic  $\text{H}_2$  production by improvement of visible light activity and interfacial charge transfer. Moreover, the water reduction potential of  $\text{CdS}$  is thermodynamically feasible as  $\text{CdS}$  constitutes a more negative CB than the  $\text{H}_2\text{O}/\text{H}_2$  reduction potential [345]. For instance, visible light photoactivity of layered  $\text{La}_2\text{Ti}_2\text{O}$  with  $\text{CdS}$  and black phosphor quantum dots (QDs) was observed to generate  $960 \mu\text{mol g}^{-1}\text{h}^{-1}$  of  $\text{H}_2$ . The enhanced activiry was obviously due to the appropriate band alignment of  $\text{CdS}$ , strong electron donating ability of  $\text{CdS}$ , electron relay and boosted light absorption [346]. Likewise, heterostucture of  $\text{SrTiO}_2$  with  $\text{CdS}$  has been investigated for enhanced  $\text{H}_2$  production due to efficient charge transfer and separation [347]. In another development,  $\text{CdS}$ ,  $\text{Bi}_2\text{S}_3$  QDs co-decorated  $\text{KNbO}_3$  composite scheme also showed photocatalytic activity in visible range 420–520 nm, respectively [348].  $\text{HSr}_2\text{Nb}_3\text{O}_{10}$  nanosheets coupled  $\text{CdS}$  heterojunction was reported for improved activity because of increased surface area, improved charge separation and light absorptioin [349].

Moreover, up conversion effect of doped luminescent agents is also been studied for improvement of photoctalytic activity. For instace, improved visible light absorptioin and boosted  $\text{H}_2$  generation was investigated for  $\text{Er}^{3+}:\text{Y}_3\text{Al}_5\text{O}_{12}/\text{KNbO}_3$  [133] and dual substituted  $\text{Eu}^{3+}$  in bulk  $\text{NaTiO}_3$  [350]. Doping of erbium ( $\text{Er}^{3+}$ ) in  $\text{SrTiO}_3$  was also studied for improved visible light absorptioin. This was due to  $\text{Er}^{3+}$  intraband transition absorption and elevated energy excited state of  $\text{Er}^{3+}$ . It also conserved energy to carry out redox reactions and improved charge

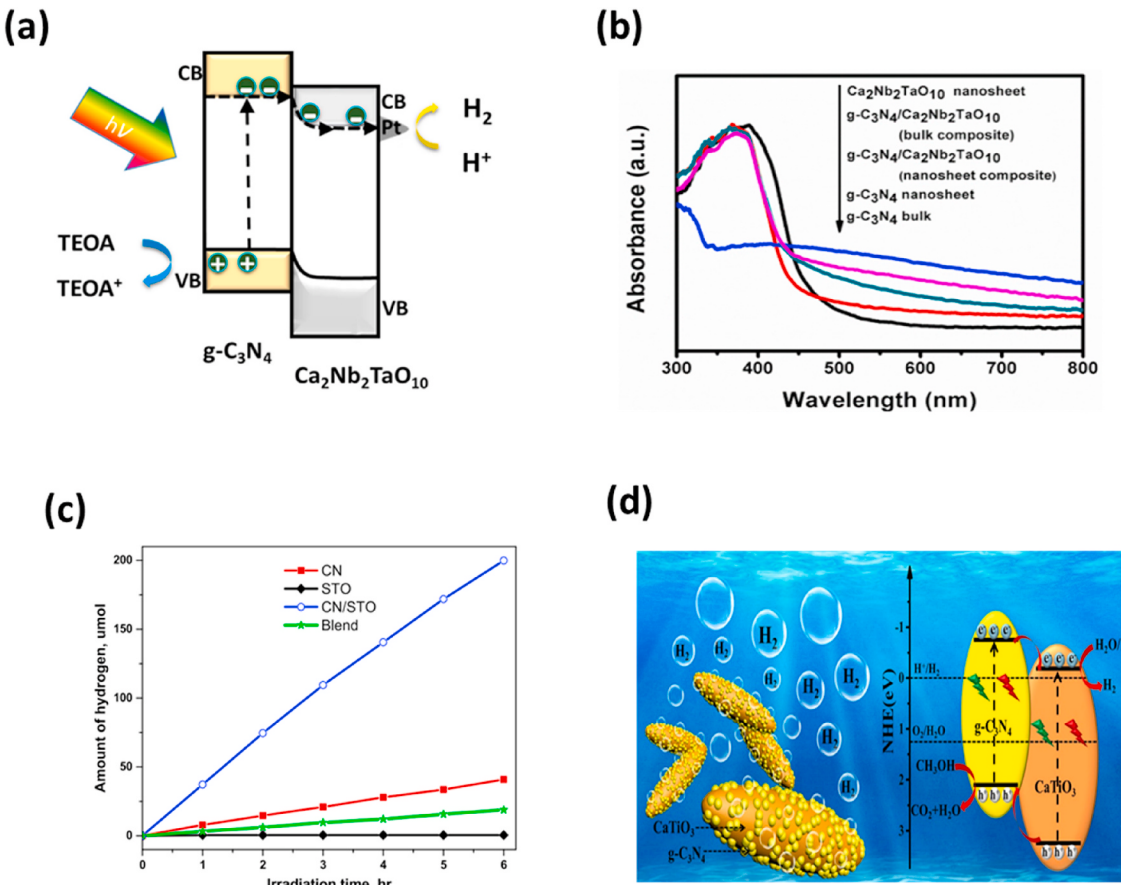


Fig. 16. (a) Schematic diagram of the charge separation; (b) UV-vis diffuse reflection spectra of the samples; Blue:  $\text{Ca}_2\text{Nb}_2\text{TaO}_{10}$  nanosheets, Pink:  $\text{g-C}_3\text{N}_4/\text{Ca}_2\text{Nb}_2\text{TaO}_{10}$  bulk composite, Aqua:  $\text{g-C}_3\text{N}_4/\text{Ca}_2\text{Nb}_2\text{TaO}_{10}$  nanosheet composite, Red:  $\text{g-C}_3\text{N}_4$  nanosheets, Black:  $\text{g-C}_3\text{N}_4$  bulk [341]; (c) The rate of hydrogen generation from photocatalytic water reduction under visible light irradiation [343]; (d) The photocatalytic hydrogen production mechanism of the  $\text{g-C}_3\text{N}_4/\text{CaTiO}_3$  nano-heterojunction [342]. (For interpretation of the references to colour in this figure legend, the reader is referred to the Web version of this article.)

**Table 9**Hydrogen production and photocatalytic reaction conditions for g-C<sub>3</sub>N<sub>4</sub>/perovskite composites.

Year	Catalyst	Band gap	Light intensity	Co-catalyst, Loading of catalyst, Reactor	Reagent	Product H <sub>2</sub>	comments	Ref.
2019	Nanocubes-AgNbO <sub>3</sub> /g-C <sub>3</sub> N <sub>4</sub>	2.35 eV	300 W Xe-lamp UV cut-off filter ( $\lambda > 420$ nm)	Pt 0.37 wt%, 0.1 g, Top irradiation reactor	CH <sub>3</sub> OH solution (100 mL, 20 vol %)	88.0 $\mu\text{mol}$ $\text{g}^{-1}\text{h}^{-1}$	1% ANCN sample exhibited the best photoactivity. H <sub>2</sub> was more by microwave method from melamine as compared to conventional method	[337]
2018	Nanosheets-KCa <sub>2</sub> Ta <sub>3</sub> O <sub>10</sub> /g-C <sub>3</sub> N <sub>4</sub>	3.44 eV	300 Xe lamp of 128 mW/cm <sup>-2</sup> power. (420 nm cut-off filter)	Pt 1 wt%, 0.05 g	50 mL of aq. sol containing 20 vol % methanol	647.19 $\mu\text{mol}\text{g}^{-1}\text{h}^{-1}$	30%-CN/KCTO showed the highest H <sub>2</sub> production activity	[344]
2018	g-C <sub>3</sub> N <sub>4</sub> /CaTiO <sub>3</sub>		A 300 W Xe arc lamp of with 100 mW/ cm <sup>-2</sup> power. (simulating sunlight)	0.05 g, Lab solar III system	100 mL solution with 10 mL methanol	189.38 $\mu\text{mol}\text{g}^{-1}\text{h}^{-1}$	g-C <sub>3</sub> N <sub>4</sub> /CaTiO <sub>3</sub> was prepared with different mol ratio. H <sub>2</sub> was highest for g-C <sub>3</sub> N <sub>4</sub> /CaTiO <sub>3</sub> for ratio 2:13.5	[342]
2017	Bi <sub>2</sub> MoO <sub>6</sub> /g-C <sub>3</sub> N <sub>4</sub>	2.7 eV	300 W Xe (UV cutoff filter >420 nm)	Pt 3 wt%. 0.1 g, top- irradiated reaction vessel	100 mL solution with 10% tri ethanolamine	563.4 $\mu\text{mol}\text{g}^{-1}\text{h}^{-1}$	20%-BM/CNNs exhibited the optimal photocatalytic hydrogen evolution. H <sub>2</sub> from 20%-BM/CNN was almost 3.84 and 32.19 times higher than that of bulk g-C <sub>3</sub> N <sub>4</sub> and Bi <sub>2</sub> MoO <sub>6</sub>	[313]
2017	Nanosheets-g-C <sub>3</sub> N <sub>4</sub> / Ca <sub>2</sub> Nb <sub>2</sub> TaO <sub>10</sub>	3.67 eV	300 W Xenon arc lamp (400 nm cut-off filter.)	Pt 1 wt%, 0.05 g, quartz top irradiation reactor	200 mL aq. sol of triethanolamine 10 vol %	870.80 $\mu\text{mol}\text{g}^{-1}\text{h}^{-1}$	Nanosheets were better than bulk for g-C <sub>3</sub> N <sub>4</sub> /Ca <sub>2</sub> Nb <sub>2</sub> TaO <sub>10</sub> in 80:20 ratio	[341]
	g-C <sub>3</sub> N <sub>4</sub> /SrTa <sub>2</sub> O <sub>6</sub>	3.22 eV	300 W Xenon lamp (420 nm cut-off filter)	Pt 2.5 wt%, 0.05 g, Pyrex reactor (V = 80 mL)	50 water with 5% tri ethanolamine	666.6 $\mu\text{mol}\text{g}^{-1}\text{h}^{-1}$	Matching between band positions of CN and STO led to better charge separation	[343]
Rode like-NiTiO <sub>3</sub> /g-C <sub>3</sub> N <sub>4</sub>	2.18 eV	Xe arc lamp (UV- cutoff filter $\lambda = 420$ nm)	Pt 1.0 wt % 0.1 g, top irradiation type Pyrex vessel	100 mL tri- ethanolamine aqueous solution (10 vol %)	835 $\mu\text{mol}\text{g}^{-1}\text{h}^{-1}$	By facile ethylene glycol-mediated route, rod like NaTiO <sub>3</sub> gave much better H <sub>2</sub> than bulk by sol gel method	[336]	

separation [351].

Other perovskite based heterojunctions were also reported for efficient photocatalytic H<sub>2</sub> production under visible light including LaCoO<sub>3</sub>/SnO<sub>2</sub> [352], Ru doped and Fe<sub>2</sub>O<sub>3</sub> coupled LaFeO<sub>3</sub> perovskite [353]. Efficient light absorption, improved charge transfer and reduced charge recombination was observed for PbTiO<sub>3</sub>/LaCrO<sub>3</sub> [354] and LaCoO<sub>3</sub>/SnO<sub>2</sub> p-n heterojunction. Improved photocatalytic activity was also reported for layered Bi<sub>2</sub>WO<sub>3</sub> heterojunction with BiOCl [355] and Bi<sub>2</sub>S<sub>3</sub> QDs co-decorated KNbO<sub>3</sub> composite scheme which showed photocatalytic activity in visible range 420–520 nm [356].

Overall, the heterojunction formation has of CdS with perovskites is an advantageous way of fabricating wide band gap perovskites for improved visible light photoactivity. The narrow gap, charge separation, appropriate band alignment and thermodynamically appropriate reduction potential induces effective photocatalytic H<sub>2</sub> production in perovskites. Also, luminescent agents located in distorted BO<sub>6</sub> to the host perovskite ions with B site octahedra to develop an internal electric field is responsible for the efficient charge transfer for boosted H<sub>2</sub> production.

## 5. Conclusions and future perspective

### 5.1. Conclusions

Photocatalytic hydrogen production by perovskite is considered to be the best-known renewable energy production technique by utilizing light and water to meet the growing energy demand without compromising the future energy demand. Moreover, hydrogen energy by photocatalysis is recognized to be sustainable energy because of its zero environmental impact and can be generated easily by non-replenished sources. Moreover, photocatalysis is also known to be cost effective and environmentally friendly H<sub>2</sub> generating technique. In this perspective, the review presents an overview of perovskites, mechanism for hydrogen production, thermodynamics analysis and different

approaches in improving efficiency of perovskite for sustainable hydrogen production. In general, perovskites are most demanding semiconductors belonging to very important family of materials and exhibit exceptional characteristics in photocatalytic application. Different modification approaches such as doping with non-metals, substituting A or B site of ABO<sub>3</sub> perovskite, formation of solid solution, incorporation of nitrogen into the perovskite lattice as well as formation of composites has been discussed.

- The introduction of metals forming appropriate Schottky barrier and noble metals showing SPR effect into perovskite can lead to increase in activity for hydrogen production. Similarly, non-metal anion doping is more preferred approach for boosting visible light activity of perovskites. Metal doping contributes in narrowing of band gap and reduction of charge carrier recombination.
- The flexible structure of perovskite allows A site substitution, B site substitution, solid solution formation and nitridation of perovskite oxide, which are considered efficient approaches to improve photocatalytic activity. Halide perovskite have reasonable band gap for visible light activation, but show recombination, decomposition and stability issues in photocatalysis applications.
- Composite formation by combining perovskite with other semiconductors i.e., TiO<sub>2</sub> to construct heterojunction promotes charge carrier separation towards boosting H<sub>2</sub> evolution. Moreover, carbon-based perovskite composites of g-C<sub>3</sub>N<sub>4</sub> and rGO are also capable of maximizing efficiency for production under visible light irradiation by heterojunction formation and by formation of Z-scheme systems, respectively.

### 5.2. Future prospective

- Perovskite semiconductors have a great potential in photocatalytic water splitting, but the knowledge of perovskite semiconductors

working under visible light range is still not up-to-date, leading to limited large-scale applications. Further research should be carried out on band gap tuning and band adjustment of perovskites for overcoming future energy needs. Moreover, they have limited practical applications due to issues in stability, cost and charge transfer and separation, redox reaction and efficiency, which remains a challenge. With the aid of appropriate approaches to construct heterojunction composite, proper selection of sacrificial reagents and efficient design of photoreactor can be employed to overcome such problems. In spite of the band gap engineering for efficiency improvement, wide and mismatched band gaps of semiconductor perovskites are still a challenge. In depth investigation is required for overcoming stability and toxicity related issues of halide perovskites. These perovskites can be coupled with green clays such as montmorillonite (MMT) and bentonite (Bt) due to their 2D layered structure, higher sorption capacity and provides efficient charge separation with good stability in multiple cycles. Besides, with the use of MAX phase and MXenes multilayers materials coupled with perovskite, higher light absorption with enhanced photoactivity and stability could be achieved.

- Detailed understanding on photoactivity dependence on morphology and retrieval of photocatalyst is also lacking. Improvement of dynamic conditions for photoactivity for molecular catalyst needs considerable attention as numerous molecular photocatalysts like halide perovskites are inappropriate for utilizing in aqueous medium i.e., water. The immobilization of photocatalyst on solid support such as mesh, monolithic and FTO supports are recognized as effective strategies for overcoming these issues and also help in the recovery and reusability of catalyst. However, the use of water as proton source without the help of sacrificial agent is still a challenge. These can be overcome with controlled environment such as temperature, sacrificial reagent concentration, catalyst loading and interaction between light source and catalyst. The controlled light intensity, gas phase photocatalytic systems and batch/continuous processes are also promising to provide detailed information about the photoactivity and stability to catalysts.
- Moreover, there is need to investigate the effect of photoreactors to improve catalyst activity with higher harvesting of light and improved stability in multiple cycles. Adequate and precise photoreactors are in need for improved photocatalytic process, depending on the requirements and conditions of photocatalytic mechanism. Also, quantum efficiency calculations for photocatalytic H<sub>2</sub> production are rarely studied, thus, attentions should be given to evaluate the flux of light being consumed and amount of hydrogen produced. More importantly, there are limited reports available highlighting the evolution of products other than hydrogen to understand the role of perovskites and their composites on yield rates and selectivity. The detailed information about reaction mechanism, reaction kinetics and thermodynamics analysis can further contribute to maximize catalyst photoactivity and products selectivity under UV and visible light irradiations. This work provides enough guidance for understanding mechanism of photocatalysis by perovskites and future research is recommended to develop an effective perovskite composite integrated with efficient photoreactor system for enhanced efficiency for H<sub>2</sub> evolution.

#### Declaration of competing interest

The authors declared no potential conflicts of interest with respect to the research, authorship, and publication of this article.

The authors received a financial support from Universiti Teknologi Malaysia (Research University Grant, Vot 17H06).

#### Acknowledgement

This work was supported by Universiti Teknologi Malaysia (UTM),

Malaysia under University Research Grant (RUG, Vot Q. J130000.2651.16J58).

#### References

- [1] Yi H, Huang D, Qin L, Zeng G, Lai C, Cheng M, et al. Selective prepared carbon nanomaterials for advanced photocatalytic application in environmental pollutant treatment and hydrogen production. *Appl Catal, B* 2018;239:408–24.
- [2] Tahir B, Tahir M, Amin NAS. Tailoring performance of La-modified TiO<sub>2</sub> nanocatalyst for continuous photocatalytic CO<sub>2</sub> reforming of CH<sub>4</sub> to fuels in the presence of H<sub>2</sub>O. *Energy Convers Manag* 2018;159:284–98.
- [3] Abdalla AM, Hossain S, Nisifordi OB, Azad AT, Dawood M, Azad AK. Hydrogen production, storage, transportation and key challenges with applications: a review. *Energy Convers Manag* 2018;165:602–27.
- [4] Gupta NM. Factors affecting the efficiency of a water splitting photocatalyst: a perspective. *Renew Sustain Energy Rev* 2017;71:585–601.
- [5] Saeed Baamran K, Tahir M. Thermodynamic investigation and experimental analysis on phenol steam reforming towards enhanced H<sub>2</sub> production over structured Ni/ZnTiO<sub>3</sub> nanocatalyst. *Energy Convers Manag* 2019;180:796–810.
- [6] Khan AA, Tahir M. Recent advancements in engineering approach towards design of photo-reactors for selective photocatalytic CO<sub>2</sub> reduction to renewable fuels. *J CO<sub>2</sub> Util* 2019;29:205–39.
- [7] Taheri Najafabadi A, Taghipour F. Physicochemical impact of zeolites as the support for photocatalytic hydrogen production using solar-activated TiO<sub>2</sub>-based nanoparticles. *Energy Convers Manag* 2014;82:106–13.
- [8] Yoong L, Chong FK, Dutta BK. Development of copper-doped TiO<sub>2</sub> photocatalyst for hydrogen production under visible light. *Energy* 2009;34:1652–61.
- [9] Fajrina N, Tahir M. Engineering approach in stimulating photocatalytic H<sub>2</sub> production in a slurry and monolithic photoreactor systems using Ag-bridged Z-scheme pCN/TiO<sub>2</sub> nanocomposite. *Chem Eng J* 2019;374:1076–95.
- [10] Fujishima A, Honda K. Electrochemical photolysis of water at a semiconductor electrode. *Nature* 1972;238:37–8.
- [11] Shi Y, Yang AF, Cao CS, Zhao B. Applications of MOFs: recent advances in photocatalytic hydrogen production from water. *Coord Chem Rev* 2019;390: 50–75.
- [12] Wang H, Zhang L, Chen Z, Hu J, Li S, Wang Z, et al. Semiconductor heterojunction photocatalysts: design, construction, and photocatalytic performances. *Chem Soc Rev* 2014;43:5234–44.
- [13] Abdin Z, Alim MA, Saidur R, Islam MR, Rashmi W, Mekhilef S, et al. Solar energy harvesting with the application of nanotechnology. *Renew Sustain Energy Rev* 2013;26:837–52.
- [14] Acar C, Dincer I. Impact assessment and efficiency evaluation of hydrogen production methods. *Int J Energy Res* 2015;39:1757–68.
- [15] Fajrina N, Tahir M. A critical review in strategies to improve photocatalytic water splitting towards hydrogen production. *Int J Hydrogen Energy* 2019;44:540–77.
- [16] Zhu J, Zach M. Nanostructured materials for photocatalytic hydrogen production. *Curr Opin Colloid Interface Sci* 2009;14:260–9.
- [17] Muradov NZ, Veziroglu TN. “Green” path from fossil-based to hydrogen economy: an overview of carbon-neutral technologies. *Int J Hydrogen Energy* 2008;33: 6804–39.
- [18] Tasleem S, Tahir M, Zakaria ZY. Fabricating structured 2D Ti<sub>3</sub>AlC<sub>2</sub> MAX dispersed TiO<sub>2</sub> heterostructure with Ni<sub>2</sub>P as a cocatalyst for efficient photocatalytic H<sub>2</sub> production. *J Alloys Compd* 2020;155752.
- [19] Tentu RD, Basu S. Photocatalytic water splitting for hydrogen production. *Curr Opin Electrochim* 2017;5:56–62.
- [20] Umer M, Tahir M, Azam MU, Tahir B, Jaffar MM, Alias H. Montmorillonite dispersed single wall carbon nanotubes (SWCNTs)/TiO<sub>2</sub> heterojunction composite for enhanced dynamic photocatalytic H<sub>2</sub> production under visible light. *Appl Clay Sci* 2019;174:1110–9.
- [21] Janáky C, Rajeshwar K, De Tacconi N, Chanmanee W, Huda M. Tungsten-based oxide semiconductors for solar hydrogen generation. *Catal Today* 2013;199: 53–64.
- [22] Attia Y, Samer M. Metal clusters: new era of hydrogen production. *Renew Sustain Energy Rev* 2017;79:878–92.
- [23] Carrasco-Jaim OA, Ahumada-Lazo R, Clark PCJ, Gómez-Solis C, Fairclough SM, Haigh SJ, et al. Photocatalytic hydrogen production by biomimetic indium sulfide using Mimosa pudica leaves as template. *Int J Hydrogen Energy* 2019;44: 2770–83.
- [24] Umer M, Tahir M, Azam MU, Jaffar MM. Metals free MWCNTs@TiO<sub>2</sub>@MMT heterojunction composite with MMT as a mediator for fast charges separation towards visible light driven photocatalytic hydrogen evolution. *Appl Surf Sci* 2019;463:747–57.
- [25] Hamilton JW, Byrne JA, Dunlop PS, Dionysiou DD, Pelaez M, O’Shea K, et al. Evaluating the mechanism of visible light activity for N, F-TiO<sub>2</sub> using photoelectrochemistry. *J Phys Chem C* 2014;118:12206–15.
- [26] Wang L, Zhao J, Liu H, Huang J. Design, modification and application of semiconductor photocatalysts. *J Taiwan Inst Chem Eng* 2018;93:590–602.
- [27] Acar C, Dincer I, Naterer GF. Review of photocatalytic water-splitting methods for sustainable hydrogen production. *Int J Energy Res* 2016;40:1449–73.
- [28] An X, Hu C, Liu H, Qu J. Hierarchical nanotubular anatase/rutile/TiO<sub>2</sub> (B) heterophase junction with oxygen vacancies for enhanced photocatalytic H<sub>2</sub> production. *Langmuir* 2018;34:1883–9.
- [29] Umer M, Tahir M, Azam MU, Tahir B, Musaab M. Self-doped Ti<sup>3+</sup> mediated TiO<sub>2</sub>/In<sub>2</sub>O<sub>3</sub>/SWCNTs heterojunction composite under acidic/basic heat medium for

- boosting visible light induced H<sub>2</sub> evolution. *Int J Hydrogen Energy* 2019;44: 13466–79.
- [30] Zhang M, Lin H, Cao J, Guo X, Chen S. Construction of novel S/CdS type II heterojunction for photocatalytic H<sub>2</sub> production under visible light: the intrinsic positive role of elementary  $\alpha$ -S. *Chem Eng J* 2017;321:484–94.
- [31] Zhao D, Yang C-F. Recent advances in the TiO<sub>2</sub>/CdS nanocomposite used for photocatalytic hydrogen production and quantum-dot-sensitized solar cells. *Renew Sustain Energy Rev* 2016;54:1048–59.
- [32] Liu X, Wang P, Zhai H, Zhang Q, Huang B, Wang Z, et al. Synthesis of synergistic phosphorus and cyano groups (CN) modified g-C<sub>3</sub>N<sub>4</sub> for enhanced photocatalytic H<sub>2</sub> production and CO<sub>2</sub> reduction under visible light irradiation. *Appl Catal, B* 2018;232:521–30.
- [33] Patnaik S, Sahoo DP, Parida K. An overview on Ag modified g-C<sub>3</sub>N<sub>4</sub> based nanostructured materials for energy and environmental applications. *Renew Sustain Energy Rev* 2018;82:1297–312.
- [34] Wang H, Chen W, Zhang J, Huang C, Mao L. Nickel nanoparticles modified CdS-a potential photocatalyst for hydrogen production through water splitting under visible light irradiation. *Int J Hydrogen Energy* 2015;40:340–5.
- [35] Buehler N, Meier K, Reber JF. Photochemical hydrogen production with cadmium sulfide suspensions. *J Phys Chem* 1984;88:3261–8.
- [36] Chen F, Luo W, Mo Y, Yu H, Cheng B. In situ photodeposition of amorphous CoS<sub>x</sub> on the TiO<sub>2</sub> towards hydrogen evolution. *Appl Surf Sci* 2018;430:448–56.
- [37] Tahir M. Hierarchical 3D VO<sub>2</sub>/ZnV<sub>2</sub>O<sub>4</sub> microspheres as an excellent visible light photocatalyst for CO<sub>2</sub> reduction to solar fuels. *Appl Surf Sci* 2019;467–468: 1170–80.
- [38] Wei S, Ni S, Xu X. A new approach to inducing Ti<sup>3+</sup> in anatase TiO<sub>2</sub> for efficient photocatalytic hydrogen production. *Chin J Catal* 2018;39:510–6.
- [39] Hossain A, Roy S, Sakthipandi K. The external and internal influences on the tuning of the properties of perovskites: an overview. *Ceram Int* 2019;45:4152–66.
- [40] Zhai H, Qi J, Zhang X, Li H, Yang L, Hu C, et al. Preparation and photocatalytic performance of hollow structure LiNb<sub>3</sub>O<sub>8</sub> photocatalysts. *Nanoscale Res Lett* 2017;12:519.
- [41] Grabowska E. Selected perovskite oxides: characterization, preparation and photocatalytic properties—a review. *Appl Catal, B* 2016;186:97–126.
- [42] Keeble D, Mackie R, Egger W, Löwe B, Pikart P, Hugenschmidt C, et al. Identification of vacancy defects in a thin film perovskite oxide. *Phys Rev B* 2010; 81:064102.
- [43] Moniruddin M, Ilyassov B, Zhao X, Smith E, Serikov T, Ibrayev N, et al. Recent progress on perovskite materials in photovoltaic and water splitting applications. *Mater Today Energy* 2018;7:246–59.
- [44] Clarizia L, Spasiano D, Di Somma I, Marotta R, Andreozzi R, Dionysiou DD. Copper modified-TiO<sub>2</sub> catalysts for hydrogen generation through photoreforming of organics. A short review. *Int J Hydrogen Energy* 2014;39:16812–31.
- [45] Dincer I, Acar C. Review and evaluation of hydrogen production methods for better sustainability. *Int J Hydrogen Energy* 2015;40:11094–111.
- [46] Kondarides DI, Daskalaki VM, Patsoura A, Verykios XE. Hydrogen production by photo-induced reforming of biomass components and derivatives at ambient conditions. *Catal Lett* 2008;122:26–32.
- [47] Abe R. Recent progress on photocatalytic and photoelectrochemical water splitting under visible light irradiation. *J Photochem Photobiol, A C* 2010;11: 179–209.
- [48] Tahir M, Amin NS. Advances in visible light responsive titanium oxide-based photocatalysts for CO<sub>2</sub> conversion to hydrocarbon fuels. *Energy Convers Manag* 2013;76:194–214.
- [49] Grewe T, Meggouh M, Tüysüz H. Nanocatalysts for solar water splitting and a perspective on hydrogen economy. *Chem Asian J* 2016;11:22–42.
- [50] Wen J, Xie J, Chen X, Li X. A review on g-C<sub>3</sub>N<sub>4</sub>-based photocatalysts. *Appl Surf Sci* 2017;391:72–123.
- [51] Colón G. Towards the hydrogen production by photocatalysis. *Appl Catal, A* 2016;518:48–59.
- [52] Hisatomi T, Kubota J, Domen K. Recent advances in semiconductors for photocatalytic and photoelectrochemical water splitting. *Chem Soc Rev* 2014;43: 7520–35.
- [53] Shi J, Guo L. ABO<sub>3</sub>-based photocatalysts for water splitting. *Prog Nat Sci* 2012;22: 592–615.
- [54] Zürch M, Chang H-T, Borja LJ, Kraus PM, Cushing SK, Gandman A, et al. Direct and simultaneous observation of ultrafast electron and hole dynamics in germanium. *Nat Commun* 2017;8:15734.
- [55] Liu B, Zhao X, Terashima C, Fujishima A, Nakata K. Thermodynamic and kinetic analysis of heterogeneous photocatalysis for semiconductor systems. *Phys Chem Chem Phys* 2014;16:8751–60.
- [56] Corma A, García H. Photocatalytic reduction of CO<sub>2</sub> for fuel production: possibilities and challenges. *J Catal* 2013;308:168–75.
- [57] Wang W-N, Soulis J, Yang YJ, Biswas P. Comparison of CO<sub>2</sub> photoreduction systems: a review. *Aerosol Air Qual. Res.* 2014;14:533–49.
- [58] Wu J, Lin H-M. Photo reduction of CO<sub>2</sub> to methanol via TiO<sub>2</sub> photocatalyst. *Int J Photoenergy* 2005;7:115–9.
- [59] Zhang R, Hu S, Lu C, Xu Z. Bandgap engineering of Gd<sub>0.8</sub>Ca<sub>0.2</sub>BaCo<sub>2</sub>O<sub>5+δ</sub> double perovskite for photocatalysis applications. *Ceram Int* 2018;44:15483–9.
- [60] Hu C-C, Teng H. Influence of structural features on the photocatalytic activity of NaTaO<sub>3</sub> powders from different synthesis methods. *Appl Catal, A* 2007;331: 44–50.
- [61] Niishiro R, Tanaka S, Kudo A. Hydrothermal-synthesized SrTiO<sub>3</sub> photocatalyst codoped with rhodium and antimony with visible-light response for sacrificial H<sub>2</sub> and O<sub>2</sub> evolution and application to overall water splitting. *Appl Catal, B* 2014; 150:187–96.
- [62] Chen Z, Xing P, Chen P, Chen Q, Wang Y, Yu J, et al. Synthesis of carbon doped KTaO<sub>3</sub> and its enhanced performance in photocatalytic H<sub>2</sub> generation. *Catal Commun* 2018;109:6–9.
- [63] Husin H, Chen H-M, Su W-N, Pan C-J, Chuang W-T, Sheu H-S, et al. Green fabrication of La-doped NaTaO<sub>3</sub> via H<sub>2</sub>O<sub>2</sub> assisted sol–gel route for photocatalytic hydrogen production. *Appl Catal, B* 2011;102:343–51.
- [64] Liu J, Chen G, Li Z, Zhang Z. Hydrothermal synthesis and photocatalytic properties of ATaO<sub>3</sub> and ANbO<sub>3</sub> (A= Na and K). *Int J Hydrogen Energy* 2007;32: 2269–72.
- [65] Modak B, Modak P, Ghosh SK. Improving visible light photocatalytic activity of NaNbO<sub>3</sub>: DFT based investigation. *RSC Adv* 2016;6:90188–96.
- [66] Kumar S, Partha Sarathy R, Singh AP, Wickman B, Thirumal M, Ganguli AK. Dominant {100} facet selectivity for enhanced photocatalytic activity of NaNbO<sub>3</sub> in NaNbO<sub>3</sub>/CdS core/shell heterostructures. *Catal Sci* 2017;7:481–95.
- [67] Liu Q, Chai Y, Zhang L, Ren J, Dai W-L. Highly efficient Pt/NaNbO<sub>3</sub> nanowire photocatalyst: its morphology effect and application in water purification and H<sub>2</sub> production. *Appl Catal, B* 2017;205:505–13.
- [68] Zielińska B, Borowiak-Palen E, Kalenczuk RJ. Preparation, characterization and photocatalytic activity of metal-loaded NaNbO<sub>3</sub>. *J Phys Chem Solid* 2011;72: 117–23.
- [69] Huang C-M, Cheng K-W, Pan G-T, Chang W-S, Yang TC-K. CTAB-assisted hydrothermal synthesis of silver vanadates and their photocatalytic characterization. *Chem Eng Sci* 2010;65:148–52.
- [70] Alammar T, Hamm I, Wark M, Mudring A-V. Low-temperature route to metal titanate perovskite nanoparticles for photocatalytic applications. *Appl Catal, B* 2015;178:20–8.
- [71] Ikeue K, Yamamoto Y, Suzuki M. Photocatalytic activity for hydrogen evolution of heteroatom-doped SrTiO<sub>3</sub> prepared using a graphitic-carbon nitride nanosheet. *Ceramics* 2020;3:22–30.
- [72] Sharma P, Lee C-T, Wu JC-S. Sunlight-driven photocatalytic hydrogen production from water using metal-doped Strontium Titanate perovskite. *ChemRxiv* 2020.
- [73] Carrasco-Jáim OA, Mora-Hernandez JM, Torres-Martínez LM, Moctezuma E. A comparative study on the photocatalytic hydrogen production of ATiO<sub>3</sub> (A = Zn, Cd and Pb) perovskites and their photoelectrochemical properties. *J Photochem Photobiol, A* 2019;371:98–108.
- [74] Zhang H, Chen G, Li Y, Teng Y. Electronic structure and photocatalytic properties of copper-doped CaTiO<sub>3</sub>. *Int J Hydrogen Energy* 2010;35:2713–6.
- [75] Zhao H, Duan Y, Sun X. Synthesis and characterization of CaTiO<sub>3</sub> particles with controlled shape and size. *New J Chem* 2013;37:986–91.
- [76] Lozano-Sánchez LM, Méndez-Medrano MG, Colbeau-Justin C, Rodríguez-López JL, Hernández-Ureña DB, Obregón S. Long-lived photoinduced charge-carriers in Er<sup>3+</sup> doped CaTiO<sub>3</sub> for photocatalytic H<sub>2</sub> production under UV irradiation. *Catal Commun* 2016;84:36–9.
- [77] Wang R, Ni S, Liu G, Xu X. Hollow CaTiO<sub>3</sub> cubes modified by La/Cr co-doping for efficient photocatalytic hydrogen production. *Appl Catal* 2018;225:139–47.
- [78] Nikolic MV, Vasiljevic ZZ, Lukovic MD, Pavlovic VP, Vujancevic J, Radovanovic M, et al. Humidity sensing properties of nanocrystalline pseudobrookite (Fe<sub>2</sub>TiO<sub>5</sub>) based thick films. *Sensor Actuator B Chem* 2018;277: 654–64.
- [79] Bassi PS, Chiam SY, Barber J, Wong LH. Hydrothermal grown nanoporous iron based titanate, Fe<sub>2</sub>TiO<sub>5</sub> for light driven water splitting. *ACS Appl Mater Interfaces* 2014;6:22490–5.
- [80] Bhoi YP, Fang F, Zhou X, Li Y, Sun X, Wang J, et al. Single step combustion synthesis of novel Fe<sub>2</sub>TiO<sub>5</sub>/ $\alpha$ -Fe<sub>2</sub>O<sub>3</sub>/TiO<sub>2</sub> ternary photocatalyst with combined double type-II cascade charge migration processes and efficient photocatalytic activity. *Appl Surf Sci* 2020;525:146571.
- [81] Zhang N, Qu Y, Pan K, Wang G, Li Y. Synthesis of pure phase Mg<sub>1.2</sub>Ti<sub>1.8</sub>O<sub>5</sub> and MgTiO<sub>3</sub> nanocrystals for photocatalytic hydrogen production. *Nano Res* 2016;9: 726–34.
- [82] Zhang G, Liu G, Wang L, Irvine JT. Inorganic perovskite photocatalysts for solar energy utilization. *Chem Soc Rev* 2016;45:5951–84.
- [83] Zhang N, Qu Y, Pan K, Wang G, Li Y. Synthesis of pure phase Mg<sub>1.2</sub>Ti<sub>1.8</sub>O<sub>5</sub> and MgTiO<sub>3</sub> nanocrystals for photocatalytic hydrogen production. *Nano Res* 2016;9: 726–34.
- [84] Guo Z, Sa B, Pathak B, Zhou J, Ahuja R, Sun Z. Band gap engineering in huge-gap semiconductor SrZrO<sub>3</sub> for visible-light photocatalysis. *Int J Hydrogen Energy* 2014;39:2042–8.
- [85] Tian Q, Zhang L, Liu J, Li N, Ma Q, Zhou J, et al. Synthesis of MoS<sub>2</sub>/SrZrO<sub>3</sub> heterostructures and their photocatalytic H<sub>2</sub> evolution under UV irradiation. *RSC Adv* 2014;5:734–9.
- [86] Chen D, Ye J. SrSnO<sub>3</sub> nanostructures: synthesis, characterization, and photocatalytic properties. *Chem Mater* 2007;19:4585–91.
- [87] Lee CW, Kim DW, Cho IS, Park S, Shin SS, Seo SW, et al. Simple synthesis and characterization of SrSnO<sub>3</sub> nanoparticles with enhanced photocatalytic activity. *Int J Hydrogen Energy* 2012;37:10557–63.
- [88] Zhang WF, Tang J, Ye J. Photoluminescence and photocatalytic properties of SrSnO<sub>3</sub> perovskite. *Chem Phys Lett* 2006;418:174–8.
- [89] Zhang W, Tang J, Ye J. Structural, photocatalytic, and photophysical properties of perovskite MSnO<sub>3</sub> (M= Ca, Sr, and Ba) photocatalysts. *J Mater Res* 2007;22: 1859–71.
- [90] Lin Y, Yuan G, Sheehan S, Zhou S, Wang D. Hematite-based solar water splitting: challenges and opportunities. *Energy Environ Sci* 2011;4:4862–9.
- [91] Tang P, Tong Y, Chen H, Cao F, Pan G. Microwave-assisted synthesis of nanoparticulate perovskite LaFeO<sub>3</sub> as a high active visible-light photocatalyst. *Curr Appl Phys* 2013;13:340–3.

- [92] Chen S, Wang L-W. Thermodynamic oxidation and reduction potentials of photocatalytic semiconductors in aqueous solution. *Chem Mater* 2012;24: 3659–66.
- [93] Iervolino G, Vaiano V, Sannino D, Rizzo L, Palma V. Enhanced photocatalytic hydrogen production from glucose aqueous matrices on Ru-doped LaFeO<sub>3</sub>. *Appl Catal, B* 2017;207:182–94.
- [94] Yang Y, Kang L, Li H. Enhancement of photocatalytic hydrogen production of BiFeO<sub>3</sub> by Gd<sup>3+</sup> doping. *Ceram Int* 2019;45:8017–22.
- [95] Tijare S, Bakardjieva S, Subrt J, Joshi M, Rayalu S, Hishita S, et al. Synthesis and visible light photocatalytic activity of nanocrystalline PrFeO<sub>3</sub> perovskite for hydrogen generation in ethanol–water system. *J Chem Sci* 2014;126:517–25.
- [96] Kanhere P, Chen Z. A review on visible light active perovskite-based photocatalysts. *Molecules* 2014;19:19995–2022.
- [97] Li P, Ouyang S, Xi G, Kako T, Ye J. The effects of crystal structure and electronic structure on photocatalytic H<sub>2</sub> evolution and CO<sub>2</sub> reduction over two phases of perovskite-structured NaNbO<sub>3</sub>. *J Phys Chem C* 2012;116:7621–8.
- [98] Hu C-C, Lee Y-L, Teng H. Efficient water splitting over Na<sub>1-x</sub>K<sub>x</sub>TaO<sub>3</sub> photocatalysts with cubic perovskite structure. *J Mater Chem* 2011;21:3824–30.
- [99] Meziani D, Reziga A, Rekhila G, Bellal B, Trari M. Hydrogen evolution under visible light over LaCoO<sub>3</sub> prepared by chemical route. *Energy Convers Manag* 2014;82:244–9.
- [100] Kong J, Yang T, Rui Z, Ji H. Perovskite-based photocatalysts for organic contaminants removal: current status and future perspectives. *Catal Today* 2019; 327:47–63.
- [101] Zhang P, Wang T, Gong J. Current mechanistic understanding of surface reactions over water-splitting photocatalysts. *Inside Chem* 2018;4:223–45.
- [102] Chiarello GL, Aguirre MH, Sellli E. Hydrogen production by photocatalytic steam reforming of methanol on noble metal-modified TiO<sub>2</sub>. *J Catal* 2010;273:182–90.
- [103] Low J, Cheng B, Yu J. Surface modification and enhanced photocatalytic CO<sub>2</sub> reduction performance of TiO<sub>2</sub>: a review. *Appl Surf Sci* 2017;392:658–86.
- [104] Puangpitch T, Chavadej S, Sreethawong T. Hydrogen production over Au-loaded mesoporous-assembled SrTiO<sub>3</sub> nanocrystal photocatalyst: effects of molecular structure and chemical properties of hole scavengers. *Energy Convers Manag* 2011;52:2256–61.
- [105] Husin H, Chen H-M, Su W-N, Pan C-J, Chuang W-T, Sheu H-S, et al. Green fabrication of La-doped NaTaO<sub>3</sub> via H<sub>2</sub>O<sub>2</sub> assisted sol–gel route for photocatalytic hydrogen production. *Appl Catal* 2011;102:343–51.
- [106] Yu H, Yan S, Li Z, Yu T, Zou Z. Efficient visible-light-driven photocatalytic H<sub>2</sub> production over Cr/N-codoped SrTiO<sub>3</sub>. *Int J Hydrogen Energy* 2012;37:12120–7.
- [107] Huerta-Flores AM, Torres-Martínez LM, Moctezuma E, Ceballos-Sánchez O. Enhanced photocatalytic activity for hydrogen evolution of SrZrO<sub>3</sub> modified with earth abundant metal oxides (MO, M=Cu, Ni, Fe, Co). *Fuel* 2016;181:670–9.
- [108] Meng J, Fu X, Du K, Chen X, Lin Q, Wei X, et al. BaZrO<sub>3</sub> hollow nanostructure with Fe (III) doping for photocatalytic hydrogen evolution under visible light. *Int J Hydrogen Energy* 2018;43:9224–32.
- [109] Gupta B, Melvin AA. TiO<sub>2</sub>/RGO composites: its achievement and factors involved in hydrogen production. *Renew Sustain Energy Rev* 2017;76:1384–92.
- [110] Dosado AG, Chen W-T, Chan A, Sun-Waterhouse D, Waterhouse GI. Novel Au/TiO<sub>2</sub> photocatalysts for hydrogen production in alcohol–water mixtures based on hydrogen titanate nanotube precursors. *J Catal* 2015;330:238–54.
- [111] Tahir M, Siraj M, Tahir B, Umer M, Alias H, Othman N. Au-NPs embedded Z-scheme WO<sub>3</sub>/TiO<sub>2</sub> nanocomposite for plasmon-assisted photocatalytic glycerol–water reforming towards enhanced H<sub>2</sub> evolution. *Appl Surf Sci* 2020; 503.
- [112] Kim SM, Lee H, Park JY. Charge transport in metal–oxide interfaces: genesis and detection of hot electron flow and its role in heterogeneous catalysis. *Catal Lett* 2015;145:299–308.
- [113] Xu X, Liu G, Azad AK. Visible light photocatalysis by in situ growth of plasmonic Ag nanoparticles upon AgTaO<sub>3</sub>. *Int J Hydrogen Energy* 2015;40:3672–8.
- [114] Tiwari D, Dunn S, Zhang Q. Impact of Zr/Ti ratio in the PZT on the photoreduction of silver nanoparticles. *Mater Res Bull* 2009;44:1219–24.
- [115] Devarajan S, Bera P, Sampath S. Bimetallic nanoparticles: a single step synthesis, stabilization, and characterization of Au–Ag, Au–Pd, and Au–Pt in sol–gel derived silicates. *J Colloid Interface Sci* 2005;290:117–29.
- [116] Sakai T, Alexandridis P. Ag and Au monometallic and bimetallic colloids: morphogenesis in amphiphilic block copolymer solutions. *Chem Mater* 2006;18: 2577–83.
- [117] Rodríguez-Torres J, Gómez-Solís C, Torres-Martínez LM, Juárez-Ramírez I. Synthesis and characterization of Au-Pd/NaTaO<sub>3</sub> multilayer films for photocatalytic hydrogen production. *J Photochem Photobiol Chem* 2017;332: 208–14.
- [118] Nithya PM, Devi LG. Effect of surface Ag metallization on the photocatalytic properties of BaTiO<sub>3</sub>: surface plasmon effect and variation in the Schottky barrier height. *Surf Interfaces* 2019;15:205–15.
- [119] Zhang D, Ma X, Zhang H, Liao Y, Xiang Q. Enhanced photocatalytic hydrogen evolution activity of carbon and nitrogen self-doped TiO<sub>2</sub> hollow sphere with the creation of oxygen vacancy and Ti<sup>3+</sup>. *Mater.Today Energy* 2018;10:132–40.
- [120] Wang R, Zhu Y, Qiu Y, Leung C-F, He J, Liu G, et al. Synthesis of nitrogen-doped KNbO<sub>3</sub> nanocubes with high photocatalytic activity for water splitting and degradation of organic pollutants under visible light. *Chem Eng J* 2013;226: 123–30.
- [121] Rao MP, Nandhini VP, Wu JJ, Syed A, Ameen F, Anandan S. Synthesis of N-doped potassium tantalate perovskite material for environmental applications. *J Solid State Chem* 2018;258:647–55.
- [122] Zhang X, Liu A, Cao Y, Xie J, Jia W, Jia D. Interstitial N-doped SrSnO<sub>3</sub> perovskite: structural design, modification and photocatalytic degradation of dyes. *New J Chem* 2019;43:10965–72.
- [123] Chen T, Meng J, Lin Q, Wei X, Li J, Zhang Z. One-step synthesis of hollow BaZrO<sub>3</sub> nanocrystals with oxygen vacancies for photocatalytic hydrogen evolution from pure water. *J Alloys Compd* 2019;780:498–503.
- [124] Jiang Z, Pan J, Wang B, Li C. Two dimensional Z-scheme AgCl/Ag/CaTiO<sub>3</sub> nanoheterojunctions for photocatalytic hydrogen production enhancement. *Appl Surf Sci* 2018;436:519–26.
- [125] Qu Z, Wang J, Tang J, Shu X, Liu X, Zhang Z, et al. Carbon quantum dots/KNbO<sub>3</sub> hybrid composites with enhanced visible-light driven photocatalytic activity toward dye waste-water degradation and hydrogen production. *Mol Catal* 2018; 445:1–11.
- [126] Yu J, Chen Z, Zeng L, Ma Y, Feng Z, Wu Y, et al. Synthesis of carbon-doped KNbO<sub>3</sub> photocatalyst with excellent performance for photocatalytic hydrogen production. *Sol Energy Mater Sol Cells* 2018;179:45–56.
- [127] Zhou D, Zhai P, Hu G, Yang J. Upconversion luminescence and enhanced photocatalytic hydrogen production for Er<sup>3+</sup> doped SrTiO<sub>3</sub> nanoparticules. *Chem Phys Lett* 2018;711:77–80.
- [128] Han J, Liu Y, Dai F, Zhao R, Wang L. Fabrication of CdSe/CaTiO<sub>3</sub> nanocomposites in aqueous solution for improved photocatalytic hydrogen production. *Appl Surf Sci* 2018;459:520–6.
- [129] Carrasco-Jáim OA, Torres-Martínez LM, Moctezuma E. Enhanced photocatalytic hydrogen production of AgMoO<sub>3</sub> (M = Ta, Nb, V) perovskite materials using CdS and NiO as co-catalysts. *J Photochem Photobiol, A* 2018;358:167–76.
- [130] Yu J, Chen Z, Chen Q, Wang Y, Lin H, Hu X, et al. Giant enhancement of photocatalytic H<sub>2</sub> production over KNbO<sub>3</sub> photocatalyst obtained via carbon doping and MoS<sub>2</sub> decoration. *Int J Hydrogen Energy* 2018;43:4347–54.
- [131] Huerta-Flores AM, Chen J, Torres-Martínez LM, Ito A, Moctezuma E, Goto T. Laser assisted chemical vapor deposition of nanostructured NaTaO<sub>3</sub> and SrTiO<sub>3</sub> thin films for efficient photocatalytic hydrogen evolution. *Fuel* 2017;197:174–85.
- [132] Wu M, Luo M, Guo M, Jia L. Sugarcane bagasse hydrolysis by metal ions mediated synthesis of perovskite LaCoO<sub>3</sub> and the photocatalytic performance for hydrogen from formaldehyde solution under visible light. *ACS Sustainable Chem Eng* 2017; 5:11558–65.
- [133] Guo Y, Li Y, Li S, Zhang L, Li Y, Wang J. Enhancement of visible-light photocatalytic activity of Pt supported potassium niobate (Pt-KNbO<sub>3</sub>) by up-conversion luminescence agent (Er<sup>3+</sup>:Y<sub>3</sub>Al<sub>5</sub>O<sub>12</sub>) for hydrogen evolution from aqueous methanol solution. *Energy* 2015;82:72–9.
- [134] Li Y, Gou H, Lu J, Wang C. A two-step synthesis of NaTaO<sub>3</sub> microspheres for photocatalytic water splitting. *Int J Hydrogen Energy* 2014;39:13481–5.
- [135] Tan H, Zhao Z, Zhu W-b, Coker EN, Li B, Zheng M, et al. Oxygen vacancy enhanced photocatalytic activity of perovskite SrTiO<sub>3</sub>. *ACS Appl Mater Interfaces* 2014;6:19184–90.
- [136] Jiang W, Jiao X, Chen D. Photocatalytic water splitting of surfactant-free fabricated high surface area NaTaO<sub>3</sub> nanocrystals. *Int J Hydrogen Energy* 2013; 38:12739–46.
- [137] Yan L, Zhang J, Zhou X, Wu X, Lan J, Wang Y, et al. Crystalline phase-dependent photocatalytic water splitting for hydrogen generation on KNbO<sub>3</sub> submicro-crystals. *Int J Hydrogen Energy* 2013;38:3554–61.
- [138] Zhang T, Zhao K, Yu J, Jin J, Qi Y, Li H, et al. Photocatalytic water splitting for hydrogen generation on cubic, orthorhombic, and tetragonal KNbO<sub>3</sub> microcubes. *Nanoscale* 2013;5:8375–83.
- [139] Xu X, Randorn C, Efstratiou P, Irvine JTS. A red metallic oxide photocatalyst. *Nat Mater* 2012;11:595.
- [140] Dhanasekaran P, Gupta N. Factors affecting the production of H<sub>2</sub> by water splitting over a novel visible-light-driven photocatalyst GaFeO<sub>3</sub>. *Int J Hydrogen Energy* 2012;37:4897–907.
- [141] Shi J, Liu G, Wang N, Li C. Microwave-assisted hydrothermal synthesis of perovskite NaTaO<sub>3</sub> nanocrystals and their photocatalytic properties. *J Mater Chem* 2012;22:18808–13.
- [142] Khan Z, Qureshi M. Tantalum doped BaZrO<sub>3</sub> for efficient photocatalytic hydrogen generation by water splitting. *Catal Commun* 2012;28:82–5.
- [143] Arney D, Hardy C, Greve B, Maggad PA. Flux synthesis of AgNbO<sub>3</sub>: effect of particle surfaces and sizes on photocatalytic activity. *J Photochem Photobiol, A* 2010;214:54–60.
- [144] Torres-Martínez LM, Gómez R, Vázquez-Cuchillo O, Juárez-Ramírez I, Cruz-López A, Alejandre-Sandoval FJ. Enhanced photocatalytic water splitting hydrogen production on RuO<sub>2</sub>/La:NaTaO<sub>3</sub> prepared by sol–gel method. *Catal Commun* 2010;12:268–72.
- [145] Husin H, Chen H-M, su w-n, Pan C-J, Chuang W-T, Sheu H-S, et al. Green fabrication of La-doped NaTaO<sub>3</sub> via H<sub>2</sub>O<sub>2</sub> assisted sol–gel route for photocatalytic hydrogen production 2011;102:343–51.
- [146] Fu X, Wang X, Leung DYC, Xue W, Ding Z, Huang H, et al. Photocatalytic reforming of glucose over La doped alkali tantalate photocatalysts for H<sub>2</sub> production. *Catal Commun* 2010;12:184–7.
- [147] Jia L, Li J, Fang W. Effect of H<sub>2</sub>/CO<sub>2</sub> mixture gas treatment temperature on the activity of LaNiO<sub>3</sub> catalyst for hydrogen production from formaldehyde aqueous solution under visible light. *J Alloys Compd* 2010;489:L13–6.
- [148] Parida KM, Reddy KH, Martha S, Das DP, Biswal N. Fabrication of nanocrystalline LaFeO<sub>3</sub>: an efficient sol–gel auto-combustion assisted visible light responsive photocatalyst for water decomposition. *Int J Hydrogen Energy* 2010;35:12161–8.
- [149] Ding Q-P, Yuan Y-P, Xiong X, Li R-P, Huang H-B, Li Z-S, et al. Enhanced photocatalytic water splitting properties of KNbO<sub>3</sub> nanowires synthesized through hydrothermal method. *J Phys Chem C* 2008;112:18846–8.

- [150] Yuan Y, Zhang X, Liu L, Jiang X, Lv J, Li Z, et al. Synthesis and photocatalytic characterization of a new photocatalyst BaZrO<sub>3</sub>. Int J Hydrogen Energy 2008;33: 5941–6.
- [151] Liu JW, Chen G, Li ZH, Zhang ZG. Hydrothermal synthesis and photocatalytic properties of ATaO<sub>3</sub> and ANbO<sub>3</sub> (A=Na and K). Int J Hydrogen Energy 2007;32: 2269–72.
- [152] Fuertes A. Chemistry and applications of oxynitride perovskites. J Mater Chem 2012;22:3293–9.
- [153] Zou J-P, Zhang L-Z, Luo S-L, Leng L-H, Luo X-B, Zhang M-J, et al. Preparation and photocatalytic activities of two new Zn-doped SrTiO<sub>3</sub> and BaTiO<sub>3</sub> photocatalysts for hydrogen production from water without cocatalysts loading. Int J Hydrogen Energy 2012;37:17068–77.
- [154] Wang L, Wang W. Photocatalytic hydrogen production from aqueous solutions over novel Bi<sub>0.5</sub>Na<sub>0.5</sub>TiO<sub>3</sub> microspheres. Int J Hydrogen Energy 2012;37:3041–7.
- [155] Hu C-C, Lee Y-L, Teng H. Efficient water splitting over Na<sub>1-x</sub>K<sub>x</sub>TaO<sub>3</sub> photocatalysts with cubic perovskite structure. J Mater Chem 2011;21:3824–30.
- [156] Lu Y, Zhao H, Li K, Du X, Ma Y, Chang X, et al. Effective calcium doping at the B-site of BaFeO<sub>3-x</sub> perovskite: towards low-cost and high-performance oxygen permeation membranes. J Mater Chem 2017;5:7999–8009.
- [157] Lu Y, Zhao H, Li K, Du X, Ma Y, Chang X, et al. Effective calcium doping at the B-site of BaFeO<sub>3-x</sub> perovskite: towards low-cost and high-performance oxygen permeation membranes. J Mater Chem 2017;5:7999–8009.
- [158] Husin H, Adisalamu Sy Y, Asnawi TM, Hasfita F. Pt nanoparticle on La<sub>0.02</sub>Na<sub>0.98</sub>TaO<sub>3</sub> catalyst for hydrogen evolution from glycerol aqueous solution. AIP Conf Proc 2017;1788:030073.
- [159] Shi J, Ye J, Zhou Z, Li M, Guo L. Hydrothermal synthesis of Na<sub>0.5</sub>La<sub>0.5</sub>TiO<sub>3</sub>–LaCrO<sub>3</sub> solid-solution single-crystal nanocubes for visible-light-driven photocatalytic H<sub>2</sub> evolution. Chem Eur 2011;17:7858–67.
- [160] Yan SC, Wang ZQ, Li ZS, Zou ZG. Photocatalytic activities for water splitting of La-doped-NaTaO<sub>3</sub> fabricated by microwave synthesis. Solid State Ionics 2009; 180:1539–42.
- [161] Xu L, Li C, Shi W, Guan J, Sun Z. Visible light-response NaTa<sub>1-x</sub>Cu<sub>x</sub>O<sub>3</sub> photocatalysts for hydrogen production from methanol aqueous solution. J Mol Catal Chem 2012;360:42–7.
- [162] Mondal I, Srikanth M, Srinivasu K, Soujanya Y, Pal U. Understanding the structural and electronic effect of Zr<sup>4+</sup>-doped KNb (Zr) O<sub>3</sub> perovskite for enhanced photoactivity: a combined experimental and computational study. J Phys Chem 2017;121:2597–604.
- [163] Wang M, Fang M, Min X, Huang Z, Tang C, Liu Yg, et al. Molten salt synthesis of NaNb<sub>x</sub>Ta<sub>1-x</sub>O<sub>3</sub> perovskites with enhanced photocatalytic activity. Chem Phys Lett 2017;686:18–25.
- [164] Chen Z, Chen P, Xing P, Hu X, Lin H, Wu Y, et al. Novel carbon modified KTa<sub>0.75</sub>Nb<sub>0.25</sub>O<sub>3</sub> nanocubes with excellent efficiency in photocatalytic H<sub>2</sub> evolution. Fuel 2018;233:486–96.
- [165] Jana P, de la Peña O’Shea VA, Mata Montero C, Pizarro P, Coronado JM, Fresno F, et al. Factors influencing the photocatalytic activity of alkali NbTa perovskites for hydrogen production from aqueous methanol solutions. Int J Hydrogen Energy 2016;41:19921–8.
- [166] Hagiwara H, Nagatomo M, Ida S, Ishihara T. Photocatalytic splitting of water into hydrogen and oxygen on organic dye modified KTa(Zr)O<sub>3</sub> catalyst. Energy Procedia 2012;22:53–60.
- [167] Jeong E, Yu S, Yoon J, Bae J, Cho C, Lim K, et al. Efficient visible light photocatalysis in cubic Sr<sub>2</sub>FeNbO<sub>6</sub>. J Ceram Process Res 2012;13:305–9.
- [168] Xu Zong GW, Yan Hongjian, Ma Guijun, Shi Jingying, Wen Fuyu, Wang Lu, Li Can. Photocatalytic H<sub>2</sub> evolution on Mo<sub>2</sub>S/CdS catalysts under visible light irradiation. J Phys Chem C 2010;114:1963–8.
- [169] Li J, Zeng J, Jia L, Fang W. Investigations on the effect of Cu<sup>2+</sup>/Cu<sup>1+</sup> redox couples and oxygen vacancies on photocatalytic activity of treated LaNi<sub>1-x</sub>Cu<sub>x</sub>O<sub>3</sub> (x= 0.1, 0.4, 0.5). Int J Hydrogen Energy 2010;35:12733–40.
- [170] Yuan Y, Zhao Z, Zheng J, Yang M, Qiu L, Li Z, et al. Polymerizable complex synthesis of BaZr<sub>1-x</sub>Sn<sub>x</sub>O<sub>3</sub> photocatalysts: role of Sn<sup>4+</sup> in the band structure and their photocatalytic water splitting activities. J Mater Chem 2010;20:6772–9.
- [171] Liu JW, Chen G, Li ZH, Zhang ZG. Electronic structure and visible light photocatalysis water splitting property of chromium-doped SrTiO<sub>3</sub>. J Solid State Chem 2006;179:3704–8.
- [172] Nishimoto S, Matsuda M, Miyake M. Photocatalytic activities of Rh-doped CaTiO<sub>3</sub> under visible light irradiation. Chem Lett 2006;35:308–9.
- [173] Yin J, Zou Z, Ye J. Photophysical and photocatalytic activities of a novel photocatalyst BaZn<sub>1/3</sub>Nb<sub>2/3</sub>O<sub>3</sub>. J Phys Chem B 2004;108:12790–4.
- [174] Yin J, Zou Z, Ye J. A novel series of the new visible-light-driven photocatalysts MC<sub>1/3</sub>Nb<sub>2/3</sub>O<sub>3</sub> (M= Ca, Sr, and Ba) with special electronic structures. J Phys Chem B 2003;107:4936–41.
- [175] Yin J, Zou Z, Ye J. Photophysical and photocatalytic properties of Mn<sub>0.5</sub>Nb<sub>0.5</sub>O<sub>3</sub> (M= Ca, Sr, and Ba). J Phys Chem B 2003;107:61–5.
- [176] Maeda K, Teramura K, Lu D, Takata T, Saito N, Inoue Y, et al. Photocatalyst releasing hydrogen from water. Nature 2006;440:295.
- [177] Lv M, Xie Y, Wang Y, Sun X, Wu F, Chen H, et al. Bismuth and chromium co-doped strontium titanates and their photocatalytic properties under visible light irradiation. Phys Chem Chem Phys 2015;17:26320–9.
- [178] Lu L, Lv M, Wang D, Liu G, Xu X. Efficient photocatalytic hydrogen production over solid solutions Sr<sub>1-x</sub>B<sub>x</sub>Ti<sub>1-x</sub>Fe<sub>x</sub>O<sub>3</sub> (0≤x≤0.5). Appl Catal, B 2017;200:412–9.
- [179] Pan C, Takata T, Nakabayashi M, Matsumoto T, Shibata N, Ikuhara Y, et al. A complex perovskite-type oxynitride: the first photocatalyst for water splitting operable at up to 600 nm. Angew Chem Int Ed 2015;54:2955–9.
- [180] Lu L, Ni S, Liu G, Xu X. Structural dependence of photocatalytic hydrogen production over La/Cr co-doped perovskite compound ATiO<sub>3</sub> (A = Ca, Sr and Ba). Int J Hydrogen Energy 2017;42:23539–47.
- [181] Kang HW, Lim SN, Park SB, Park A-HA. H<sub>2</sub> evolution under visible light irradiation on La and Cr co-doped NaTaO<sub>3</sub> prepared by spray pyrolysis from polymeric precursor. Int J Hydrogen Energy 2013;38:6323–34.
- [182] Zhang H, Chen G, He X, Xu J. Electronic structure and photocatalytic properties of Ag-La codoped CaTiO<sub>3</sub>. J Alloys Compd 2012;516:91–5.
- [183] Yi Z, Ye J. Band gap tuning of Na<sub>1-x</sub>La<sub>x</sub>Ta<sub>1-x</sub>Cr<sub>x</sub>O<sub>3</sub> for H<sub>2</sub> generation from water under visible light irradiation. J Appl Phys 2009;106:074910.
- [184] Kawashima K, Hojaberdirov M, Wagata H, Zahedi E, Yubuta K, Domen K, et al. Two-step synthesis and visible-light-driven photocatalytic water oxidation activity of AW(O,N)<sub>3</sub> (A=Sr, La, Pr, Nd and Eu) perovskites. J Catal 2016;344: 29–37.
- [185] Ebbinghaus SG, Abicht H-P, Drönskowsky R, Müller T, Reiller A, Weidenkaff A. Perovskite-related oxynitrides – recent developments in synthesis, characterisation and investigations of physical properties. Prog Solid State Chem 2009;37:173–205.
- [186] Balazs A, Portet SH, Woodward PM, Brillson LJ. Electronic structure of tantalum oxynitride perovskite photocatalysts. Chem Mater 2013;25:3337–43.
- [187] Hara M, Takata T, Kondo JN, Domen K. Photocatalytic reduction of water by TaON under visible light irradiation. Catal Today 2004;90:313–7.
- [188] Kasahara A, Nukumizu K, Hitoki G, Takata T, Kondo JN, Hara M, et al. Photoreactions on LaTiO<sub>2</sub>N under visible light irradiation. J Phys Chem 2002; 106:6750–3.
- [189] Qi Y, Chen S, Li M, Ding Q, Li Z, Cui J, et al. Achievement of visible-light-driven Z-scheme overall water splitting using barium-modified Ta<sub>3</sub>N<sub>5</sub> as a H<sub>2</sub>-evolving photocatalyst. Chem Sci 2017;8:437–43.
- [190] Siriratnakul B, Maeda K, Hisatomi T, Domen K. Synthesis and photocatalytic activity of perovskite niobium oxynitrides with wide visible-light absorption bands. ChemSusChem 2011;4:74–8.
- [191] Matsukawa M, Ishikawa R, Hisatomi T, Moriya Y, Shibata N, Kubota J, et al. Enhancing photocatalytic activity of LaTiO<sub>2</sub>N by removal of surface reconstruction layer. Nano Lett 2014;14:1038–41.
- [192] Sasaki R, Maeda K, Kako Y, Domen K. Preparation of calcium tantalum oxynitride from layered oxide precursors to improve photocatalytic activity for hydrogen evolution under visible light. Appl Catal, B 2012;128:72–6.
- [193] Higashi M, Abe R, Takata T, Domen K. Photocatalytic overall water splitting under visible light using ATaO<sub>2</sub>N (A= Ca, Sr, Ba) and WO<sub>3</sub> in a IO<sub>3-</sub>/I- shuttle redox mediated system. Chem Mater 2009;21:1543–9.
- [194] Yamasita D, Takata T, Hara M, Kondo JN, Domen K. Recent progress of visible-light-driven heterogeneous photocatalysts for overall water splitting. Solid State Ionics 2004;172:591–5.
- [195] Zhang L, Liang W. How the structures and properties of two-dimensional layered perovskites MAPbI<sub>3</sub> and CsPbI<sub>3</sub> vary with the number of layers. J Phys Chem Lett 2017;8:1517–23.
- [196] Kato M, Imai Y, Kajita T, Takarabe Y, Minakawa T, Nemoto K-i, et al. Synthesis of oxide superconductors by soft-chemical techniques. Mat Sci Eng B-Adv 2008;148: 53–7.
- [197] Machida M, Miyazaki K, Matsushima S, Arai M. Photocatalytic properties of layered perovskite tantalates, MLnTa<sub>2</sub>O<sub>7</sub> (M= Cs, Rb, Na, and H; Ln= La, Pr, Nd, and Sm). J Mater Chem 2003;13:1433–7.
- [198] Zhang P, Hua X, Teng X, Liu D, Qin Z, Ding S. CTAB assisted hydrothermal synthesis of lamellar Bi<sub>2</sub>WO<sub>6</sub> with superior photocatalytic activity for rhodamine b degradation. Mater Lett 2016;185:275–7.
- [199] Chen Z, Jiang X, Zhu C, Shi C. Chromium-modified Bi<sub>4</sub>Ti<sub>3</sub>O<sub>12</sub> photocatalyst: application for hydrogen evolution and pollutant degradation. Appl Catal, B 2016;199:241–51.
- [200] Bai Y, Chen J, Wu X, Zhao S. Photovoltaic behaviors regulated by band-gap and bipolar electrical cycling in Holmium-doped Bi<sub>5</sub>Ti<sub>3</sub>FeO<sub>15</sub> ferroelectric films. J Phys Chem C 2016;120:24637–45.
- [201] Kulischow N, Ladasiu C, Marschall R. Layered Dion-Jacobson type niobium oxides for photocatalytic hydrogen production prepared via molten salt synthesis. Catal Today 2017;287:65–9.
- [202] Fajrina N, Tahir M. A critical review in strategies to improve photocatalytic water splitting towards hydrogen production 2019;44:540–77.
- [203] Wang Q, Hisatomi T, Ma SSK, Li Y, Domen K. Core/Shell structured La- and Rh-codoped SrTiO<sub>3</sub> as a hydrogen evolution photocatalyst in Z-scheme overall water splitting under visible light irradiation. Chem Mater 2014;26:4144–50.
- [204] Tahir M, Tasleem S, Tahir B. Recent development in band engineering of binary semiconductor materials for solar driven photocatalytic hydrogen production. Int J Hydrogen Energy 2020;32:15985–6038.
- [205] Maeda K. Rhodium-doped barium titanate perovskite as a stable p-type semiconductor photocatalyst for hydrogen evolution under visible light. ACS appl. Mater. Interfaces 2014;6:2167–73.
- [206] Maeda K, Lu D, Domen K. Solar-Driven Z-scheme water splitting using modified BaZrO<sub>3</sub>-BaTaO<sub>2</sub>N solid solutions as photocatalysts. ACS Catal 2013;3:1026–33.
- [207] Li P, Zhou Y, Li H, Xu Q, Meng X, Wang X, et al. All-solid-state Z-scheme system arrays of Fe<sub>2</sub>V<sub>4</sub>O<sub>13</sub>/RGO/Cds for visible light-driving photocatalytic CO<sub>2</sub> reduction into renewable hydrocarbon Fuel. Chem Commun 2014;51:800–3.
- [208] Iwase A, Ng YH, Ishiguro Y, Kudo A, Amal R. Reduced graphene oxide as a solid-state electron mediator in Z-scheme photocatalytic water splitting under visible light. J Am Chem Soc 2011;133:11054–7.
- [209] Wei Y, Zhang X, Xu J, Wang J, Huang Y, Fan L, et al. Enhancement of photocatalytic activity from HCa<sub>2</sub>Ta<sub>x</sub>Nb<sub>3-x</sub>O<sub>10</sub> (x=0, 1), co-intercalated with sulfides particles. Appl Catal, B 2014;147:920–8.

- [210] Boltersdorf J, Maggard PA. Silver exchange of layered metal oxides and their photocatalytic activities. *ACS Catal* 2013;3:2547–55.
- [211] Wang Q, Hisatomi T, Moriya Y, Maeda K, Domen K. Physicochemical properties and photocatalytic H<sub>2</sub> evolution activity of Rh-doped La<sub>2</sub>Ti<sub>2</sub>O<sub>7</sub> prepared by molten salt synthesis. *Catal Sci Technol* 2013;3:2098–103.
- [212] Huang Y, Wei Y, Cheng S, Fan L, Li Y, Lin J, et al. Photocatalytic property of nitrogen-doped layered perovskite K<sub>2</sub>La<sub>2</sub>Ti<sub>3</sub>O<sub>10</sub>. *Sol Energy Mater Sol Cells* 2010; 94:761–6.
- [213] Marschall R, Soldat J, Wark M. Enhanced photocatalytic hydrogen generation from barium tantalate composites. *Photochem Photobiol Sci* 2013;12:671–7.
- [214] Kim J, Hwang DW, Kim HG, Bae SW, Lee JS, Li W, et al. Highly efficient overall water splitting through optimization of preparation and operation conditions of layered perovskite photocatalysts. *Top Catal* 2005;35:295–303.
- [215] Kim HG, Borse PH, Jang JS, Jeong ED, Lee JS. Enhanced photochemical properties of electron rich W-doped PbBi<sub>2</sub>Nb<sub>2</sub>O<sub>9</sub> layered perovskite material under visible-light irradiation. *Mater Lett* 2008;62:1427–30.
- [216] Xu Q, Zhang L, Yu J, Wageh S, Al-Ghamdi AA, Jaroniec M. Direct Z-scheme photocatalysts: principles, synthesis, and applications. *Mater Today* 2018;21: 1042–63.
- [217] Abe R. Development of a new system for photocatalytic water splitting into H<sub>2</sub> and O<sub>2</sub> under visible light irradiation. *Bull Chem Soc Jpn* 2011;84:1000–30.
- [218] Liang X, Zheng H, Li X, Yu Y, Yue G, Zhang W, et al. Nanocomposites of Bi<sub>5</sub>FeTi<sub>3</sub>O<sub>15</sub> with MoS<sub>2</sub> as novel Pt-free counter electrode in dye-sensitized solar cells. *Ceram Int* 2016;42:12888–93.
- [219] Zhang P, Hua X, Teng X, Liu D, Qin Z, Ding S. CTAB assisted hydrothermal synthesis of lamellar Bi<sub>2</sub>WO<sub>6</sub> with superior photocatalytic activity for rhodamine b degradation. *Mater Lett* 2016;185:275–7.
- [220] Bai Y, Chen J, Wu X, Zhao S. Photovoltaic behaviors regulated by band-gap and bipolar electrical cycling inholmium-doped Bi<sub>5</sub>Ti<sub>3</sub>FeO<sub>15</sub> ferroelectric films. *J Phys Chem C* 2016;120:24637–45.
- [221] Arif M, Min Z, Yuting L, Yin H, Liu X. A Bi<sub>2</sub>WO<sub>6</sub>-based hybrid heterostructures photocatalyst with enhanced photodecomposition and photocatalytic hydrogen evolution through Z-scheme process. *J Ind Eng Chem* 2019;69:345–57.
- [222] Jiang L, Ni S, Liu G, Xu X. Photocatalytic hydrogen production over Aurivillius compound Bi<sub>3</sub>TiNbO<sub>9</sub> and its modifications by Cr/Nb co-doping. *Appl Catal, B* 2017;217:342–52.
- [223] Zhang H, Chen G, Li X. Synthesis and visible light photocatalysis water splitting property of chromium-doped Bi<sub>4</sub>Ti<sub>3</sub>O<sub>12</sub>. *Solid State Ionics* 2009;180:1599–603.
- [224] Chang C-J, Wang C-W, Wei Y-H, Chen C-Y. Enhanced photocatalytic H<sub>2</sub> production activity of Ag-doped Bi<sub>2</sub>WO<sub>6</sub>-graphene based photocatalysts. *Int J Hydrogen Energy* 2018;43:11345–54.
- [225] Qian X, Xia L, Jiang Z, Wei W, Chen L, Xie J. In situ chemical transformation synthesis of Bi<sub>4</sub>Ti<sub>3</sub>O<sub>12</sub>/I<sub>2</sub>-BiOCl 2D/2D heterojunction systems for water pollution treatment and hydrogen production. *Catal Sci* 2017;7:3863–75.
- [226] Shimizu K, Kato H, Kobayashi M, Kakihana M. Synthesis and photocatalytic properties of tetragonal tungsten bronze type oxynitrides. *Appl Catal, B* 2017;206: 444–8.
- [227] Chen H, Xu X. Ruddlesden-Popper compounds in the double-perovskite family Sr<sub>n</sub>FeTaO<sub>6</sub>(Sr<sub>n</sub>O)(n=0, 1 and 2) and their photocatalytic properties. *Appl Catal, B* 2017;206:35–43.
- [228] Huerta-Flores AM, Torres-Martínez LM, Moctezuma E. Overall photocatalytic water splitting on Na<sub>2</sub>Zr<sub>x</sub>Ti<sub>6-x</sub>O<sub>13</sub> (x=0, 1) nanobelts modified with metal oxide nanoparticles as cocatalysts. *Int J Hydrogen Energy* 2017;42:14547–59.
- [229] Wang Q, Hisatomi T, Moriya Y, Maeda K, Domen K. Physicochemical properties and photocatalytic H<sub>2</sub> evolution activity of Rh-doped La<sub>2</sub>Ti<sub>2</sub>O<sub>7</sub> prepared by molten salt synthesis. *Catal Sci* 2013;3:2098–103.
- [230] Chen S, Yang J, Ding C, Li R, Jin S, Wang D, et al. Nitrogen-doped layered oxide Sr<sub>5</sub>Ta<sub>4</sub>O<sub>15-x</sub>N<sub>x</sub> for water reduction and oxidation under visible light irradiation. *J Mater Chem* 2013;1:5651–9.
- [231] Mukherji A, Sun C, Smith SC, Lu GQ, Wang L. Photocatalytic hydrogen production from water using N-doped Ba<sub>5</sub>Ta<sub>4</sub>O<sub>15</sub> under solar irradiation. *J Phys Chem C* 2011;115:15674–8.
- [232] Jeong H, Kim T, Kim D, Kim K. Hydrogen production by the photocatalytic overall water splitting on NiO/Sr<sub>3</sub>Ti<sub>2</sub>O<sub>7</sub>: effect of preparation method. *Int J Hydrogen Energy* 2006;31:1142–6.
- [233] Hwang DW, Kim HG, Lee JS, Kim J, Li W, Oh SH. Photocatalytic hydrogen production from water over M-doped La<sub>2</sub>Ti<sub>2</sub>O<sub>7</sub> (M= Cr, Fe) under visible light irradiation ( $\lambda > 420$  nm). *J Phys Chem B* 2005;109:2093–102.
- [234] Yang D, Lv J, Zhao X, Xu Q, Fu Y, Zhan Y, et al. Functionality-directed screening of Pb-free hybrid organic-inorganic perovskites with desired intrinsic photovoltaic functionalities. *Chem Mater* 2017;29:524–38.
- [235] Pang S, Hu H, Zhang J, Lv S, Yu Y, Wei F, et al. NH<sub>2</sub>CHNH<sub>2</sub>PbI<sub>3</sub>: an alternative organolead iodide perovskite sensitizer for mesoscopic solar cells. *Chem Mater* 2014;26:1485–91.
- [236] Mitzi DB, Feild C, Schlesinger Z, Laibowitz R. Transport, optical, and magnetic properties of the conducting halide perovskite CH<sub>3</sub>NH<sub>3</sub>SnI<sub>3</sub>. *J Solid State Chem* 1995;114:159–63.
- [237] Eperon GE, Stranks SD, Menelaou C, Johnston MB, Herz LM, Snaith HJ. Formamidinium lead trihalide: a broadly tunable perovskite for efficient planar heterojunction solar cells. *Energy Environ Sci* 2014;7:982–8.
- [238] Ogomi Y, Morita A, Tsukamoto S, Saitoh T, Fujikawa N, Shen Q, et al. CH<sub>3</sub>NH<sub>3</sub>Sn<sub>x</sub>Pb<sub>(1-x)</sub>I<sub>3</sub> Perovskite solar cells covering up to 1060 nm. *J Phys Chem Lett* 2014;5:1004–11.
- [239] Chen Q, De Marco N, Yang Y, Song T-B, Chen C-C, Zhao H, et al. Under the spotlight: the organic-inorganic hybrid halide perovskite for optoelectronic applications. *Nano Today* 2015;10:355–96.
- [240] Frost JM, Butler KT, Brivio F, Hendon CH, Van Schilfgaarde M, Walsh A. Atomistic origins of high-performance in hybrid halide perovskite solar cells. *Nano Lett* 2014;14:2584–90.
- [241] García T, García-Aboal R, Alberto J, Atienzar P, García H. Vapor-phase photocatalytic overall water splitting using hybrid methylammonium copper and lead perovskites. *J Nanomater* 2020;10:960.
- [242] Lang L, Yang J-H, Liu H-R, Xiang H, Gong X. First-principles study on the electronic and optical properties of cubic ABX<sub>3</sub> halide perovskites. *Phys Lett* 2014;378:290–3.
- [243] Yin W-J, Shi T, Yan Y. Superior photovoltaic properties of lead halide perovskites: insights from first-principles theory. *J Phys Chem C* 2015;119:5253–64.
- [244] Miyata A, Mitioglu A, Plochocka P, Portegiesz O, Wang JT-W, Stranks SD, et al. Direct measurement of the exciton binding energy and effective masses for charge carriers in organic-inorganic tri-halide perovskites. *Nat Phys* 2015;11:582–7.
- [245] D'innocenzo V, Grancini G, Alcocer MJ, Kandada ARS, Stranks SD, Lee MM, et al. Excitons versus free charges in organo-lead tri-halide perovskites. *Nat Commun* 2014;5:1–6.
- [246] Stranks SD, Eperon GE, Grancini G, Menelaou C, Alcocer MJ, Leijtens T, et al. Electron-hole diffusion lengths exceeding 1 micrometer in an organometal trihalide perovskite absorber. *J Sci* 2013;342:341–4.
- [247] De Wolf S, Holovsky J, Moon S-J, López P, Niesen B, Ledinsky M, et al. Organometallic halide perovskites: sharp optical absorption edge and its relation to photovoltaic performance. *J Phys Chem Lett* 2014;5:1035–9.
- [248] Huynh KA, Nguyen DLT, Nguyen VH, Vo DVN, Trinh QT, Nguyen TP, et al. Halide perovskite photocatalysis: progress and perspectives. *J Chem* 2020.
- [249] Pavliuk MV, Abdellah M, Sá J. Hydrogen evolution with CsPbBr<sub>3</sub> perovskite nanocrystals under visible light in solution. *Mater. Today Commun* 2018;16:90–6.
- [250] Saidaminov MI, Abdelyad AL, Murali B, Alarousu E, Burlakov VM, Peng W, et al. High-yield bulk hybrid perovskite single crystals within minutes by inverse temperature crystallization. *Nat Commun* 2015;6:1–6.
- [251] Ali N, Rauf S, Kong W, Ali S, Wang X, Khesro A, et al. An overview of the decompositions in organo-metal halide perovskites and shielding with 2-dimensional perovskites. *Renew Sustain Energy Rev* 2019;109:160–86.
- [252] Akilan T, Srinivasan N, Saravanan R, Chowdury P. Structure of vanadium-doped zinc oxide, Zn<sub>1-X</sub>V<sub>X</sub>O. *Mater Manuf Process* 2014;29:780–8.
- [253] Wu Y, Wang P, Zhu X, Zhang Q, Wang Z, Liu Y, et al. Composite of CH<sub>3</sub>NH<sub>3</sub>PbI<sub>3</sub> with reduced graphene oxide as a highly efficient and stable visible-light photocatalyst for hydrogen evolution in aqueous HI solution. *Adv Mater* 2018;30: 1704342.
- [254] Wang H, Wang X, Chen R, Zhang H, Wang X, Wang J, et al. Promoting photocatalytic H<sub>2</sub> evolution on organic-inorganic hybrid perovskite nanocrystals by simultaneous dual-charge transportation modulation. *ACS Energy Lett* 2019;4: 40–7.
- [255] Park S, Chang WJ, Lee CW, Park S, Ahn H-Y, Nam KT. Photocatalytic hydrogen generation from hydriodic acid using methylammonium lead iodide in dynamic equilibrium with aqueous solution. *Nat Energy* 2017;2:16185.
- [256] Wang X, Wang H, Zhang H, Yu W, Wang X, Zhao Y, et al. Dynamic interaction between methylammonium lead iodide and TiO<sub>2</sub> nanocrystals leads to enhanced photocatalytic H<sub>2</sub> evolution from HI splitting. *ACS Energy Lett* 2018;3:1159–64.
- [257] Hoeveler SF, Trimmel G, Rath T. Progress on lead-free metal halide perovskites for photovoltaic applications: a review. *Monatsh Chem* 2017;148:795–826.
- [258] Chatterjee S, Pal AJ. Influence of metal substitution on hybrid halide perovskites: towards lead-free perovskite solar cells. *J Mater Chem* 2018;6:3793–823.
- [259] Filip MR, Giustino F. Computational screening of homovalent lead substitution in organic-inorganic halide perovskites. *J Phys Chem* 2016;120:166–73.
- [260] Shi Z, Guo J, Chen Y, Li Q, Pan Y, Zhang H, et al. Lead-free organic-inorganic hybrid perovskites for photovoltaic applications: recent advances and perspectives. *Adv Mater* 2017;29:1605005.
- [261] Fu H. Review of lead-free halide perovskites as light-absorbers for photovoltaic applications: from materials to solar cells. *Sol Energy Mater Sol Cells* 2019;193: 107–32.
- [262] Jellicoe TC, Richter JM, Glass HFJ, Tabachnyk M, Brady R, Dutton SE, et al. Synthesis and optical properties of lead-free cesium tin halide perovskite nanocrystals. *J Am Chem Soc* 2016;138:2941–4.
- [263] Stoumpos CC, Kanatzidis MG. Halide Perovskites: poor Man's high-performance semiconductors. *Adv Mater* 2016;28:5778–93.
- [264] Mohan R. Green bismuth. *Nat Chem* 2010;2:336.
- [265] Zhao H, Li Y, Zhang B, Xu T, Wang C. Pt<sub>x</sub>/[(CH<sub>3</sub>)<sub>2</sub>NH<sub>2</sub>]<sub>3</sub>[BiI<sub>3</sub>] as a well-dispersed photocatalyst for hydrogen production in hydriodic acid. *Nanomater Energy* 2018;50:665–74.
- [266] Guo Y, Liu G, Li Z, Lou Y, Chen J, Zhao Y. Stable lead-free (CH<sub>3</sub>NH<sub>3</sub>)<sub>3</sub>Bi<sub>2</sub>I<sub>9</sub> perovskite for photocatalytic hydrogen generation. *ACS Sustainable Chem Eng* 2019;7:15080–5.
- [267] Testino A, Bellobono IR, Buscaglia V, Canevali C, D'Arienzo M, Polizzi S, et al. Optimizing the photocatalytic properties of hydrothermal TiO<sub>2</sub> by the control of phase composition and particle morphology. A systematic approach. *J Am Chem Soc* 2007;129:3564–75.
- [268] West JL, Halas NJ. Applications of nanotechnology to biotechnology: Commentary. *Curr Opin Biotechnol* 2000;11:215–7.
- [269] Jin Y, Jiang D, Li D, Xiao P, Ma X, Chen M. SrTiO<sub>3</sub> nanoparticle/SnNb<sub>2</sub>O<sub>6</sub> nanosheet OD/2D heterojunctions with enhanced interfacial charge separation and photocatalytic hydrogen evolution activity. *ACS Sustainable Chem Eng* 2017; 5:9749–57.
- [270] Yang W, Yu Y, Starr MB, Yin X, Li Z, Kvit A, et al. Ferroelectric polarization-enhanced photoelectrochemical water splitting in TiO<sub>2</sub>-BaTiO<sub>3</sub> core-shell nanowire photoanodes. *Nano Lett* 2015;15:7574–80.

- [271] Ha MN, Zhu F, Liu Z, Wang L, Liu L, Lu G, et al. Morphology-controlled synthesis of SrTiO<sub>3</sub>/TiO<sub>2</sub> heterostructures and their photocatalytic performance for water splitting. *RSC Adv* 2016;6:21111–8.
- [272] Jiao Z, Zhang Y, Chen T, Dong Q, Lu G, Bi Y. TiO<sub>2</sub> nanotube Arrays modified with Cr-doped SrTiO<sub>3</sub> nanocubes for highly efficient hydrogen evolution under visible light. *Chem Eur* 2014;20:2654–62.
- [273] Ahmad H, Kamarudin SK, Minggu LJ, Kassim M. Hydrogen from photo-catalytic water splitting process: a review. *Renew Sustain Energy Rev* 2015;43:599–610.
- [274] Yu J, Ran J. Facile preparation and enhanced photocatalytic H<sub>2</sub>-production activity of Cu(OH)<sub>2</sub> cluster modified TiO<sub>2</sub>. *Energy Environ Sci* 2011;4:1364–71.
- [275] Digdaya I, Han L, Buijs T, Zeman M, Dam B, Smets A, et al. Extracting large photovoltages from a-SiC photocathodes with an amorphous TiO<sub>2</sub> front surface field layer for solar hydrogen evolution 2015;8:1585–93.
- [276] Chen Y-L, Lo S-L, Chang H-L, Yeh H-M, Sun L, Oiu C. Photocatalytic hydrogen production of the CdS/TiO<sub>2</sub>-WO<sub>3</sub> ternary hybrid under visible light irradiation. *Water Sci Technol* 2016;73:1667–72.
- [277] Momeni MM, Ghayeb Y, Davarzadeh M. Single-step electrochemical anodization for synthesis of hierarchical WO<sub>3</sub>-TiO<sub>2</sub> nanotube arrays on titanium foil as a good photoanode for water splitting with visible light. *J Electroanal Chem* 2015;739:149–55.
- [278] Sreethawong T, Suzuki Y, Yoshikawa S. Photocatalytic evolution of hydrogen over mesoporous TiO<sub>2</sub> supported NiO photocatalyst prepared by single-step sol-gel process with surfactant template. *Int J Hydrogen Energy* 2005;30:1053–62.
- [279] Yu J, Hai Y, Cheng B. Enhanced photocatalytic H<sub>2</sub>-production activity of TiO<sub>2</sub> by Ni(OH)<sub>2</sub> cluster modification. *J Phys Chem C* 2011;115:4953–8.
- [280] González-Moya JR, García-Basabe Y, Rocco MLM, Pereira MB, Princival JL, Almeida LC, et al. Effects of the large distribution of CdS quantum dot sizes on the charge transfer interactions into TiO<sub>2</sub> nanotubes for photocatalytic hydrogen generation. *Nanotechnology* 2016;27:285401.
- [281] Hwang YJ, Boukai A, Yang P. High density n-Si-n-TiO<sub>2</sub> core/shell nanowire arrays with enhanced photoactivity. *Nano Lett* 2008;9:410–5.
- [282] Shi J, Wang X. Hierarchical TiO<sub>2</sub>-Si nanowire architecture with photoelectrochemical activity under visible light illumination. *Energy Environ Sci* 2012;5:7918–22.
- [283] Ng J, Xu S, Zhang X, Yang HY, Sun DD. Hybridized nanowires and cubes: a novel architecture of a heterojunctioned TiO<sub>2</sub>/SrTiO<sub>3</sub> thin film for efficient water splitting. *Adv Funct Mater* 2010;20:4287–94.
- [284] Han T, Chen Y, Tian G, Wang J-Q, Ren Z, Zhou W, et al. Hierarchical FeTiO<sub>3</sub>-TiO<sub>2</sub> hollow spheres for efficient simulated sunlight-driven water oxidation. *Nanoscale* 2015;7:15924–34.
- [285] Fang D, Huang K, Liu S, Luo Z, Qing X, Zhang Q. High-density NiTiO<sub>3</sub>/TiO<sub>2</sub> nanotubes synthesized through sol-gel method using well-ordered TiO<sub>2</sub> membranes as template. *J Alloys Compd* 2010;498:37–41.
- [286] Fajrina N, Tahir M. 2D-montmorillonite-dispersed g-C<sub>3</sub>N<sub>4</sub>/TiO<sub>2</sub> 2D/0D heterojunction composite for enhanced visible-light-induced H<sub>2</sub> evolution from glycerol-water mixture 2019;471:1053–64.
- [287] Tahir M, Mulewa W, Amin NAS, Zakaria ZY. Thermodynamic and experimental analysis on ethanol steam reforming for hydrogen production over Ni-modified TiO<sub>2</sub>/MMT nanoclay catalyst. *Energy Convers Manag* 2017;154:25–37.
- [288] Tahir B, Tahir M. Morphological effect of 1D/1D In<sub>2</sub>O<sub>3</sub>/TiO<sub>2</sub> NRs/NWs heterojunction photo-embedded with Cu-NPs for enhanced photocatalytic H<sub>2</sub> evolution under visible light. *Appl Surf Sci* 2020;506:145034.
- [289] Huang J, Jiang Y, Li G, Xue C, Guo W. Hetero-structural NiTiO<sub>3</sub>/TiO<sub>2</sub> nanotubes for efficient photocatalytic hydrogen generation. *Renew Energy* 2017;111:410–5.
- [290] Azam MU, Tahir M, Umer M, Jaffar MM, Nawawi MGM. Engineering approach to enhance photocatalytic water splitting for dynamic H<sub>2</sub> production using La<sub>2</sub>O<sub>3</sub>/TiO<sub>2</sub> nanocatalyst in a monolith photoreactor. *Appl Surf Sci* 2019;484:1089–101.
- [291] Sanzone G, Zimbone M, Cacciato G, Ruffino F, Carles R, Privitera V, et al. Ag/TiO<sub>2</sub> nanocomposite for visible light-driven photocatalysis. *Superlattice Microst* 2018;123:394–402.
- [292] Subha N, Mahalakshmi M, Myilsamy M, Reddy NL, Shankar M, Neppolian B, et al. Influence of synthesis conditions on the photocatalytic activity of mesoporous Ni doped SrTiO<sub>3</sub>/TiO<sub>2</sub> heterostructure for H<sub>2</sub> production under solar light irradiation. *Colloids Surf, A* 2017;522:193–206.
- [293] Humayun M, Zada A, Li Z, Xie M, Zhang X, Qu Y, et al. Enhanced visible-light activities of porous BiFeO<sub>3</sub> by coupling with nanocrystalline TiO<sub>2</sub> and mechanism. *Appl Catal* 2016;180:219–26.
- [294] Lv T, Wang H, Hong W, Wang P, Jia L. In situ self-assembly synthesis of sandwich-like TiO<sub>2</sub>/reduced graphene oxide/LaFeO<sub>3</sub> Z-scheme ternary heterostructure towards enhanced photocatalytic hydrogen production. *Mol Catal* 2019;475:110497.
- [295] Lakhera SK, Hafeez HY, Veluswamy P, Ganesh V, Khan A, Ikeda H, et al. Enhanced photocatalytic degradation and hydrogen production activity of in situ grown TiO<sub>2</sub> coupled NiTiO<sub>3</sub> nanocomposites. *Appl Surf Sci* 2018;449:790–8.
- [296] Yan J-H, Zhu Y-R, Tang Y-G, Zheng S-Q. Nitrogen-doped SrTiO<sub>3</sub>/TiO<sub>2</sub> composite photocatalysts for hydrogen production under visible light irradiation. *J Alloys Compd* 2009;472:429–33.
- [297] Kumar S, Kumar A, Bahuguna A, Sharma V, Krishnan V. Two-dimensional carbon-based nanocomposites for photocatalytic energy generation and environmental remediation applications. *Beilstein J Nanotechnol* 2017;8:1571–600.
- [298] Umer M, Tahir M, Usman Azam M, Tasleem S, Abbas T, Muhammad A. Synergistic effects of single/multi-walls carbon nanotubes in TiO<sub>2</sub> and process optimization using response surface methodology for photo-catalytic H<sub>2</sub> evolution. *J. Environ. Chem* 2019;7.
- [299] Cao S, Yu J. Carbon-based H<sub>2</sub>-production photocatalytic materials. *J Photochem Photobiol, A* 2016;27:72–99.
- [300] Syed N, Huang J, Feng Y, Wang X, Cao L. Carbon-based nanomaterials via heterojunction serving as photocatalyst. *Front. Chem* 2019;7:713.
- [301] Rowley-Neale SJ, Randvirk EP, Abo Dena AS, Banks CE. An overview of recent applications of reduced graphene oxide as a basis of electroanalytical sensing platforms. *Appl Mater Today* 2018;10:218–26.
- [302] McAllister MJ, Li J-L, Adamson DH, Schniepp HC, Abdala AA, Liu J, et al. Single sheet functionalized graphene by oxidation and thermal expansion of graphite. *Chem Mater* 2007;19:4396–404.
- [303] Stankovich S, Dikin DA, Domke GH, Kohlhaas KM, Zimney EJ, Stach EA, et al. Graphene-based composite materials. *Nature* 2006;442:282.
- [304] Xiang Q, Yu J. Graphene-based photocatalysts for hydrogen generation. *J Chem Lett* 2013;4:753–9.
- [305] An J, Zhu L, Wang N, Song Z, Yang Z, Du D, et al. Photo-Fenton like degradation of tetrabromobisphenol A with grapheneBiFeO<sub>3</sub> composite as a catalyst. *Chem Eng J* 2013;219:225–37.
- [306] Bafaqueer A, Tahir M, Amin NAS. Synergistic effects of 2D/2D ZnV<sub>2</sub>O<sub>6</sub>/RGO nanosheets heterojunction for stable and high performance photo-induced CO<sub>2</sub> reduction to solar fuels. *Chem Eng J* 2018;334:2142–53.
- [307] Zhao X, Wu G, Deng Y, Han D, Zhang B, et al. A review of studies using graphenes in energy conversion, energy storage and heat transfer development. *Energy Convers Manag* 2019;184:581–99.
- [308] Huang H, Yue Z, Li G, Wang X, Huang J, Du Y, et al. Ultraviolet-assisted preparation of mesoporous WO<sub>3</sub>/reduced graphene oxide composites: superior interfacial contacts and enhanced photocatalysis. *J Mater Chem* 2013;1:15110–6.
- [309] Pham T-T, Nguyen-Huy C, Shin EW. Facile one-pot synthesis of nickel-incorporated titanium dioxide/graphene oxide composites: enhancement of photodegradation under visible-irradiation. *Appl Surf Sci* 2016;377:301–10.
- [310] Zhang W, Li Y, Peng S. Facile synthesis of graphene sponge from graphene oxide for efficient dye-sensitized H<sub>2</sub> evolution. *ACS Appl Mater Interfaces* 2016;8:15187–95.
- [311] Dave SH, Gong C, Robertson AW, Warner JH, Grossman JC. Chemistry and structure of graphene oxide via direct imaging. *ACS Nano* 2016;10:7515–22.
- [312] Ong W-J, Yeong J-J, Tan L-L, Goh BT, Yong S-T, Chai S-P. Synergistic effect of graphene as a co-catalyst for enhanced daylight-induced photocatalytic activity of Zn<sub>0.5</sub>Cd<sub>0.5</sub>S synthesized via an improved one-pot co-precipitation-hydrothermal strategy. *RSC Adv* 2014;4:59676–85.
- [313] Li J, Yin Y, Liu E, Ma Y, Wan J, Fan J, et al. In situ growing Bi<sub>2</sub>MoO<sub>6</sub> on g-C<sub>3</sub>N<sub>4</sub> nanosheets with enhanced photocatalytic hydrogen evolution and disinfection of bacteria under visible light irradiation. *J Hazard Mater* 2017;321:183–92.
- [314] Song X, Shi Q, Wang H, Liu S, Tai C, Bian Z. Preparation of Pd-Fe/graphene catalysts by photocatalytic reduction with enhanced electrochemical oxidation-reduction properties for chlorophenols. *Appl Catal, B* 2017;203:442–51.
- [315] Adamu H, Dubey P, Anderson JA. Probing the role of thermally reduced graphene oxide in enhancing performance of TiO<sub>2</sub> in photocatalytic phenol removal from aqueous environments. *Chem Eng J* 2016;284:380–8.
- [316] Liu R, Zhu X, Chen B. A new insight of graphene oxide-Fe (III) complex photochemical behaviors under visible light irradiation. *Sci Rep* 2017;7:40711.
- [317] Morales-Narváez E, Sgobbi LF, Machado SAS, Merkoç A. Graphene-encapsulated materials: synthesis, applications and trends. *Prog Mater Sci* 2017;86:1–24.
- [318] Acharya S, Padhi DK, Parida KM. Visible light driven LaFeO<sub>3</sub> nano sphere/RGO composite photocatalysts for efficient water decomposition reaction. *Catal Today* 2017.
- [319] He G-L, Zhong Y-H, Chen M-J, Li X, Fang Y-P, Xu Y-H. One-pot hydrothermal synthesis of SrTiO<sub>3</sub>-reduced graphene oxide composites with enhanced photocatalytic activity for hydrogen production. *J Mol Catal Chem* 2016;423:70–6.
- [320] Diab KR, El-Maghribi HH, Nada AA, Youssef AM, Hamdy A, Roualdes S, et al. Facile fabrication of NiTiO<sub>3</sub>/graphene nanocomposites for photocatalytic hydrogen generation. *J Photochem Photobiol, A* 2018;365:86–93.
- [321] Hong Z, Li X, Kang S-z, Qin L, Li G, Mu J. Modifications of morphology and hydrogen evolution activity for the potassium niobate nanoscrolls by introducing reduced graphene oxide. *Int J Hydrogen Energy* 2015;40:14297–304.
- [322] Lv T, Wu M, Guo M, Liu Q, Jia L. Self-assembly photocatalytic reduction synthesis of graphene-encapsulated LaNiO<sub>3</sub> nanoreactor with high efficiency and stability for photocatalytic water splitting to hydrogen. *Chem Eng J* 2019;356:580–91.
- [323] Mukherji A, Seger B, Lu GQ, Wang L. Nitrogen doped Sr<sub>2</sub>Ta<sub>2</sub>O<sub>7</sub> coupled with graphene sheets as photocatalysts for increased photocatalytic hydrogen production. *ACS Nano* 2011;5:3483–92.
- [324] Suzuki TM, Iwase A, Tanaka H, Sato S, Kudo A, Morikawa T. Z-scheme water splitting under visible light irradiation over powdered metal-complex/semiconductor hybrid photocatalysts mediated by reduced graphene oxide. *J Mater Chem* 2015;3:13283–90.
- [325] Hong Z, Li X, Kang S-z, Qin L, Li G, Mu J. Enhanced photocatalytic activity and stability of the reduced graphene oxide loaded potassium niobate microspheres for hydrogen production from water reduction. *Int J Hydrogen Energy* 2014;39:12515–23.
- [326] Ding J, Yan W, Xie W, Sun S, Bao J, Gao C. Highly efficient photocatalytic hydrogen evolution of graphene/YInO<sub>3</sub> nanocomposites under visible light irradiation. *Nanoscale* 2014;6:2299–306.
- [327] Wu M, Yan J-M, Zhang X-W, Zhao M, Jiang Q. Ag<sub>2</sub>O modified g-C<sub>3</sub>N<sub>4</sub> for highly efficient photocatalytic hydrogen generation under visible light irradiation. *J Mater Chem* 2015;3:15710–4.

- [328] Fajrina N, Tahir M. Monolithic Ag-Mt dispersed Z-scheme pCN-TiO<sub>2</sub> heterojunction for dynamic photocatalytic H<sub>2</sub> evolution using liquid and gas phase photoreactors. *Int J Hydrogen Energy* 2020;45:4355–75.
- [329] Jiang W, Luo W, Wang J, Zhang M, Zhu Y. Enhancement of catalytic activity and oxidative ability for graphitic carbon nitride. *J Photochem Photobiol A* 2016;28:87–115.
- [330] Fajrina N, Tahir M. 2D-montmorillonite-dispersed g-C<sub>3</sub>N<sub>4</sub>/TiO<sub>2</sub> 2D/ODnanocomposite for enhanced photo-induced H<sub>2</sub> evolution from glycerol-water mixture. *Appl Surf Sci* 2019;471:1053–64.
- [331] Jiang L, Yuan X, Pan Y, Liang J, Zeng G, Wu Z, et al. Doping of graphitic carbon nitride for photocatalysis: a review. *Appl Catal, B* 2017;217:388–406.
- [332] Wang X, Blechert S, Antonietti M. Polymeric graphitic carbon nitride for heterogeneous photocatalysis. *ACS Catal* 2012;2:1596–606.
- [333] Xu J, Zhang L, Shi R, Zhu Y. Chemical exfoliation of graphitic carbon nitride for efficient heterogeneous photocatalysis. *J Mater Chem* 2013;1:14766–72.
- [334] Maeda K, Eguchi M, Oshima T. Perovskite oxide nanosheets with tunable band-edge potentials and high photocatalytic hydrogen-evolution activity. *Angew Chem Int Ed* 2014;53:13164–8.
- [335] Tahir B, Tahir M, Amin NAS. Ag-La loaded protonated carbon nitrides nanotubes (pCNNT) with improved charge separation in a monolithic honeycomb photoreactor for enhanced bireforming of methane (BRM) to fuels. *Appl Catal, B* 2019;248:167–83.
- [336] Zeng Y, Wang Y, Chen J, Jiang Y, Kiani M, Li B, et al. Fabrication of high-activity hybrid NiTiO<sub>3</sub>/g-C<sub>3</sub>N<sub>4</sub> heterostructured photocatalysts for water splitting to enhanced hydrogen production. *Ceram Int* 2016;42:12297–305.
- [337] Chen P, Xing P, Chen Z, Hu X, Lin H, Zhao L, et al. In-situ synthesis of AgNbO<sub>3</sub>/g-C<sub>3</sub>N<sub>4</sub> photocatalyst via microwave heating method for efficiently photocatalytic H<sub>2</sub> generation. *J Colloid Interface Sci* 2019;534:163–71.
- [338] Wang X, Maeda K, Thomas AK, Xin G, Carlsson JM, Domen K, Antonietti M. *Nat Mater* 2009;8:76–80.
- [339] Jiang D, Wang T, Xu Q, Li D, Meng S, Chen M. Perovskite oxide ultrathin nanosheets/g-C<sub>3</sub>N<sub>4</sub> 2D-2D heterojunction photocatalysts with significantly enhanced photocatalytic activity towards the photodegradation of tetracycline. *Appl Catal, B* 2017;201:617–28.
- [340] Jiang D, Ma W, Yao Y, Xiao P, Wen B, Li D, et al. Dion-Jacobson-type perovskite KCa<sub>2</sub>Ta<sub>3</sub>O<sub>10</sub> nanosheets hybridized with g-C<sub>3</sub>N<sub>4</sub> nanosheets for photocatalytic H<sub>2</sub> production. *Catal. Sci* 2018;8:3767–73.
- [341] Thaweesak S, Lyu M, Peerakiatkhaohn P, Butburee T, Luo B, Chen H, et al. Two-dimensional g-C<sub>3</sub>N<sub>4</sub>/Ca<sub>2</sub>Nb<sub>2</sub>TaO<sub>10</sub> nanosheet composites for efficient visible light photocatalytic hydrogen evolution. *Appl Catal, B* 2017;202:184–90.
- [342] Pan J, Jiang Z, Feng S, Zhao C, Dong Z, Wang B, et al. The enhanced photocatalytic hydrogen production of the fusiform g-C<sub>3</sub>N<sub>4</sub> modification CaTiO<sub>3</sub> nano-heterojunction. *Int J Hydrogen Energy* 2018;43:19019–28.
- [343] Adhikari SP, Hood ZD, Wang H, Peng R, Krall A, Li H, et al. Enhanced visible light photocatalytic water reduction from a g-C<sub>3</sub>N<sub>4</sub>/SrTa<sub>2</sub>O<sub>6</sub> heterojunction. *Appl Catal* 2017;217:448–58.
- [344] Jiang D, Ma W, Yao Y, Xiao P, Wen B, Li D, et al. Dion-Jacobson-type perovskite KCa<sub>2</sub>Ta<sub>3</sub>O<sub>10</sub> nanosheets hybridized with g-C<sub>3</sub>N<sub>4</sub> nanosheets for photocatalytic H<sub>2</sub> production. *Catal Sci* 2018;8:3767–73.
- [345] Cheng L, Xiang Q, Liao Y, Zhang H. CdS-based photocatalysts. *Energy Environ Sci* 2018;11:1362–91.
- [346] Mao L, Cai X, Yang S, Han K, Zhang J. Black phosphorus-CdS-La<sub>2</sub>Ti<sub>2</sub>O<sub>7</sub> ternary composite: effective noble metal-free photocatalyst for full solar spectrum activated H<sub>2</sub> production. *Appl Catal, B* 2019;242:441–8.
- [347] Moniruddin M, Meusling B, Dupre R, Casadonte DJ, Nuraje N. Nanoassembly of perovskite-based photocatalysts in a nanoconfined system for photocatalytic H<sub>2</sub> production under visible light. *J Mol Catal* 2020;483:110719.
- [348] Bajorowicz B, Kowalska E, Nadolina J, Wei Z, Endo M, Ohtani B, et al. Preparation of CdS and Bi<sub>2</sub>S<sub>3</sub> quantum dots co-decorated perovskite-type KNbO<sub>3</sub> ternary heterostructure with improved visible light photocatalytic activity and stability for phenol degradation. *Dalton Trans* 2018;47:15232–45.
- [349] Luo D, Huang Y, Zhao Y, Fang Y, Li Z, Guo Q, et al. Visible-light-driven HSr<sub>2</sub>Nb<sub>3</sub>O<sub>10</sub>/CdS heterojunctions for high hydrogen evolution activity. *Int J Hydrogen Energy* 2020;45:2896–908.
- [350] Su Y, Peng L, Guo J, Huang S, Lv L, Wang X. Tunable optical and photocatalytic performance promoted by nonstoichiometric control and site-selective codoping of trivalent ions in NaTaO<sub>3</sub>. *J Phys Chem C* 2014;118:10728–39.
- [351] Shi J, Ye J, Ma L, Ouyang S, Jing D, Guo L. Site-selected doping of upconversion luminescent Er<sup>3+</sup> into SrTiO<sub>3</sub> for visible-light-driven photocatalytic H<sub>2</sub> or O<sub>2</sub> evolution. *Chem Eur* 2012;18:7543–51.
- [352] Meziani D, Reziga A, Rekhila G, Bellal B, Trari M. Hydrogen evolution under visible light over LaCoO<sub>3</sub> prepared by chemical route. *Energy Convers Manag* 2014;82:244–9.
- [353] Iervolino G, Vaiano V, Sannino D, Rizzo L, Galluzzi A, Polichetti M, et al. Hydrogen production from glucose degradation in water and wastewater treated by Ru-LaFeO<sub>3</sub>/Fe<sub>2</sub>O<sub>3</sub> magnetic particles photocatalysis and heterogeneous photo-Fenton. *Int J Hydrogen Energy* 2018;43:2184–96.
- [354] Paramanik L, Reddy KH, Sultana S, Parida K. Architecture of biperovkite-based LaCrO<sub>3</sub>/PbTiO<sub>3</sub> p-n heterojunction with a strong interface for enhanced charge anti-recombination process and visible light-induced photocatalytic reactions. *Inorg Chem* 2018;57:15133–48.
- [355] Zhu S, Yang C, Li F, Li T, Zhang M, Cao W. Improved photocatalytic Bi<sub>2</sub>WO<sub>6</sub>/BiOCl heterojunctions: one-step synthesis via an ionic-liquid assisted ultrasonic method and first-principles calculations. *J Mol Catal* 2017;435:33–48.
- [356] Bajorowicz B, Kowalska E, Nadolina J, Wei Z, Endo M, Ohtani B, et al. Preparation of CdS and Bi<sub>2</sub>S<sub>3</sub> quantum dots co-decorated perovskite-type KNbO<sub>3</sub> ternary heterostructure with improved visible light photocatalytic activity and stability for phenol degradation. *Dalton Trans* 2018;47:15232–45.